Optomechanical Simulations for Optimizing Spin-Phonon-Photon Coupling in a Silicon Nanobeam

Master's thesis, 29.5.2024

Author:

Simeoni Ahopelto

Supervisor:

Juha Muhonen

UNIVERSITY OF JYVÄSKYLÄ
DEPARTMENT OF PHYSICS

Abstract

Ahopelto, Simeoni
Optomechanical Simulations for Optimizing Spin-Phonon-Photon Coupling in a Silicon Nanobeam
Master's thesis
Department of Physics, University of Jyväskylä, 2024, 91 pages.

We investigated the geometric design of a photonic crystal silicon nanobeam working as a quantum transducer between donor spins, phonons, and photons. The photonic crystal nanobeam combines an optical cavity with a mechanical oscillator, so that their resonance frequencies can be coupled via strain to a spin state of a donor atom in a magnetic field. In order to maximize the coupling, we optimized the geometry of the nanobeam using electromagnetic and mechanical FEM eigenfrequency simulations. We simulated a width tapered nanobeam cavity which reached an optical Q-factor of 10^6 and a maximum optomechanical coupling of $g_0/2\pi = 4\,\mathrm{MHz}$ within robust fabrication limits. We optimized the nanobeam joints for strain confinement and achieved a zero-point fluctuation strain $\varepsilon_{\mathrm{zpf}} > 10^{-9}$ corresponding to a $^{31}\mathrm{P}$ donor spin-phonon coupling of $\lambda_0 \sim 0.1\,\mathrm{kHz}$ in an ion implantable volume with requirements on magnetic field $B \leq 1\,\mathrm{T}$ and mechanical eigenfrequency $\Omega_{\mathrm{m}}/2\pi \leq 3\,\mathrm{MHz}$. The spin-phonon coupling was still an order of magnitude too small for single spin measurements. The results help to chart the direction towards feasible spin-strain coupled nanobeam transducers.

Keywords: Optomechanics, nanobeam, photonic crystal, high-Q cavity, spin coupling

Tiivistelmä

Ahopelto, Simeoni
Piinanopalkin spin-fononi-fotoni kytkennän optimisaatio optomekaanisilla simulaatioilla
Pro gradu -tutkielma
Fysiikan laitos, Jyväskylän yliopisto, 2024, 91 sivua

Työssä tutkittiin fotonikiteisen piinanopalkin mahdollisuuksia toimia kvanttimuuntimena atomin spinien, mekaanisten fononien ja optisten fotonien välillä. Fotonikiteinen nanopalkki koostuu optisesta kaviteetista ja mekaanisesta värähtelijästä, joiden resonanssitaajuudet voidaan kytkeä venymän avulla riippumaan donoriatomien spin-tilasta magneettikentässä. Kytkennän maksimoimiseksi tutkimuksessa pyrittiin optimoimaan nanopalkin geometria simuloimalla sen sähkömagneettisia ja mekaanisia resonansseja elementtimenetelmällä. Optimoinnissa päädyttiin keskeltä ohennettuun nanopalkin muotoiluun, jolla saavutettiin optinen laatutekijä $Q \sim 10^6$ ja optomekaanisen kytkennän maksimi $g_0/2\pi = 4\,\mathrm{MHz}$. Nanopalkin liitoksiin lisättiin venymää kohdentava geometria, joka maksimoi nollapiste-energialla normalisoidun venymän $\varepsilon_{\mathrm{zpf}} > 10^{-9}$ ioni-implantaatiolle mahdollisella alueella. Venymä vastasi ^{31}P donoriatomin spin-fononi kytkentävoimakkuutta $\lambda_0 \sim 0.1\,\mathrm{kHz}$ kokeellisesti rajoitetussa magneettikentässä $B \leq 1\,\mathrm{T}$ ja fononien taajuudella $\Omega_{\mathrm{m}}/2\pi \leq 3\,\mathrm{MHz}$. Kytkentävoimakkuus ei ollut vielä riittävä yksittäisen spin-tilan mittaamiseen. Tulokset luovat pohjaa piinanopalkkien hyödyntämiselle kvanttiantureina.

Avainsanat: Optomekaniikka, nanopalkki, fotonikide, spinkytkentä

Preface

I have always been interested in a wide range of topics in physics, never choosing between theoretical and experimental work. Working with 3D simulations provided me with a knowledge bridging experience with one foot in theory and another in the framework experimental applications. Similarly, it allowed me the opportunity to stretch my mind into the quantum world while keeping my feet grounded in everyday engineering problems.

As is often the case in research, I spent more time learning and developing the tools necessary to carry out the simulations than with the simulations themselves. Sometimes trying to apply a multifunctional software like COMSOL on a specific problem felt like armwrestling a giant. Other times, I could get verifiable data from a moments inspiration in no time. Regardless of the ups and downs, I learned to appreciate the possibility autonomy and independence in simulations. To be able to apply physics at any time anywhere.

Many thanks go to my research team, who suffered through the long evenings with me: Cliona, Milla, Arvind and Antti for their experimental expertise, Charles for battling against tedious simulation problems, Henri for his encouraging counsels and an occasional dry anecdote, and of course my supervisor Juha for the opportunity to work as part of his team. Lastly, I thank my friends and family, who have kept me company in good spirit and revitalized the vision forward. I feel that working on the thesis as part of a research group has opened the doors to the research world, yet I know not what may spring out of it next.

Part of the journey is the end. But in an end lies a new beginning.

For your prosperity, dear reader.

Jyväskylä, May 29th, 2024

Simeoni Ahopelto

Contents

1 Introduction

How do you create a device that is able to reliably detect a change in the spin of a single electron? How is it possible to transfer the quantum information of a spin state to a photon? These questions are of a particular interest to the research fields of quantum metrology and sensing [1, 2], quantum information processing [3], communication, and quantum simulation [4]. Especially, with the start of the NISQ (Noisy, Intermediate-Scale Quantum) era in quantum computing [5], interest towards the search possible quantum technologies has grown substantially.

Our research group investigates atomic spins for their potential in serving as the basic building block of a quantum computers: **the qubit**. In short, a qubit can be any two-level quantum system that can be encoded with binary information i.e. an atom's nuclear or electronic spin, or a superconducting circuit. As opposed to normal classical bits, the state of a qubit is not well-defined as 1 or 0 before measurement. Instead, the qubit can exist in a superposition state, and only attains a definite value (0 or 1 with some probability distribution) when its state is measured and saved onto a classical bit. Keeping multiple interdependent qubits in an indeterminate state during computation allows quantum algorithms to consider multiple solution states simultaneously, albeit while losing information on definitive solution.

A number of physical quantum system have been proposed to serve as qubit platforms, including ion traps [6], nuclear magnetic resonance (NMR) [7], silicon donors [8], quantum dots [9], linear optics [10] and superconducting quantum electrodymamics (QED) [11]. The early commercial quantum computers mostly utilize superconducting qubits due to their manufacturability and controllability [12]. However, the functionalities of nascent quantum computers are still severely limited, and so it remains valuable to explore the limits of promising, alternative and integrable technologies.

What makes the group V (^{31}P, ^{75}As, ^{121}Sb, ^{127}Sb, ^{209}Bi) donor spins in silicon so attractive qubit candidates, is their long decoherence times and utilization of existing silicon fabrication technologies [13]. Decoherence measures the time a quantum state remains unperturbed by outside interference, and is directly related to the

performance of the qubit. Donor defect spins in silicon have been shown to possess decoherence times as long as 30 s for nuclear and 0.5 s for electron spin [14] compared to $< 100\,\mu$s in superconducting qubits [15]. Thus, donor spins in silicon provide a promising platform for the realization of qubits.

Notably, many of the applications envisioned for quantum technologies require the transmission of quantum states via photons of light. Photons are the natural medium for the transfer of quantum information, as they coherently preserve their quantum state while traveling at the universal speed limit. Photons also posess multiple degrees of freedom that can be utilized for encoding information [16]. Thus, it would be highly beneficial to the nascent quantum infrastructure, that a robust device, able to reliably transfer a quantum state from e.g. an electron spin to a photon (a so-called quantum bus), is realized.

The challenge is to create a deterministic or a heralded spin-photon interface at telecommunication frequencies [17] to be able to take advantage of the existing optical fiber infrastructure to create entangled quantum networks. The interface requires both transduction and storage of the quantum state [18]. Whereas the donor spin system can provide the long coherence memory, optomechanical resonators are recently investigated as an intermediary coupling device for their versatility in design [19]. For spin-resonator systems, vacancy centers in diamond have been studied [20] along with group V donor spins in silicon [3]. Alternative potential spin-photon interfaces include InGaAs quantum dots [21, 22] and T centres in silicon [23].

The sliced silicon nanobeam considered in this thesis is an optomechanical device that combines a mechanical beam resonator with a photonic crystal cavity [24]. A periodic silicon-hole patterning (a photonic crystal) allows the creation of an optical cavity that can be used to observe small displacements of the nanobeam through changes in optical resonance frequency. The displacements are caused by mechanical oscillations of the nanobeam. When the nanobeam is implanted with donor spins, its oscillation frequency shifts depending on the donor spin direction in an external magnetic field. If the shift in mechanical frequency is significant enough, it can be measured from the changes in optical frequency.Figure 1 illustrates the working principle of such device.

This thesis considers the performance optimization of a sliced silicon nanobeam, that works as a spin-to-photon transducer via a mechanically resonating optical cavity [25–27]. Chapter 2 starts with the description and preparation of a donor spin

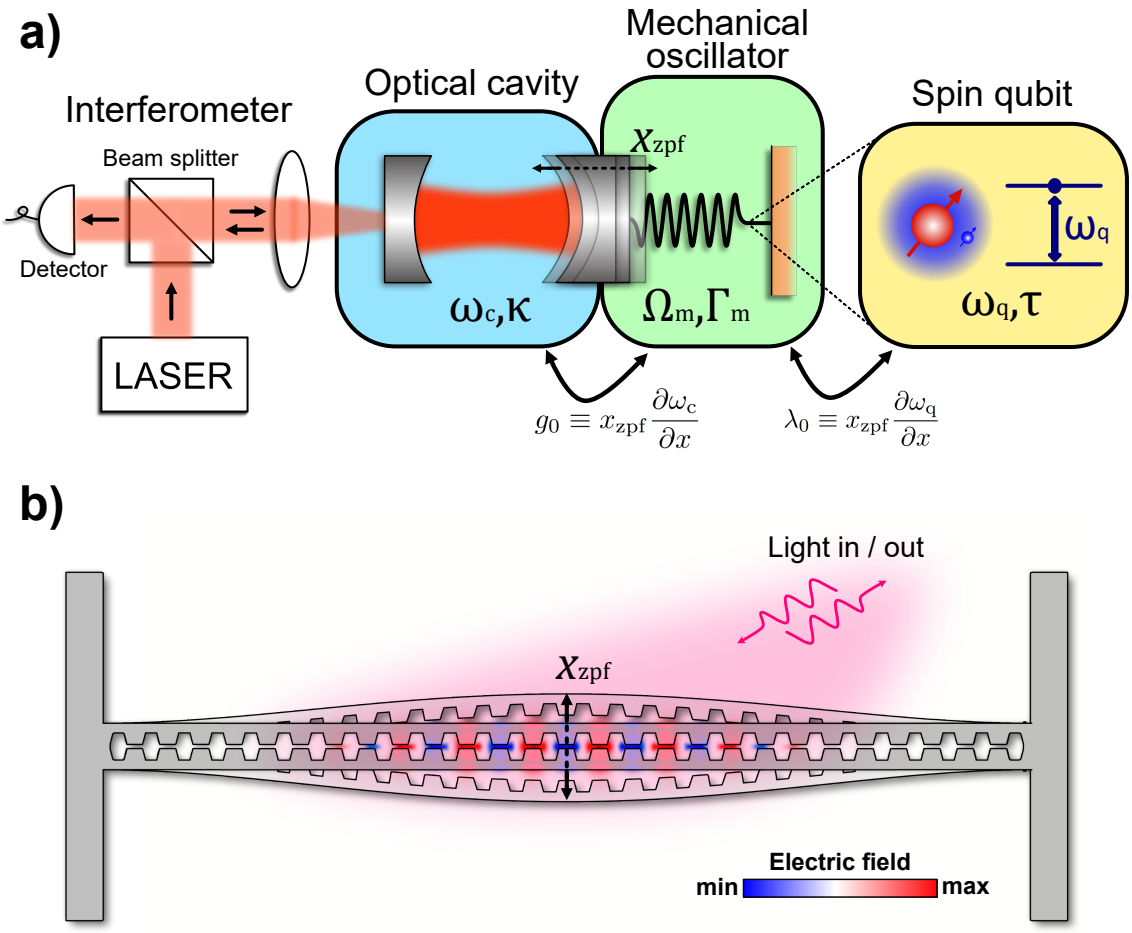

Figure 1. a) An illustration of the coupling between three different quantum systems: an optical cavity, a mechanical oscillator, and atomic spins. The optical cavity is driven with an external light source. The photons in the cavity exert a radiation pressure on the unfixed mirror causing it to oscillate. Displacement in the oscillating mirror causes the cavity resonance frequency to shift. Additionally, the displacement in the oscillating mirror alters the internal resonance frequencies of atomic spins through their strain or magnetic field dependence. The coupling constants g_0 and λ_0 correspond to the frequency shifts per unit of displacement. The frequencies ω_c, Ω_m, and ω_q describe the optical, mechanical, and spin resonances with their respective decay rates κ, Γ_m, and $1/\tau$. **b)** The sliced silicon nanobeam with its resonant electric field mode and displacement x_{zpf} at the beam center.

qubit in silicon. Section 2.2 presents how the spin qubit can alter the mechanical resonance frequency of a nanobeam. Sections 2.3 and 2.4 discuss the properties and performance measures of optical photonic crystal cavities and the optomechanical coupling. Chapter 3 dives into the finite elements method (FEM) simulations used for the optimization. Finally, chapter 4 presents the simulated results and viable designs of the nanobeam. For quick readers, the main results are collected in chapter 5.

2 Theoretical background

2.1 Donor spin in silicon as a qubit

Group V donors in silicon (^{31}P, ^{75}As, ^{121}Sb, ^{127}Sb, ^{209}Bi) have been shown to have spin systems suitable to serve as a platform for qubits. The following chapter outlines the simplest spin system of ^{31}P donor, and how the the system needs to be prepared for spin measurements. For more detailed description of spins as qubits, see [13, 28].

2.1.1 The donor spin system

In an environment with no magnetic fields, the spin states of a single electron or nucleus are degenerate i.e. they cannot be distinguished energetically. In order to separate the spin states, the donor atoms are placed in a external magnetic field. The nuclear and electron spins align either along or against the magnetic field lines, and split the spin states to lower and higher energy states respectively. The phenomena is known as the Zeeman effect. The resulting energy separation for a single spin is

$$\omega_{e,N} = \gamma_{e,N} B_0, \tag{1}$$

where B_0 is the external magnetic field, $\gamma_e = g\mu_B/\hbar$ is the gyromagnetic ratio (GMR) for the electron with its g-factor and Bohr magneton μ_B. Similarly for nuclear spins, $\gamma_N = g_N\mu_N/\hbar$ with the nuclear g-factor g_N and nuclear magneton μ_N. Additionally, when we have a nucleus-electron system, such as that of a donor ^{31}P atom in silicon, we have to also take into account the hyperfine interaction $A\hat{S}\cdot\hat{I}$ between the electron $\hat{S}$ and nuclear $\hat{I}$ spins, where A is the (isotropic) hyperfine interaction strength. The Hamiltonian describing the energy of nucleus-electron system is

$$\mathcal{H} = (\gamma_e\hat{S}_z - \gamma_N\hat{I}_z)B_0 + A\hat{S}\cdot\hat{I}, \tag{2}$$

where $\hat{S}_z$ and $\hat{I}_z$ are the spin projections along the magnetic field direction. Equation (2) forms a linear system that can be a bit tedious to solve, especially for system with higher spin numbers like ^{209}Bi, as seen in [13, p.45]. However, a so-called

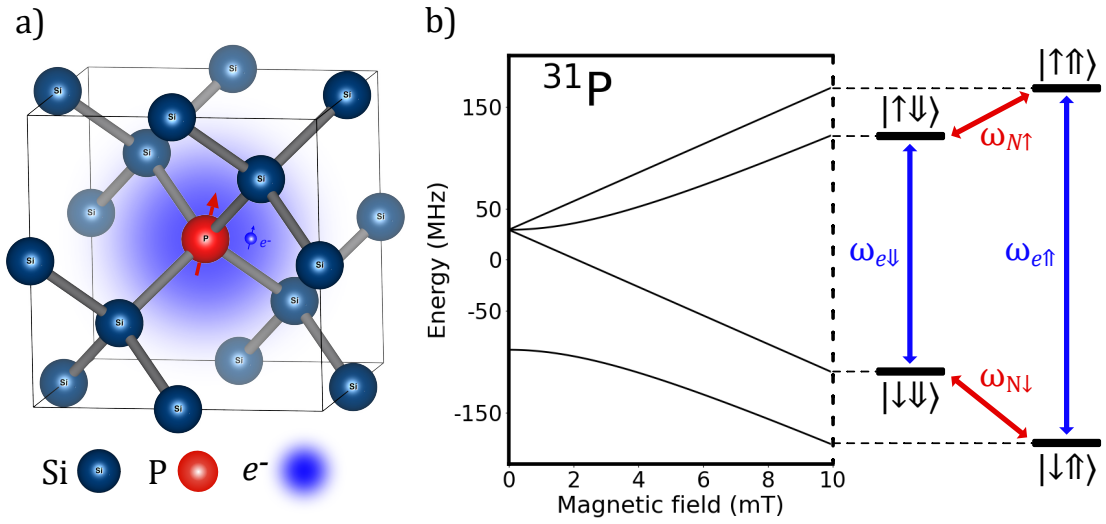

Figure 2. **a)** Silicon crystal with a diamond cubic lattice and a ^{31}P donor defect. The electron wavefunction extends over multiple atoms in the lattice. **b)** The energy splitting of ^{31}P spin states with increasing magnetic field [13], and the resulting nucleus-electron spin system with corresponding electron (blue) and nuclear (red) spin transitions. The electron and nuclear spin states are noted with $|\uparrow\rangle$ and $|\Uparrow\rangle$.

Table 1. Properties of group V spin system [13]

	^{31}P	^{75}As	^{121}Sb	^{123}Sb	^{209}Bi
Nuclear spin I	1/2	3/2	5/2	7/2	9/2
Electron GMR γ_e (GHz/T)	27.972	27.970	27.973	27.973	27.997
Nuclear GMR γ_N (MHz/T)	17.23	7.3	10.26	5.6	6.9
Hyperfine interaction A_0 (MHz)	117.5	198.3	186.8	101.5	1475.2

high-field approximation $\gamma_e \gg A > \gamma_N$, accurate at high magnetic fields, can be used to simplify and cancel the off-diagonal terms. The experimental values for nuclear spins, gyromagnetic ratios, and hyperfine interaction strengths can be found in Table 1.

For the simplest spin system of ^{31}P, the eigenenergies corresponding to equation (2) are

$$E_{\downarrow\Uparrow} = \frac{-\sqrt{(\gamma_e + \gamma_N)^2 B_0 - A/2}}{2}, \tag{3}$$

$$E_{\downarrow\Downarrow} = \frac{-(\gamma_e - \gamma_N)B_0 + A/2}{2}, \tag{4}$$

$$E_{\uparrow\Downarrow} = \frac{\sqrt{(\gamma_e + \gamma_N)^2 B_0 - A/2}}{2}, \tag{5}$$

$$E_{\uparrow\Uparrow} = \frac{(\gamma_e - \gamma_N)B_0 + A/2}{2} \tag{6}$$

where the notation $|1\rangle \otimes |0\rangle = |\uparrow\rangle \otimes |\Downarrow\rangle = |\uparrow\Downarrow\rangle$ is used for the electron and nucleus spin states corresponding to Figure 2 b). The transition frequencies with fixed nuclear spin ω_e and fixed electron spin ω_N are then

$$\omega_{e\Uparrow} = E_{\uparrow\Uparrow} - E_{\downarrow\Uparrow} = \gamma_e B_0 + A/2, \tag{7}$$

$$\omega_{e\Downarrow} = E_{\uparrow\Downarrow} - E_{\downarrow\Downarrow} = \gamma_e B_0 - A/2, \tag{8}$$

$$\omega_{N\uparrow} = E_{\uparrow\Downarrow} - E_{\uparrow\Downarrow} = A/2 - \gamma_N B_0, \tag{9}$$

$$\omega_{N\downarrow} = E_{\uparrow\Uparrow} - E_{\downarrow\Uparrow} = A/2 + \gamma_N B_0. \tag{10}$$

From these frequencies we can choose one as our qubit resonance frequency ω_q.

2.1.2 Dressing the qubit

To achieve a more tunable level splitting and longer coherence times, a "dressing" protocol is can be used [29], where an additional oscillating magnetic field of amplitude B_1 is applied orthogonal to the static field B_0. Treating the chosen ω_q as a single spin in magnetic field, the Hamiltonian of the system will now be

$$\mathcal{H}/\hbar = \omega_\mathrm{q}\hat{\sigma}_z + B_1 \cos(\omega_1 t)\hat{\sigma}_x, \tag{11}$$

where ω_1 is the magnetic field oscillation frequency, and $\hat{\sigma}_x$,$\hat{\sigma}_z$ are Pauli matrices. A time-independent solution for equation (11) can be derived by a change of basis from stationary $|\Psi_{\text{stat}}\rangle$ to rotating $|\Psi_{\text{rot}}\rangle = e^{i\omega_1 t}|\Psi_{\text{stat}}\rangle$ and solving for time dependent Schrödinger equation. This is equivalent to a frame change from a fixed laboratory frame to a rotating frame, traveling along the spin's Lamor precession around its own axis. A more detailed derivation can be found in [13, p.30]. As a result, the Hamiltonian will change to

$$\mathcal{H}/h = (\omega_1 - \omega_{\text{q}})\hat{\sigma}_z + \Omega_{\text{R}}\hat{\sigma}_x, \tag{12}$$

where $(\omega_1 - \omega_{\text{q}})$ is the detuning of the oscillating field from spin resonance and $\Omega_{\text{R}} = \frac{1}{2}\gamma B_1$ the system's Rabi frequency. The Rabi frequency describes the system's alternating oscillations between its eigenstates. The corresponding eigenenergies of the Hamiltonian (12) are

$$\text{E}_{\pm} = \pm\sqrt{(\omega_1 - \omega_{\text{q}})^2 + \Omega_{\text{R}}^2}. \tag{13}$$

However, they are in a different basis defined by

$$|+\rangle = \frac{|\uparrow\rangle + |\downarrow\rangle}{\sqrt{2}}, \tag{14}$$

$$|-\rangle = \frac{|\uparrow\rangle - |\downarrow\rangle}{\sqrt{2}}. \tag{15}$$

Here, we can see that the energy splitting can be tuned with the strength of the oscillating field B_1. In section 2.2.2 we will see that the Rabi frequency Ω_{R} needs to be matched close to the frequency Ω_{m} of our mechanical resonator to achieve higher spin coupling. Interestingly, this creates a limiting factor for the mechanical frequency of our nanobeam resonator. In a practical measurement setup, the driving supply power P_{s} of the magnet is proportional to $\sqrt{P_{\text{s}}} \propto B_1 \propto \Omega_{\text{R}}$ for which the highest attained Rabi frequency around 3.3 MHz [28, p.76]. Moreover, the supplied driving power needs to be high enough for the Rabi frequency to exceed linewidth of the bare electron spin resonance (ESR). The ESR linewidths are around $\Delta\omega_{\text{q}} \sim 1\,\text{MHz}$ in natural silicon, but much lower in isotopicly purified silicon [28, p.32]. The linewidth is caused by the decoherence effects to the bare spin qubit state, such as dephasing

[28, p.26]. Thus, if we want the spin flipping to be detectable in our resonator, the mechanical resonance frequency is constrained by

$$\frac{\Omega_{\mathrm{m}}}{2\pi} \leq 1\text{–}\,3\,\mathrm{MHz}. \tag{16}$$

2.2 Nanobeam as a mechanical resonator

Mechanical beams are one of the most studied harmonic oscillators. Here we show how a doubly-clamped silicon nanobeam (of length $L \sim 10\,\mu$m) can be coupled to a donor spin. The derivations are based on previous works by Leijssen [25] and van der Hel [27]. For reviews on nanomechanical resonators, see for example [30].

2.2.1 Properties of mechanical resonators

Firstly, the most important properties of mechanical oscillators are the mechanical oscillation frequencies Ω_m, mechanical damping rate Γ_m and effective mass m_eff. We are interested in these properties of the fundamental breathing mode of the sliced nanobeam in Figure 3, since it can be optically coupled by confining a high electric field and radiation pressure at the nanobeam's center.

As for the mechanical modes, the frequency of a mode n in a uniform rectangular beam with double clamping can be modeled analytically using the deflection equation in Euler-Bernoulli elasticity theory, for which the frequency solutions are of the form [31]

$$\frac{\Omega_n}{2\pi} = \frac{\beta_n^2}{2\pi}\sqrt{\frac{E}{12\rho}}\frac{w}{L^2}, \tag{17}$$

where $E \approx 124\,\mathrm{GPa}$ is Young's modulus for silicon, $\rho \approx 2329\,\mathrm{kg/m^3}$ is the density of silicon, L is beam length, w is beam width (to oscillation direction), and β_n are constants. In this elasticity model the frequencies are unaffected by the beam thickness i.e. thickness of the silicon layer. For the fundamental mode $\beta_1 \approx 4.73$ [25, p.51], which gives the fundamental flexural mode frequency

$$\Omega_\mathrm{m} \equiv \Omega_1 \sim \frac{w}{L^2} \cdot 7500\,\mathrm{Hz\ m}. \tag{18}$$

This result combined with the restriction in equation 16 gives approximate constraints to the nanobeam size.

Secondly, the frequency of a harmonic oscillator can also be expressed as

$$\Omega_\mathrm{m} = \sqrt{\frac{k}{m_\mathrm{eff}}}, \tag{19}$$

where k is structure dependent stiffness, and m_eff is the effective mass. Since we would like to keep the resonator frequency in the range of equation 16, its dependence

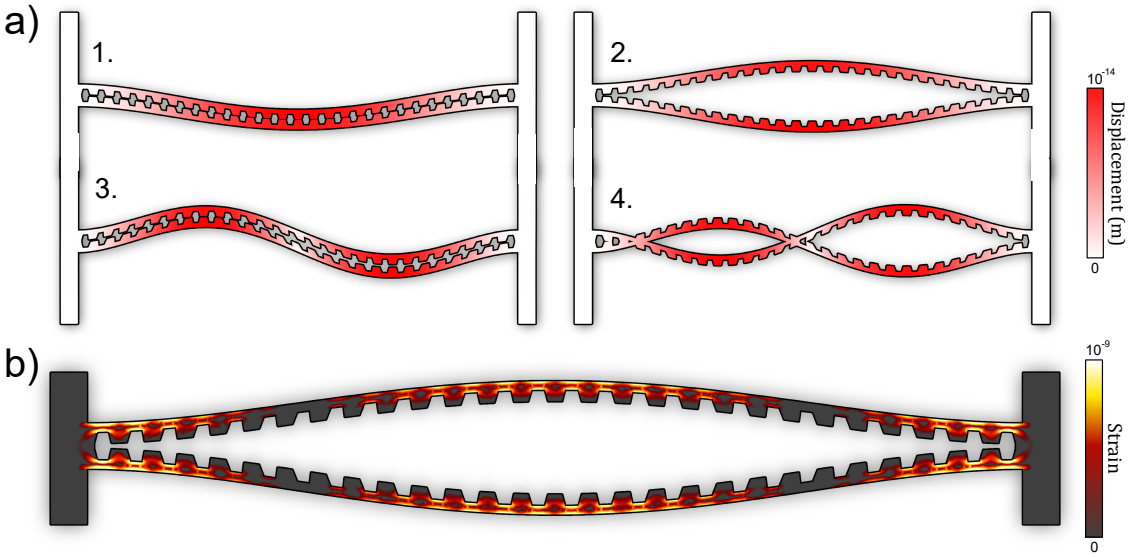

Figure 3. a) Mechanical in-plane eigenfrequency modes of a sliced nanobeam resonator with a zipper-like design. The mechanical mode 2 (referred to as the breathing mode) is the one we are interested in. The breathing mode has the lowest frequency with the highest displacement amplitude, and it is suitable to be optically driven with radiation pressure by creating an optical cavity at the center of the nanobeam. **b)** The simulated strain distribution of the breathing mode. The areas with the highest absolute strain are suitable spin-strain coupling, whereas the areas with the highest displacement favor spin-magnetic field coupling.

on the effective mass has to also be taken into account in the design. The effective mass is equal to the oscillating mass of a mechanical mode (see Figure 3 a) for the displacement profiles) and is calculated by weighing each infinitesimal mass element dm by its displacement [32, p.49]

$$m_{\text{eff}} = \frac{1}{x_{\text{max}}^2} \int \mathbf{U}^2(\mathbf{r}) \mathrm{d}m, \tag{20}$$

where $\mathbf{U}(\mathbf{r})$ is the displacement profile for a particular mechanical mode, which is usually normalized by the highest displacement amplitude x_{max} of the mode. For uniform beams, the estimated estimated effective mass of the fundamental breathing mode is $m_{\text{eff}} \simeq 0.396\, m_{\text{total}}$ of the beam. FEM simulations show that the zipper-like design is not far off of this estimation $m_{\text{eff}} \simeq 0.398\, m_{\text{total}}$.

Finally, the time-evolution of an externally driven nanobeam is classically described by a damped harmonic oscillator with the equation of motion

$$m_{\text{eff}}\ddot{x} + m_{\text{eff}}\Gamma_{\text{m}}\dot{x} + m_{\text{eff}}\Omega_{\text{m}}^2 x = F_{\text{ext}}(t), \tag{21}$$

where F_{ext} is the driving force, and Γ_{m} is the damping rate. The damping rate can be understood to correspond to the exponential decay of the oscillation amplitude $x(t) = e^{-\Gamma_{\text{m}} t}\cos(\Omega_{\text{m}} t)$. It also describes the linewidth $\Gamma_{\text{m}} = \Delta\Omega_{\text{m}}$ (full width at half maximum) of a resonator's frequency. For many resonators, keeping the damping rate low is essential for device performance. Conventionally, a scale-invariant and dimensionless measure called the quality factor (or Q-factor) is used in its stead

$$Q_{\text{m}} = \frac{\Omega_{\text{m}}}{\Gamma_{\text{m}}}. \tag{22}$$

The Q-factor is proportional the number of oscillations in the cavity before its decay.

In order to distinguish the effect of donor spins on the resonance, it is necessary for the spin-affected frequency change to be larger than the mechanical linewidth $\delta\Omega_{\text{m}} > \Delta\Omega_{\text{m}}$. Otherwise, one cannot separate the frequency change from the initial peak in a frequency measurement. In experimental conditions, the mechanical linewidth of the nanobeam tends to be around $\Delta\Omega_{\text{m}} \sim 200\,\text{Hz}$ [25, p.118].

2.2.2 Coupling spins to displacement

Considering the nanobeam as a harmonic oscillator, the energy-quantized Hamiltonian can be written as

$$\mathcal{H}_{\mathrm{m}}/\hbar = \Omega_{\mathrm{m}} \left(\frac{1}{2} + \hat{b}^{\dagger}\hat{b} \right), \tag{23}$$

where Ω_{m} is the frequency of the oscillator, and $n = \hat{b}^{\dagger}\hat{b}$ the total number of phonons with $\hat{b}^{\dagger}$ and $\hat{b}$ being the phonon creation and annihilation operators. Combining the spin system in equation (12) with the mechanical resonator in equation (23) results in the Hamiltonian

$$\mathcal{H}/\hbar = \Omega_{\mathrm{m}}\hat{b}^{\dagger}\hat{b} + \Omega_{\mathrm{R}}\hat{\sigma}_x + (\omega_1 - \omega_{\mathrm{q}})\hat{\sigma}_z, \tag{24}$$

where the zero-point energy $\Omega_{\mathrm{m}}/2$ is neglected. If we assume that a displacement of the nanobeam can change the qubit frequency, we can add a linear first-order estimation of the change in spin frequency $\partial\omega_{\mathrm{q}}$ caused by a small displacement ∂x of the nanobeam's center by Taylor expansion

$$\omega_{\mathrm{q}} \approx \omega_{\mathrm{q}} + \hat{x}\frac{\partial\omega_{\mathrm{q}}}{\partial x} + \mathrm{O}(x^2), \tag{25}$$

where $\mathrm{O}(x^2)$ contains the remaining second-or-higher order error terms, which can be discarded since the displacements are fairly tiny $\sim 10^{-13}$ in silicon nanobeams. Here, the displacement operator $\hat{x}$ is defined as

$$\hat{x} \equiv x_{\mathrm{zpf}}(\hat{b}^{\dagger} + \hat{b}), \tag{26}$$

with the zero-point fluctuation x_{zpf} of a mechanical oscillator

$$x_{\mathrm{zpf}} = \sqrt{\frac{\hbar}{2m_{\mathrm{eff}}\Omega_{\mathrm{m}}}}, \tag{27}$$

where m_{eff} is the effective mass of the oscillator. Continuing our derivation of the Hamiltonian we plug the first-order approximation 25 into the system 24

$$\mathcal{H}/\hbar = \Omega_{\mathrm{m}}\hat{b}^{\dagger}\hat{b} + \Omega_{\mathrm{R}}\hat{\sigma}_x + (\omega_1 - \omega_{\mathrm{q}})\hat{\sigma}_z + x_{\mathrm{zpf}}\frac{\partial\omega_{\mathrm{q}}}{\partial x}(\hat{b}^{\dagger} + \hat{b})\hat{\sigma}_z. \tag{28}$$

Next we assume that the oscillating magnetic field is on resonance with the spin qubit $\omega_1 - \omega_{\mathrm{q}} = 0$ and rotate the basis with a transformation $e^{-i\pi\hat{\sigma}_y}\left|\Psi\right\rangle$ changing

$\hat{\sigma}_x \to \hat{\sigma}_z$ and $\hat{\sigma}_z \to -\hat{\sigma}_x$. The Hamiltonian becomes

$$\mathcal{H}/\hbar = \Omega_{\mathrm{m}}\hat{b}^\dagger\hat{b} + \Omega_{\mathrm{R}}\hat{\sigma}_z - x_{\mathrm{zpf}}\frac{\partial\omega_{\mathrm{q}}}{\partial x}(\hat{b}^\dagger + \hat{b})\hat{\sigma}_x. \tag{29}$$

Finally, to derive the coupling, we use $\hat{\sigma}_x \equiv \frac{1}{2}(\hat{\sigma}_+ + \hat{\sigma}_-)$ and omit the terms $\hat{b}^\dagger\hat{\sigma}_+$ and $\hat{b}\hat{\sigma}_-$ that break energy conservation (interactions where both a spin state is excited and a phonon created, or both are de-excited) to get

$$\mathcal{H}/\hbar = \Omega_{\mathrm{m}}\hat{b}^\dagger\hat{b} + \Omega_{\mathrm{R}}\hat{\sigma}_z - \frac{1}{2}x_{\mathrm{zpf}}\frac{\partial\omega_{\mathrm{q}}}{\partial x}(\hat{b}^\dagger\hat{\sigma}_- + \hat{b}\hat{\sigma}_+). \tag{30}$$

Equation (30) corresponds to the Jaynes-Cummings model of the interaction between an atom and a boson [33]. Here, we can see that the coupling between mechanical phonons and spin is defined by the terms $\hat{b}^\dagger\hat{\sigma}_-$ and $\hat{b}\hat{\sigma}_+$ where a phonon and a spin excitation are exchanged. Now, we can define the coupling strength between the mechanical resonator and the spin qubit as

$$\lambda_0 \equiv x_{\mathrm{zpf}}\frac{\partial\omega_{\mathrm{q}}}{\partial x}. \tag{31}$$

The eigenenergies corresponding to equation (30) are easily solved by separating the Hamiltonian into two commuting parts

$$\mathcal{H} = \mathcal{H}_1 + \mathcal{H}_2, \tag{32}$$

where the Hamiltonians are

$$\mathcal{H}_1/\hbar = \Omega_{\mathrm{m}}\left(\hat{b}^\dagger\hat{b} + \frac{\hat{\hat{\sigma}}_z}{2}\right), \tag{33}$$

$$\mathcal{H}_2/\hbar = (\Omega_{\mathrm{R}} - \Omega_{\mathrm{m}})\frac{\hat{\sigma}_z}{2} - \frac{\lambda_0}{2}\left(\hat{b}\hat{\sigma}_+ + \hat{b}^\dagger\hat{\sigma}_-\right). \tag{34}$$

The resulting eigenenergies for equation (30) are then

$$E_\pm/\hbar = \left(n + \frac{1}{2}\right)\Omega_{\mathrm{m}} \pm \frac{1}{2}\sqrt{(\Omega_{\mathrm{R}} - \Omega_{\mathrm{m}})^2 - \lambda_0^2(n+1)}, \tag{35}$$

where $n = \hat{b}^\dagger\hat{b}$ is the number of phonons. We want to estimate the coupling strength λ_0 and its effect on the mechanical frequency Ω_{m}. We evaluate a differential equation

$$\frac{\partial \Omega_\mathrm{m}}{\partial \lambda_0} = \frac{\partial \Omega_\mathrm{m}}{\partial E_\pm}\frac{\partial E_\pm}{\partial \lambda_0} = \pm\frac{\lambda_0}{\sqrt{(\Omega_\mathrm{R}-\Omega_\mathrm{m})^2+\lambda_0^2}}, \tag{36}$$

where the number of phonons n may be omitted. Thus, the measurable change to the mechanical frequency of the resonator is

$$\delta\Omega_\mathrm{m} = \pm\frac{\lambda_0^2}{\sqrt{(\Omega_\mathrm{R}-\Omega_\mathrm{m})^2+\lambda_0^2}}, \tag{37}$$

where we notice that the effect of coupling is heavily dependent on the Rabi detuning $(\Omega_\mathrm{R}-\Omega_\mathrm{m})$ between the Rabi and mechanical oscillations. When the detuning goes to zero, the mechanical frequency changes is directly proportional to the coupling strength $\delta\Omega_\mathrm{m} \sim \lambda_0$, whereas with high detuning the frequency shift is similar to $\delta\Omega_\mathrm{m} \sim \frac{\lambda_0^2}{\Omega_\mathrm{R}-\Omega_\mathrm{m}}$.

For experimental Rabi detunings, limited mainly by thermal noise to a range of $\sim$ 1–100 kHz [29] and mechanical linewidths of 200 Hz [25, p.118], the required coupling strength is around $\lambda_0 \geq$ 0.5–5 kHz. A more realistic approximation of $\lambda_0 \geq 1-10$ kHz can be derived using the time evolution of Lindblad master equation [34], which takes into account the inherent uncertainties of the system, such as the linewidth of the spin resonance.

Also, for the equation (31), there is no direct coupling between the spin resonance ω_q and the displacement ∂x of the beam's center. From equations (7) – (10) we can deduce that the spin resonance is affected by change in magnetic field or the hyperfine strength. The hyperfine strength in a silicon lattice has been shown to change with the mechanical straining of the lattice [35]. Thus, the spin resonance can be altered at least in two ways: by displacement in a magnetic field with steep gradient, or by the straining of silicon lattice caused by deformations in the nanobeam. Next, we shall explore the effects of these two ways of coupling.

2.2.3 Strain coupling

When a silicon lattice is mechanically strained, the band structure of silicon changes. As strain displaces the lattice atoms, it modifies the donor electron wavefunction and causes perturbations in the donor's hyperfine strength A and electron g-factor [35]. We want to estimate the effects of these perturbations on our spin coupling strength λ_0.

Expanding the differential part of our spin coupling strength in equation (31) with unidimensional component ε_{xx} of volumetric strain $\varepsilon = (\varepsilon_{xx} + \varepsilon_{yy} + \varepsilon_{zz})/3$ gives

$$\frac{\partial \omega_\mathrm{q}}{\partial x} = \frac{\partial \omega_\mathrm{q}}{\partial \varepsilon_{xx}} \frac{\partial \varepsilon_{xx}}{\partial x} \simeq \frac{\partial \omega_\mathrm{q}}{\partial \varepsilon_{xx}} \frac{\varepsilon_{xx}^\mathrm{sim}}{x^\mathrm{sim}}, \tag{38}$$

where the values for strain $\varepsilon_{xx}^\mathrm{sim} \sim 10^{-9}$ and displacement $x^\mathrm{sim} \sim 10^{-13}$ remain to be optimized with simulations. The strain coupling $\partial\omega_\mathrm{q}/\partial\varepsilon_{xx}$ itself is somewhat more cumbersome to model analytically. Fortunately, Mansir et al.[35] have provided experimental data by straining a silicon in a magnetic field, and modeling its hyperfine coupling and g-factor ansiotropy using valley repopulation model (VRM). Notably, the hyperfine strength changes linearly with small strains. Additionally to the VRM effects, shear strain also changes the g-factor. The resulting strain coupling is given as

$$\frac{\partial \omega_\mathrm{q}}{\partial \varepsilon_{xx}} = \frac{\partial A}{\partial \varepsilon_{xx}} \frac{\partial \omega_q}{\partial A} + \left[\left. \frac{\partial g}{\partial \varepsilon_{xx}} \right|_\mathrm{VRM} + \left. \frac{\partial g}{\partial \varepsilon_{xx}} \right|_\mathrm{shear} \right] \frac{\partial \omega_q}{\partial g}, \tag{39}$$

with the strain coupling differentials equal to

$$\frac{\partial A}{\partial \varepsilon_{xx}} = K A_0, \tag{40}$$

$$\left. \frac{\partial g}{\partial \varepsilon_{xx}} \right|_\mathrm{VRM} = \beta_\mathrm{VRM}(3\cos^2\theta - 1), \tag{41}$$

$$\left. \frac{\partial g}{\partial \varepsilon_{xx}} \right|_\mathrm{shear} = \beta_\mathrm{shear}(3\cos^2\theta - 3), \tag{42}$$

where θ is the angle silicon lattice and the magnetic field ($B \perp [001] : \theta = 0°$ and $B \perp [0\bar{1}1] : \theta = 90°$), and the constant $\beta_\mathrm{shear}, \beta_\mathrm{VRM}$, and K are given in Table 2. Choosing the best case scenario, where $\omega_\mathrm{q} = \omega_{e\Downarrow} = g\mu_\mathrm{B}/\hbar - A/2$ and $\theta = 90°$, where the effect of electron g-factor maximises, the strain coupling can now be expressed as

Table 2. Best values of experimental constants for donor strain coupling in silicon from [35].

	K	$\beta_{\mathrm{VRM}} \cdot 10^{-3}$	$\beta_{\mathrm{shear}} \cdot 10^{-3}$
^{31}P	79.2	206.51	173
^{75}As	37.4	165.1	96
^{121}Si	32.8	197.6	90.3
^{201}Bi	19.1	-	-

$$\frac{\partial \omega_{\mathrm{q}}}{\partial \varepsilon_{xx}} = -\frac{KA_0}{2} - (\beta_{\mathrm{VRM}} + 3\beta_{\mathrm{shear}})\frac{\mu_{\mathrm{B}} B_0}{\hbar} \tag{43}$$

and the mechanical coupling strength

$$\lambda_{\mathrm{strain}} = -x_{\mathrm{zpf}} \left(\frac{KA_0}{2} + (\beta_{\mathrm{VRM}} + 3\beta_{\mathrm{shear}})\frac{\mu_{\mathrm{B}} B_0}{\hbar} \right) \frac{\varepsilon_{xx}^{\mathrm{sim}}}{x^{\mathrm{sim}}}. \tag{44}$$

Notably, the effect of electron g-factor increases with the strength of the magnetic field. Thus, for higher fields the strain coupling becomes more plausible. Plugging in the experimental values for ^{13}P from Tables 1 and 2, and assuming that the simulated displacement can be normalized so that $x^{\mathrm{sim}} = x_{\mathrm{zpf}}$, the strain coupling reduces to

$$\lambda_{\mathrm{strain}} = (4.653\,\mathrm{GHz} + 63.512\,\mathrm{GHz/T} \cdot B_0)\, \varepsilon_{xx}^{\mathrm{zpf}}, \tag{45}$$

where $\varepsilon_{xx}^{\mathrm{zpf}}$ is the zero-point fluctuation strain. The experimentally achieved magnetic fields are approximately $B_0 \sim 1\,\mathrm{T}$. To achieve the desired spin-phonon coupling of $\lambda_0 \geq 1\,\mathrm{kHz}$ for single spin implantation, the requirement for strain is approximately

$$\varepsilon_{xx}^{\mathrm{zpf}} \geq 1.5 \cdot 10^{-8},$$

in a sufficiently large volume for a robust ion implantation.

2.2.4 Magnetic field coupling

Alternatively, the spin resonance can be altered by having a high magnetic field gradient near the nanobeam. This can be achieved e.g. by adding a magnet close to the displaced beam. Then the differential part of equation (31) becomes

$$\frac{\partial \omega_{\mathrm{q}}}{\partial x} = \frac{\partial \omega_{\mathrm{q}}}{\partial B}\frac{\partial B}{\partial x} = \gamma_e \nabla B_x^{\mathrm{sim}}, \tag{46}$$

where $\nabla B_x^{\mathrm{sim}}$ is the magnetic gradient to the direction of the displacement near the donor spin. The corresponding mechanical coupling strength

$$\lambda_{\mathrm{mag}} = x_{\mathrm{zpf}}\ \gamma_e \nabla B_x^{\mathrm{sim}}, \tag{47}$$

and the requirement for a change of the magnetic field

$$\nabla B_x^{\mathrm{sim}} x_{\mathrm{zpf}} \geq 36\,\mathrm{nT} \tag{48}$$

Next, we will see how the coupling strength scales with multiple donor spins.

2.2.5 Scaling the coupling with N donor spins

Due to the weakness of the spin-phonon coupling, the effect of a group V single spin on mechanical resonance has not yet been observed with optical measurement. As an intermediary step and proof-of-concept, the silicon can be doped with multiple donor spins. Here we want to derive how the coupling strength λ_0 scales with a system of N spins. We will start by defining macroscopic spin operators

$$S_\alpha = \sum_{i=1}^{N} \hat{\sigma}_\alpha^{(i)}, \ \text{with} \ \ \alpha = x,y,z\ , \tag{49}$$

so that we can present the Hamiltonian (30) as a multiple spin system

$$\mathcal{H}_N/\hbar = \Omega_{\mathrm{m}} \hat{b}^\dagger \hat{b} + \Omega_{\mathrm{R}} S_z + \frac{1}{2}\lambda_0 (\hat{b}^\dagger S_- + \hat{b} S_+), \tag{50}$$

which is also known as the Dicke or Tavis-Cummings model [36–38]. Notably, adding indistinguishable spins into the system creates a kond of "degeneracy" of energy states in the system up to the total number of spins N. Importantly, the spin ensemble will start to resemble a bosonic system in their excitation with increasing N. Then, we can define the macrospin operators in terms of bosonic spin excitation and de-excitation operators $\hat{s}^\dagger, \hat{s}$ also known as the Holstein-Primakoff transformation [39]

$$S_+ = \hat{s}^\dagger (N - \hat{s}^\dagger \hat{s})^{1/2}, \quad S_- = (N - \hat{s}^\dagger \hat{s})^{1/2} \hat{s} \quad \text{and} \quad S_z = \hat{s}^\dagger \hat{s} - \frac{N}{2}. \tag{51}$$

Substituting equation (51) into (50), and neglecting the terms $\hat{s}^\dagger \hat{s}/N$ compared to unity will result in the Hamiltonian

$$\mathcal{H}_N/\hbar \simeq \Omega_{\rm m}\hat{b}^\dagger\hat{b} + \Omega_{\rm R}\left(\hat{s}^\dagger\hat{s} - \frac{N}{2}\right) + \frac{1}{2}\lambda_0\sqrt{N}(\hat{b}^\dagger\hat{s} + \hat{b}\hat{s}^\dagger), \tag{52}$$

from which we can see that the coupling strength scales by

$$\lambda_{\rm total} \propto \lambda_0\sqrt{N} \tag{53}$$

with N donor spins.

2.3 Optomechanics

Here, we only introduce the necessary concepts of optical cavities to understand cavity coupling. For cavity optomechanics, a good overview is a known review by Aspelmeyer et al. [40]. For the optomechanical dynamics and measurements of the nanobeam, see [24, 41].

2.3.1 Properties of optical cavities

Optical cavities are formed by confining light between reflective mirrors. The simplest cavity formed by two opposing mirrors is often referred to as a Fabry-Pérot cavity. As photon are prevented from escaping the confines of the mirrors, the cavity can be driven by an external light source to create high electromagnetic (EM) fields.

Similar to the harmonic mechanical oscillator, optical cavities are identified and compared most commonly by their resonance frequency ω_c, and the decay rate κ. Resonance in the cavity takes place when the light reflected between mirrors interferes constructively with itself i.e. when the phase of the EM-waves aligns coherently. This means that an integer n multiple of half-wavelengths $\lambda/2$ has to fit exactly into the cavity length L

$$n\frac{\lambda}{2} = L. \tag{54}$$

Thus, an optical cavity contains a series of resonant frequencies

$$\omega_n = n\frac{\pi c}{L}, \tag{55}$$

where we used $\omega/2\pi = c/\lambda$ with the speed of light c. One can understand the optical cavity resonance as a plane wave inside the cavity, with electric field component

$$\mathbf{E} = E_0 e^{i(\mathbf{k}\cdot\mathbf{x}-\omega_c t)}, \tag{56}$$

where E_0 is the electric field amplitude, $\mathbf{k}$ is the wavevector containing wavenumbers with spatial distance $\mathbf{x}$, time t, and cavity frequency ω_c. However, no material interface is a perfect reflector, so the EM-field in the cavity will decay with time. One way to model the decay rate κ is with a complex frequency [32, p.131]

$$\omega_c = \omega_0 + i\kappa, \tag{57}$$

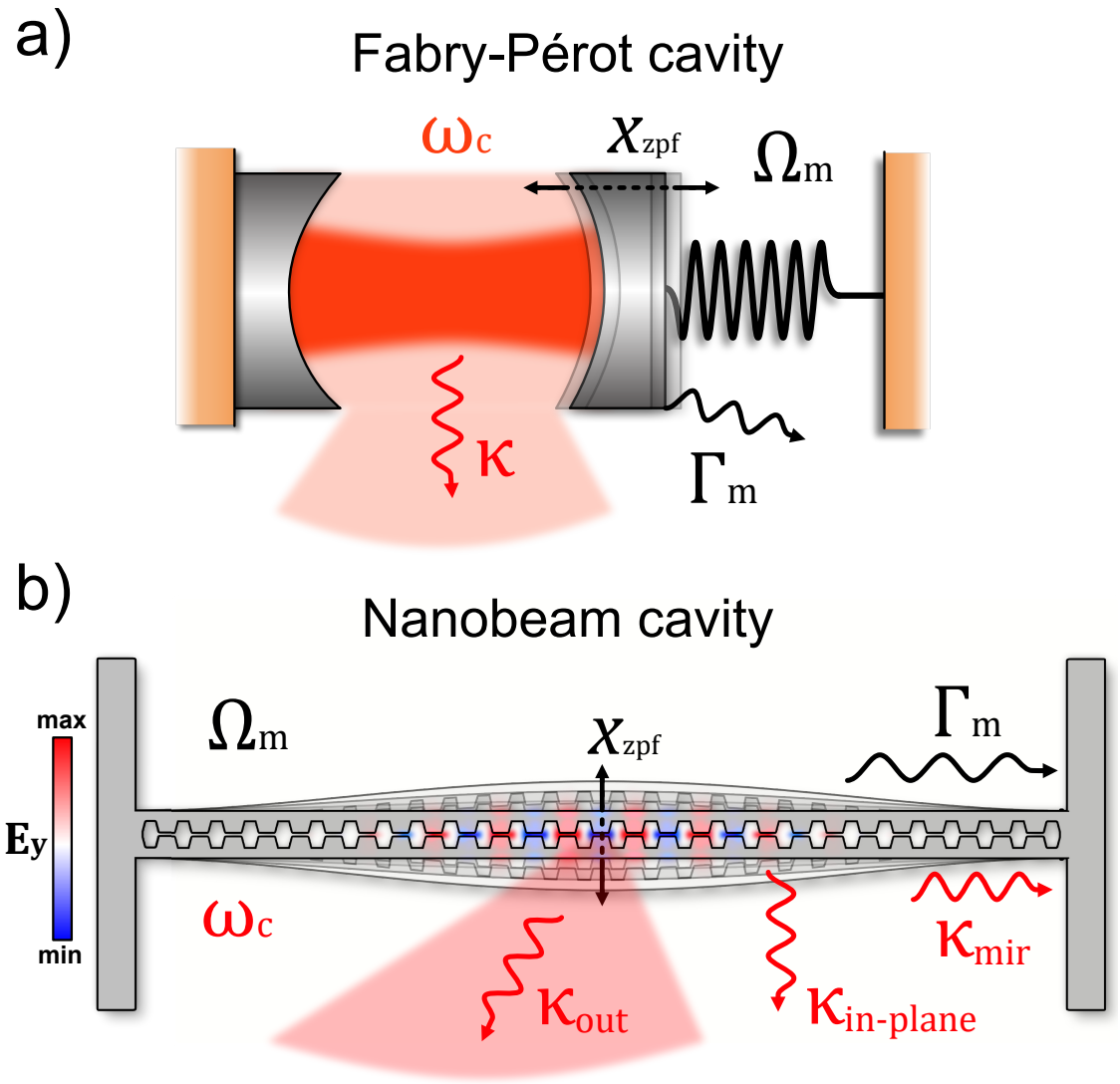

Figure 4. **a)** An optomechanical Fabry-Pérot cavity with its mechanical and optical frequencies Ω_m,ω_c, loss rates Γ_m, κ and displacement x_{zpf}. **b)** An optomechanical nanobeam cavity with its equivalent properties. The amplitude of the E-fields vertical component is shown as $\mathbf{E_y}$. The mechanical oscillations decay by escaping into the surrounding silicon. The optical pathways of decay are separated into losses through the mirrors κ_{mir}, in-plane losses $\kappa_{in\text{-}plane}$ and out-of-plane losses κ_{out}. Optimizing the cavity consists of minimizing the mirror and in-plane losses, while maximizing the out-of-plane detection $\eta\kappa_{out}$, where η is the detection efficiency.

which corresponds to a wave function

$$\mathbf{E} = E_0 e^{-\kappa t} e^{i(\mathbf{k}\cdot\mathbf{x}-\omega_0 t)}, \tag{58}$$

where the wave amplitude E_0 inside the cavity attenuates exponentially with time $e^{-\kappa t}$ similarly to the mechanical damping. As with the mechanical resonators, the decay rate κ is meaningful only in the context of the resonance frequency. Therefore, a similar scale-invariant measure called the optical quality factor

$$Q = \frac{\omega_0}{\kappa}, \tag{59}$$

is commonly used to compare the performance of cavities with different frequencies. Consequently, a high quality factor is a trait of a well performing cavity. The optical decay rate κ and quality factor Q are analogous to the damping rate Γ_m and quality factor Q_m of a mechanical resonator. In the case of multiple uncorrelated pathways of decay, the total decay rate can be divided into a sum of its constituents

$$\kappa = \kappa_0 + \kappa_1 + \dots , \tag{60}$$

corresponding to the Q-factors

$$\frac{1}{Q} = \frac{1}{Q_0} + \frac{1}{Q_1} + \dots . \tag{61}$$

These properties are of high utility when trying to identify the different sources that might affect the cavity decay. Importantly, the total Q-factor can only be as large as the lowest constituent Q, and is thus limited by the largest decay pathway.

Increasing the cavity Q-factor is one of the main steps in the optimization of the nanobeam. We don't necessarily need the Q-factor to be too high, as we want to be able to detect light leaving the cavity. However, it is reasonable to first design for a high-Q cavity, and only then try to control the direction of outgoing losses.

2.3.2 Coupling light to displacement

An optomechanical cavity can be constructed from Fabry-Pérot cavity by simply allowing one of the mirrors to move mechanically e.g. on a spring. In such a cavity, the resonant frequency ω_c can be altered by shifts in the suspended mirror. For an optical cavity, the Hamiltonian is analogous to that of the mechanical resonator

$$\mathcal{H}_{\mathrm{c}}/\hbar = \omega_{\mathrm{c}} \left(\frac{1}{2} + a^{\dagger} a \right), \tag{62}$$

where $\hat{a}^{\dagger}\hat{a} = n_c$ is now the total number of photons in the cavity, with the photon creation $\hat{a}^{\dagger}$ and annihilation $\hat{a}$ operators. Combining equation (23) and (62) into an optomechanical Hamiltonian, gives

$$\mathcal{H}/\hbar = \Omega_{\mathrm{m}} \hat{b}^{\dagger}\hat{b} + \omega_{\mathrm{c}} \hat{a}^{\dagger}\hat{a}, \tag{63}$$

where we ignored the zero-point energy terms. As with the mechanical resonator, we estimate the optical frequency shift induced by the displacement of the nanobeam with first-order Taylor expansion

$$\omega_{\mathrm{c}}(x) \approx \omega_0 + \hat{x} \frac{\partial \omega}{\partial x} + \mathrm{O}(x^2), \tag{64}$$

where terms of the order of $\mathrm{O}(x^2)$ or higher will again be neglected. The Hamiltonian (63) then becomes

$$\mathcal{H}/\hbar = \Omega_{\mathrm{m}} \hat{b}^{\dagger}\hat{b} + \omega_0 \hat{a}^{\dagger}\hat{a} + \hat{x} \frac{\partial \omega_{\mathrm{c}}}{\partial x} \hat{a}^{\dagger}\hat{a} \tag{65}$$

Expressing the position operator in terms of zero-point fluctuations $\hat{x} \equiv x_{\mathrm{zpf}}(\hat{b}^{\dagger} + \hat{b})$ results in

$$\mathcal{H}/\hbar = \Omega_{\mathrm{m}} \hat{b}^{\dagger}\hat{b} + \omega_0 \hat{a}^{\dagger}\hat{a} + x_{\mathrm{zpf}} \frac{\partial \omega_{\mathrm{c}}}{\partial x} \hat{a}^{\dagger}\hat{a}(\hat{b}^{\dagger} + \hat{b}) \tag{66}$$

Now we can define the optomechanical coupling strength as

$$g_0 \equiv x_{\mathrm{zpf}} \frac{\partial \omega_{\mathrm{c}}}{\partial x}, \tag{67}$$

which describes how much a displacement in the nanobeam affects the cavity frequency. It turns out that we do not need to go further than this analytically. The effect of a small displacement on the cavity frequency of the beam can be attained directly by displacing the nanobeam in simulations e.g. by increasing the gap be-

tween the nanobeam halves. We conclude that the optomechanical coupling can be approximated with

$$g_0 = x_{\mathrm{zpf}} \frac{\delta\omega_c}{\delta x}, \tag{68}$$

where $\delta\omega_c$ is the cavity frequency shift caused by a displacement δx of the nanobeam half.

2.4 High-Q photonic crystal cavities

High Q-factor photonic cavities are essential for optical measurements, as they enable us to enhance effects at nanoscale with high EM-fields. In the following sections we introduce photonic crystals and the requirements for creating a high-Q cavity. We follow design ideas from [42–44]. For a good overview on photonic crystals, see [32].

2.4.1 Photonic crystals

How can we build reflective mirrors for an optical cavity at nanoscales? How can we tune the cavity resonance for selected frequencies? These questions are answered by photonic crystal cavity design.

Photonic crystals (PhC) are periodically patterned dielectric structures, that enable the control of light. The dielectric patterning creates a photonic band structure, similar to that of the electronic band structure in crystals (see Figure 5), and allows the transmittance of resonant EM frequencies while attenuating others. The transmitted and attenuated frequency modes are dependent on the geometry of the crystal, as well as the dielectric constants ϵ and refractive indexes $n \simeq \sqrt{\epsilon}$ of the materials. Therefore, a photonic crystal structure can be geometrically designed to trap light of selected frequencies.

The cavity of the nanobeam is built as a combination of two photonic crystal structures: a silicon waveguide and a Bragg mirror. The silicon beam forms a waveguide, which constrains light to move along its direction. The Bragg mirror is periodical layering of two dielectric mediums. The dielectric mediums for our nanobeam are silicon with $n_{\mathrm{Si}} \simeq 3.47$ and etched holes for air or vacuum with $n_{\mathrm{air}} \simeq 1$. Figure 5 shows how the perforated Bragg mirror structure of the nanobeam creates photonic bands in the first Brillouin zone (BZ) of an ideal infinite nanobeam.

It should be noted that the photonic bands corresponding to resonant EM-field modes in the nanobeam are not typical vacuum modes with both electric and magnetic fields being transverse (TEM modes) to the direction of propagation. Instead, the PhC nanobeam confines light in polarized transverse electric (TE) and transverse magnetic (TM) modes, where the field lines of the transverse component form a loop transverse to the direction of propagation. Importantly, we are interested in the fundamental TE_1 mode in Figure 5 as it creates high electric field and radiation pressure between the nanobeam's teeth. The idea is to create a PhC cavity by

matching the TE_1 band frequency at the BZ edge $k = \pi/a$ with our laboratory laser frequency and geometrically tune the bandgap in Figure 5 to create confinement.

2.4.2 Mirror strength and the photonic bandgap

In order to confine the light in the cavity, mirrors have to be designed at the ends of the nanobeam. The mirrors can be constructed by shifting the TE_1 mode frequency away from the cavity frequency at the ends of the nanobeam. This is achieved by changing the silicon-to-air ratio and hole geometry in the beam.

To maximize reflection, we would like to minimize the spatial distribution of electric field outside the cavity, so that it does not leak to free space from the nanobeam ends. The spatial attenuation profile of the EM-field can be approximated similar to the temporal attenuation in equation (57) by an imaginary wavevector component

$$k = k_0 + i\gamma, \tag{69}$$

which corresponds to a electric field profile

$$\mathbf{E} = E_0 e^{-\gamma x} e^{i(kx - \omega_n t)}, \tag{70}$$

where γ is the mirror strength describing the exponential decay of the field amplitude $e^{-\gamma x}$ within the mirrors. A higher γ is then better for light confinement. In order to understand the relationship between the mirror strength γ and the photonic band structure, we can approximate the effect of a small shift of $\delta k = k - \pi/a$ on the ν_1 frequency at the BZ edge [32, p.52]. Due to the time reversal symmetry of the photonic bands at the BZ edge $k = \pi/a$, we can ignore the asymmetric Taylor expansion terms, which leaves

$$\nu_1(\delta k) \approx \nu_1\left(\frac{\pi}{a}\right) + \frac{\partial^2 \nu_1\left(\frac{\pi}{a}\right)}{\partial k^2}\delta k^2 + \mathrm{O}(\delta k^4). \tag{71}$$

We mark the curvature of the approximated band as $-\alpha = \partial^2 \nu_1\left(\frac{\pi}{a}\right)/\partial k^2$ which leads to a frequency shift

$$\delta\nu_1 \approx -\alpha \delta k^2 \tag{72}$$

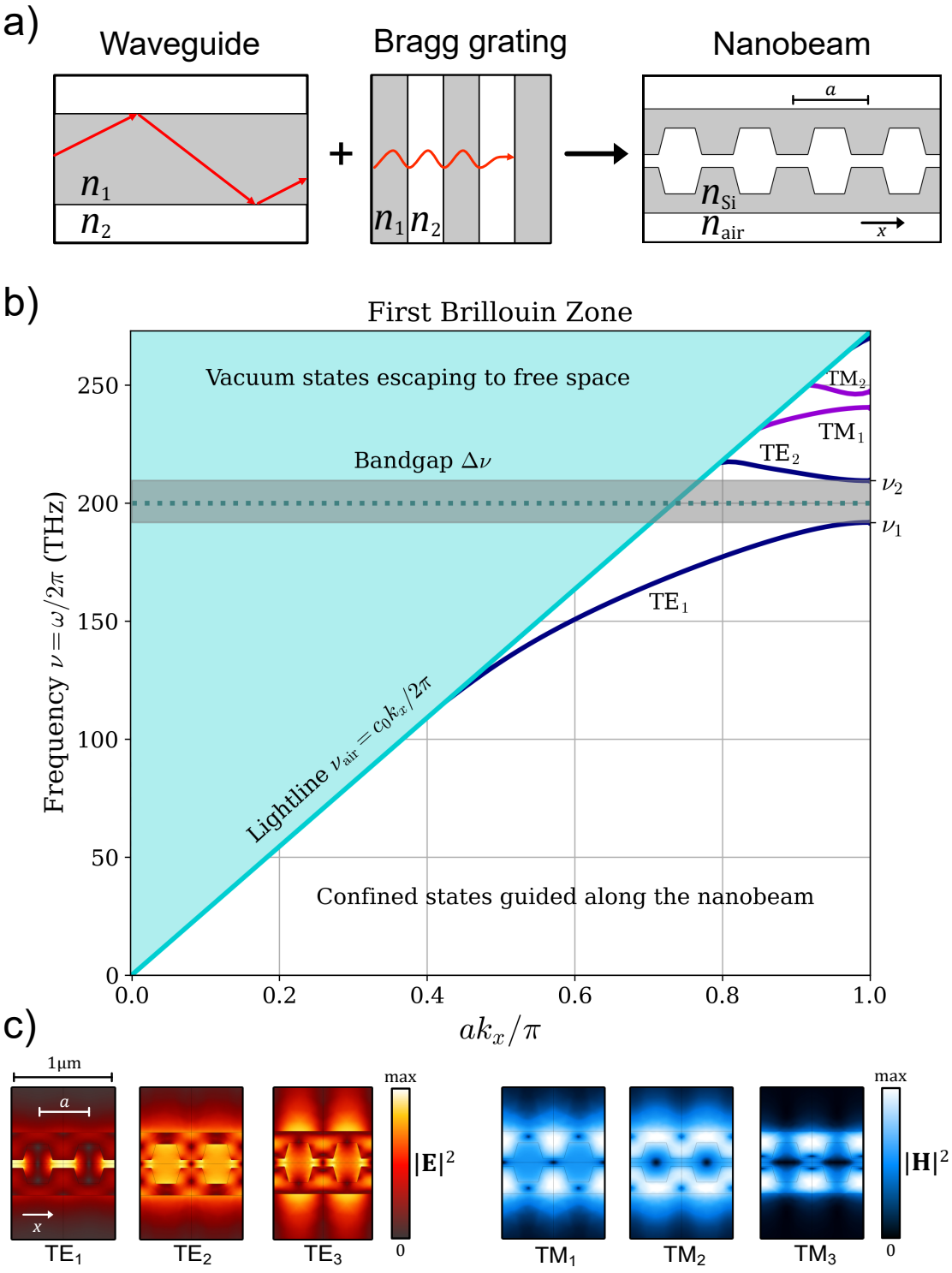

Figure 5. **a)** The sliced photonic crystal nanobeam as a Bragg grated slot waveguide with periodicity a to the wave propagation direction x. **b)** Photonic band structure for wavevector k_x in the first Brilluoin zone of the nanobeam. The states above the lightline ν_{air} with the speed of light c_0 are able to escape to free space, whereas the bands of resonant mode below are confined in the nanobeam. The bandgap $\Delta\nu$ marks a region where no waves propagate in the nanobeam. **c)** The EM-field energy densities for TE and TM modes. The fundamental TE$_1$ mode is the most optomechanically active mode due to a high E-field concentrated between the nanobeam's teeth.

and the corresponding wavenumber shift

$$\delta k \approx \sqrt{-\frac{\delta\nu_1}{\alpha}}. \tag{73}$$

Here, we can notice that for frequency shifts $\delta\nu_1 < 0$ towards the TE_1 band, the values for δk are real and correspond to the band frequencies. However, if we shift the frequency into the bandgap $\delta\nu_1 > 0$, the δk values are imaginary. The imaginary shift in wavenumber $k = k_0 + \delta k$ corresponds to equation (69) and the mirrors strength is revealed as

$$i\gamma = \delta k \propto i\sqrt{\delta\nu}, \tag{74}$$

which means that the exponential attenuation increases with $\sqrt{\delta\nu}$ the further we go into the bandgap. Importantly, the approximation (72) can be done for both frequencies ν_1 and ν_2, which means that the mirror strength depends on the **frequency distance from both bands**

$$\gamma \propto \left(\sqrt{\delta\nu_1} + \sqrt{\Delta\nu - \delta\nu_1}\right), \tag{75}$$

where the shift from TE_2 frequency is $\delta\nu_2 = \Delta\nu - \delta\nu_1$ and $\Delta\nu = \nu_2 - \nu_1$ is bandgap between ν_1 and ν_2. Therefore, the mirror strength reaches its maximum at the center of the bandgap ν_{mid} (dotted line in Figure 5), where the frequency is furthest from both photonic bands with real values of $\nu_{1,2}$. Moreover, with increasing size of the bandgap $\Delta\nu$, the mirror strength also increases. For the mirrors a large bandgap with center frequency matching the ν_1 of the cavity is needed to optimize cavity Q-factor.

2.4.3 Gaussian attenuation profile

When trying to increase the Q-factor of a photonic cavity, the out-of-plane scattering (with $Q_{\text{out}}, \kappa_{\text{out}}$) to free space is known to be a limiting factor [42]. The out-of-plane scattering power P_{out} has been shown to be proportional to the Fourier components of the EM-fields overlapping with vacuum states

$$P_{\text{out}} \;\propto\; \int_{<\text{lightline}} \mathrm{d}k(|\mathcal{F}[H_z]|^2 \,+\, |\mathcal{F}[E_z]|^2), \tag{76}$$

where $\mathcal{F}[H_z]$ and $\mathcal{F}[E_z]$ mark the spatial Fourier transformation. Figure 6 shows the E-field distributions for nanobeams with tapered and constant mirrors. For mirrors with constant mirror strength γ, the EM-field attenuates exponentially with $e^{-\gamma x}$ as seen in (70). Fourier transforming the exponential attenuation profile creates a Lorentzian distribution for our resonant frequency at the first BZ edge

$$\mathcal{F}_x\left[e^{-\gamma|x|}\right](k) = \sqrt{\frac{2}{\pi}}\frac{\gamma}{k^2+\gamma^2} \propto k^{-2}, \tag{77}$$

where part of the distribution that overlaps with the vacuum states above the lightline are able to scatter. Ideally, the overlapping field would be minimized by tightly localizing the Fourier distribution in k-space.

Fortunately, the classical Fourier uncertainty with the variance relation $\sigma_k^2\sigma_x^2 \geq \frac{1}{4}$ is known to be minimized by a Gaussian distribution. Thus, we want to create a Gaussian attenuation profile by linearly increasing the mirror strength with distance from the cavity center $\gamma \to \eta|x|$, so that $e^{-\gamma|x|} \to e^{-\eta x^2}$ and $\max(\eta|x|) = \gamma$. The Fourier transform of a Gaussian attenuation profile is also a Gaussian distribution in k-space

$$\mathcal{F}_x\left[e^{-\eta x^2}\right](k) = \frac{1}{\sqrt{2\eta}}e^{-k^2/4\eta} \propto e^{-k^2}. \tag{78}$$

Clearly, a distribution following e^{-k^2} can offer more confinement than k^{-2}. Practically, the Gaussian attenuation profile means that the mirror geometry has to be tapered so that the mirror strength is linearly increasing away from the cavity. This is achieved by changing the geometry at the nanobeam ends so that resonance frequency ν_1 decreases linearly away from the cavity.

2.4.4 Airgap: the distance to lightline

Additionally, the overlap P_{out} between the E-field distribution and free space states in Figure 6 is affected by the distance of the lightline $k_{\text{air}} = 2\pi\nu_{\text{air}}/c_0$ from the BZ edge $k = \pi/a$ for a resonant frequency. Therefore, scattering radiation is minimized by a short periodicity a and a small k_{air}. Since $k_{\text{air}} \propto \nu_{\text{air}}$, the scattering is lesser for lower frequencies. In Figure 5, this corresponds to the pushing down of the TE_1 band frequency ν_1. For simulations, the distance from lightline can be measured as the airgap at the BZ edge

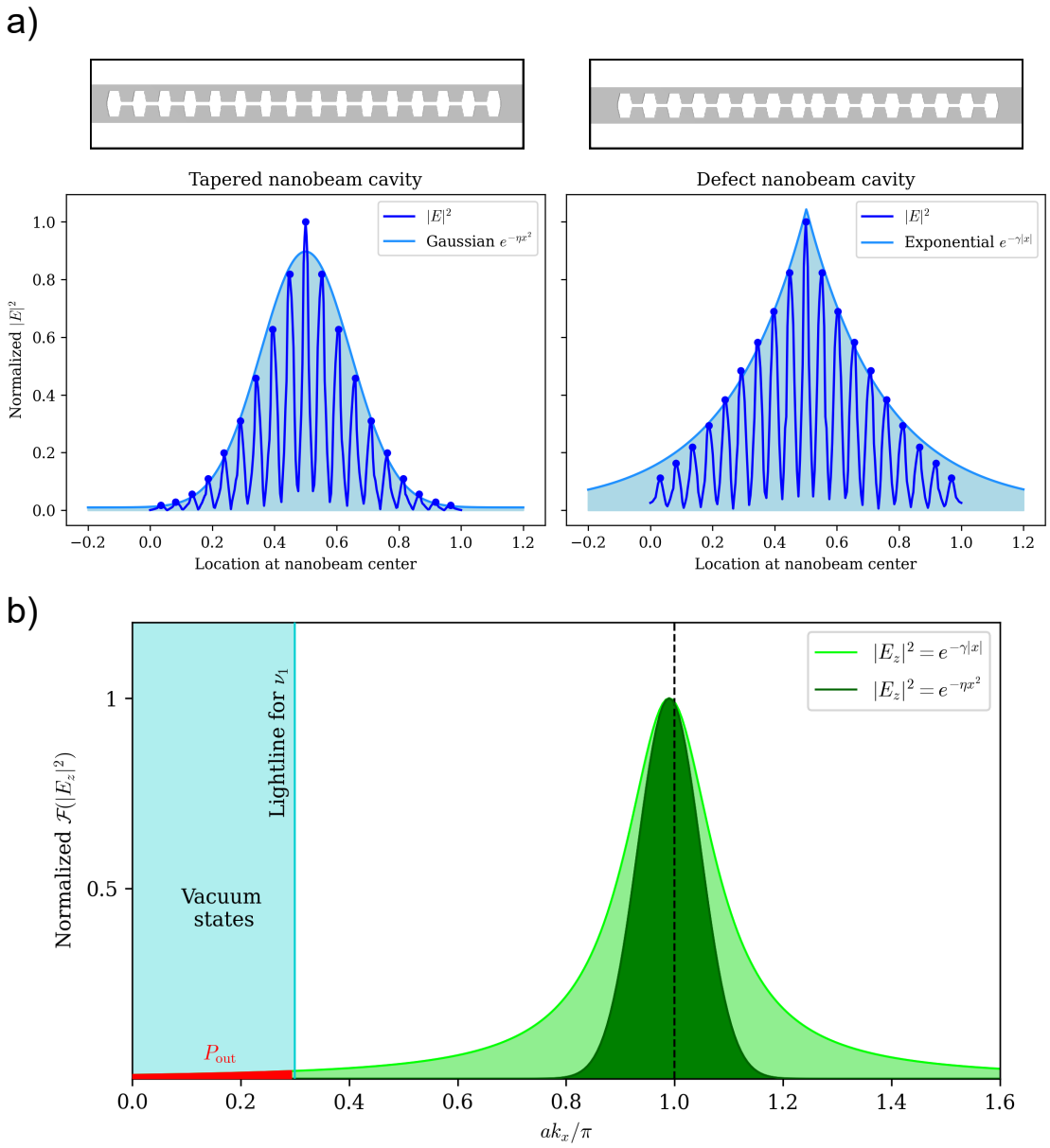

Figure 6. a) Normalized E-fields of a TE_1 mode in the nanobeam for constant and linearly increasing mirror strengths with a Gaussian and exponential attenuation profile. Illustrative nanobeams are shown above. **b)** Fourier transformations of the field profiles depicting the intensity in k-space. The Gaussian distribution has less overlap with the vacuum states for the frequency ν_1, and thus has less out-of-plane scattering.

$$\Delta\nu_{\text{air}} = \nu_{\text{air}}\left(\frac{\pi}{a}\right) - \nu_1\left(\frac{\pi}{a}\right), \tag{79}$$

which we want to maximize to achieve highest confinement of light to the nanobeam. Intuitively, the airgap is affected by the amounts of silicon in the nanobeam shifting the resonant frequencies down and the minimum resonant wavelength in the periodic structure.

2.4.5 Phase matching

In Figure 6 a), we can see that the that the normalized E-field follows an attenuating sine function $|\sin(\pi x/a)|^2$ inside nanobeam, where the peaks are located in between the teeths with periodicity a. Thus, the periodicity affects the phase of the resonant mode. In order to match the phase of the EM-field mode in each periodic cell, the periodicity should be kept constant between cells. Otherwise, the mode mismatch at the interface between two periodic cells will increase scattering [42]. Correspondingly in the reciprocal k-space, altering the periodicity a changes the location of the first BZ edge $k_x = \pi/a$, which leads to a less confined E-field distribution. Therefore, we will refrain from using the periodicity a for the tapering of the nanobeam.

2.4.6 Mode volume

To compare the confinement of the EM-fields between PhC cavities of different shapes and sizes, a quantity called modal volume V is used [32, p.150]. The modal volume is described as the ratio between total E-field near the cavity volume and the peak maximum of the E-field

$$V = \frac{\int dr^3 \epsilon |\mathbf{E}|^{\mathbf{2}}}{\max(\epsilon |\mathbf{E}|^{\mathbf{2}})}. \tag{80}$$

For comparison, the modal volume is usually normalized with the smallest volume a (half) wavelength $\lambda/2$ of light can be confined in a material i.e. silicon with a refractive index n_{Si}, given by

$$V_{\text{norm}} = \frac{V}{(\lambda/2n_{\text{Si}})^3}. \tag{81}$$

Increasing the spatial mode volume can sometimes allow for a more confined

distribution of the Fourier transformed field in Figure 6 b) increasing the Q-factor by sacrificing spatial localization of the EM-fields.

2.4.7 Double period modulation

In order to maximize the out-coupling of the light escaping our nanobeam cavity, we need a way to control its scattering direction. A method known as the double period modulation (DPM) [44] uses the symmetry of the first Brillouin zone to calibrate the scattering direction from in-plane (x,y) to out-of-plane (z) direction, as shown in Figure 7.

DPM applies a size modulation on every other periodic cell, so that the resulting structure has double the periodicity. The change in hole size hinders the wave propagation to x-direction of the resonant mode with the unmodulated periodicity a. In the first BZ, this causes the intensity distribution at $k = \pi/a$ to be mirrored with respect to the BZ edge of the modulated periodicity at $k_x = \pi/2a$ to $k_x = 0$. At $k_x = 0$ the mode does not propagate to x-direction, but instead scatter to y,z-directions. In 2D materials the scattering can be better confined to only z-direction, but in a 1D periodic nanobeam, the y-directional scattering cannot be controlled. In our nanobeam waveguide, the y-directional scattering is restricted by the internal reflection of the silicon.

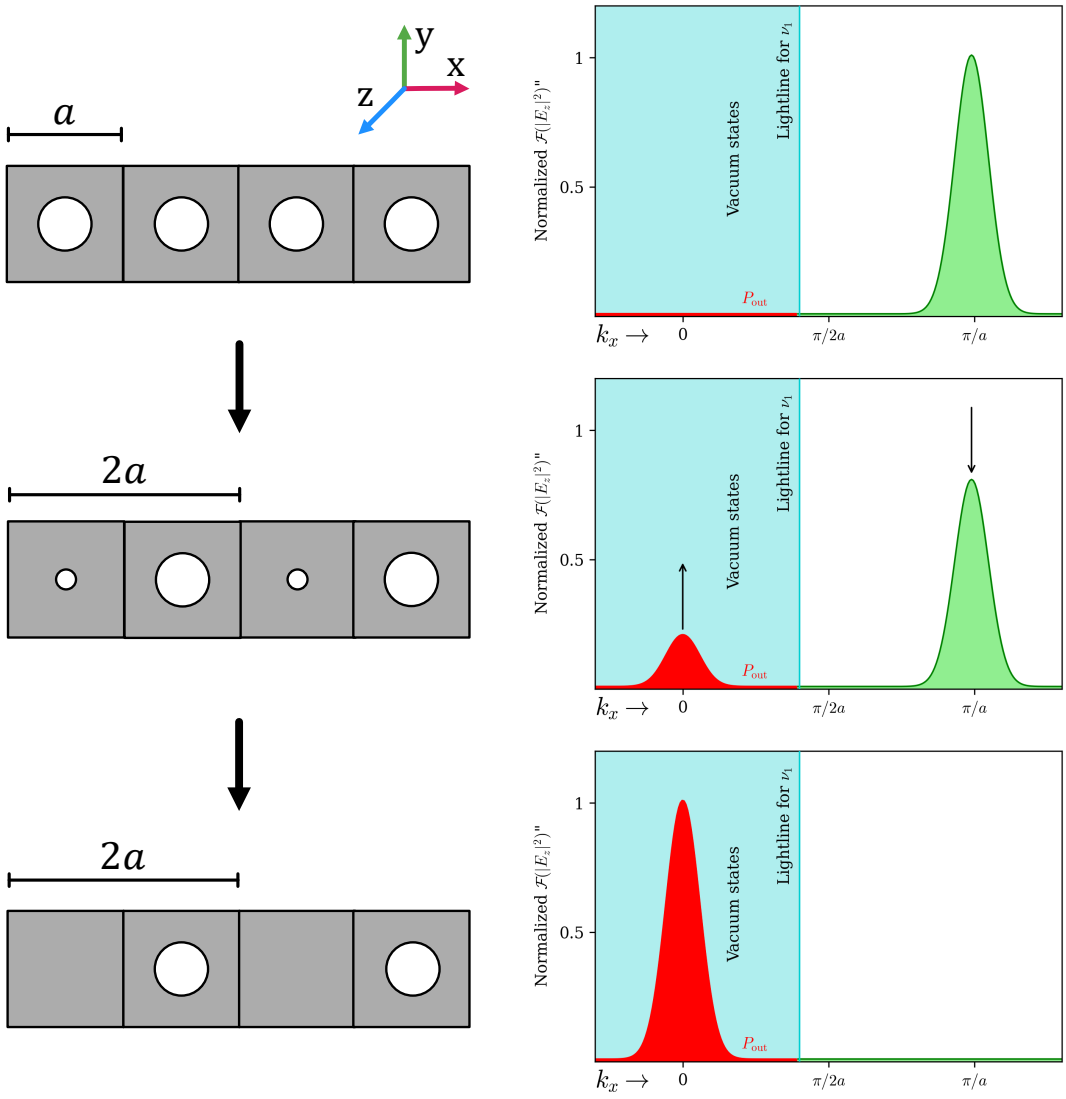

Figure 7. a) Illustration of double period modulation of holes in a nanobeam. Changing the size of every other hole doubles the periodicity of the structure. **b)** The corresponding E-field distributions. Initially, the E-field is confined to $k_x = \pi/a$ for the ν_1 resonant mode. As the size of every other hole is modulated, the distribution is mirrored to $k_x = 0$ as new BZ edge is formed at $k_x = \pi/2a$. The resulting wavevector will be of the form $\mathbf{k} = (0,k_y,k_z)$. If the modulation is taken to extreme with only half of the holes present, the structure with does not support the propagation of the original mode. In this case, almost all of the E-field is scattered to y and z-directions.

3 Numerical simulations

Our goals for the design of the nanobeam are the following:

1. To maxmimize the optomechanical g_0 and spin-mechanical λ_0 couplings
2. To create a high-Q cavity and control the output scattering direction.

We try to achieve these goals in the context of our research groups laboratory equipment and fabrication possibilities. Our research group uses two subinfrared lasers with frequency ranges 1460–1570 nm and 1510–1630 nm corresponding to a total frequency range 183–205 THz. The frequency range is compatable with the fiber-optic transmission window around 200 THz, which minimizes the fiber attenuation in the current communication infrastructure. We will choose the center frequency $\nu_c \coloneqq 194\,\mathrm{THz}$ of our laser range as the sweet spot for the optical cavity frequency.

The real devices are fabricated onto a silicon-on-insulator (SOI) chip using electron-beam litography and etching. For our group, the smallest robustly reproducible slit hole width by etching is currently $\geq 80\,\mathrm{nm}$, and the thinnest beam of silicon able to support the nanobeam has been $\geq 120\,\mathrm{nm}$. This provides limitations to the design geometry. The fabrication procedure itself is described in more detail in [27, p.25] and [25, p.70]. We also base our simulations on previous works [25, 26].

The design process utilizes the FEM eigenfrequency solver of COMSOL Multiphysics software to search for the resonant optical (Radio Frequency Module) and mechanical (Structural Mechanics Module) frequencies of the nanobeam. The eigenfrequency solver calculates the determinant of a linear system with the multiple degrees of freedom of a finite mesh. The resonant frequencies of the mesh are then returned as an ordered list from lowest to highest with their real and imaginary components.

First, our aim is to optimize the band structure for the cavity and mirror using computationally efficient periodic unit cell simulations. The unit cell simulations depicted in Figure 8 take advantage of the symmetry and periodicity of the nanobeam using mirror symmetry and periodic boundary conditions (PBC) in COMSOL. Secondly, we create the nanobeam cavity simply by stacking the unit cells for mirrors

Table 3. Nanobeam unit cell parameters with their descriptions and estimated ranges for resonance frequencies around 200 THz. The parameters marked with red are kept constant based on previous work [26].

a	Periodic constant or unit cell length	400–800 nm
w	Nanobeam width	400–1500 nm
d	Hole length at the gap side of the beam,	$\%a$
f	Hole length at the far side of the beam,	$\%a$
support	Thinnest silicon width supporting the nanobeam	120 nm,
gap	Smallest gap between the nanobeam halves	80 nm,
thickness	Thickness of silicon layer to z-direction	220 nm

and cavity with an additional tapering region between them, as shown in Figure 9. The numbers of mirror and cavity cells in the nanobeam is then adjusted to match the highest Q-factor with full nanobeam simulations. Finally, we add a strain confining design outside the nanobeam cavity, shown in Figure 10. The optical simulations were done first, as the cavity structure limits for the size of the nanobeam resonator. The mechanical strain geometry is then adjusted outside the optical cavity.

3.1 Periodic unit cell

We begin the design of our nanobeam by geometrical parameterization. The nanobeam is constructed by stacking unit cells of varying dimensions as shown in Figure 8. A trapezoidal hole structure is used to gain more control over the design, while conserving fabrication simplicity. The parameters are described in table 3.

To simulate the PhC band structure of the nanobeam, we calculated the eigenmodes of the electromagnetic field in the nanobeam unit cell using PBC. This is equivalent to having an infinite nanobeam repeating the single unit cell geometry. We placed our unit cell in an 3D airbox to include the effects of the surrounding air. The size of the airbox was chosen as $a \times 1.5\,\mu\text{m} \times 1.5\,\mu\text{m}$ to minimize computation time while preserving the accuracy of resulting eigenfrequencies, as shown in [26, p.12]. A tetrahedral FEM mesh was used with sizes ~ 10 nm in the gap region and ~ 100 nm in the surrounding air and silicon.

At the airbox sides perpendicular to the nanobeam, we set a periodic boundary condition for our fields $\vec{E}\,(x+a) = e^{ik_x a}\vec{E}\,(x)$, where k_x is the wavevector number, resulting in Floquet-Bloch periodic wave solutions. The airbox facet at $z = 0$ was set as a perfect magnetic conductor to pick out only the TE-mode solutions.

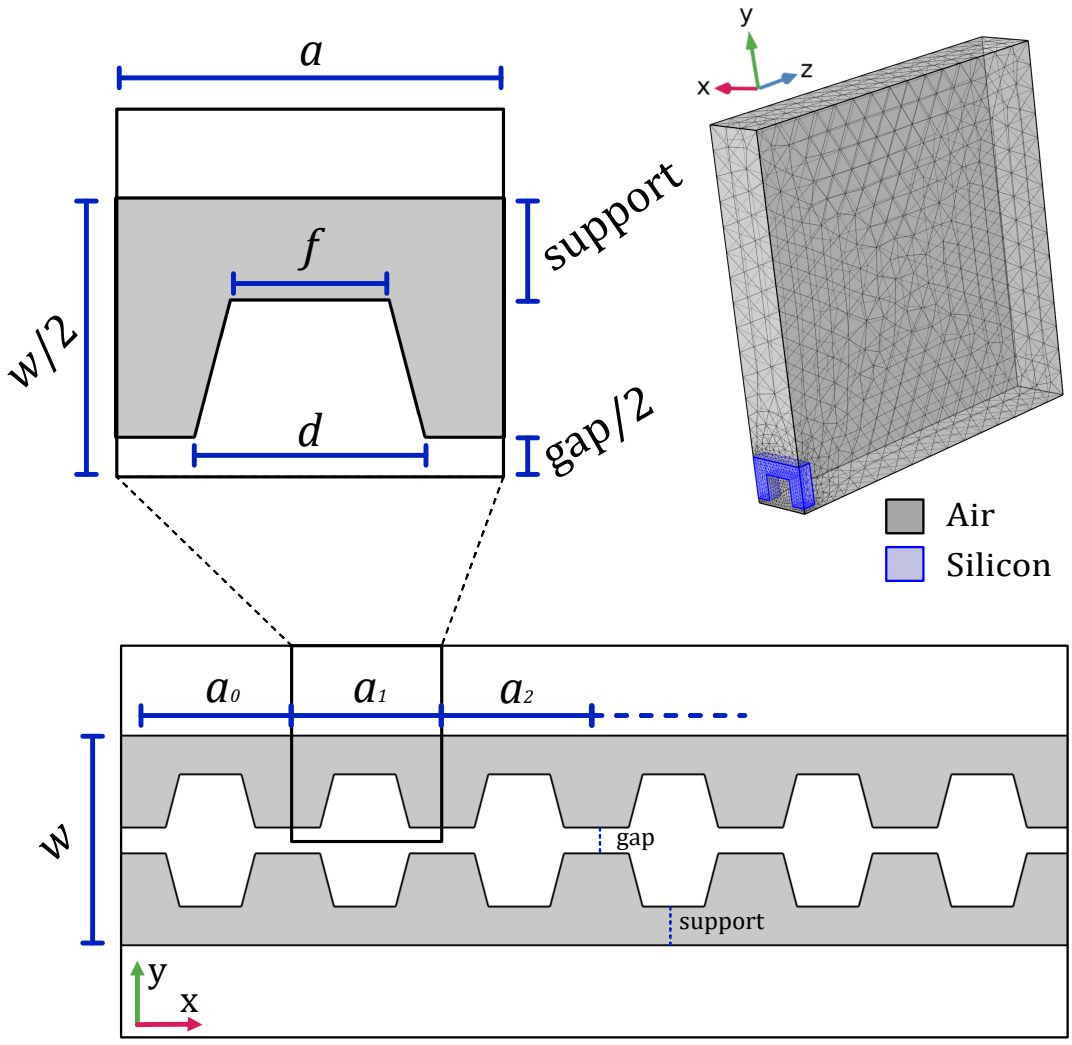

Figure 8. Parameterization of the nanobeam. The nanobeam is built by stacking unit cells with different varying parameters. The unit cell parameters can be optimized by performing eigenfrequency simulations in an 3D airbox with periodic boundary conditions in x-direction and mirror symmetry in y-direction.

Correspondingly, the TM-modes are found by setting the facet at $z = 0$ as a perfect electric conductor. The remaining sides were left as perfect electric conductors.

The photonic band diagram for the unit cell's first Brillouin zone can be calculated by sweeping for values of $k_x = 0 \to \frac{\pi}{a}$, as seen in Figure 5. The COMSOL eigenfrequency solver returns an ordered list of resonant frequencies from lowest to highest. The frequencies below the lightline $\nu_{\text{air}} = c_0 k_x / 2\pi$, where c_0 is the speed of light in vacuum, are meaningful as they are confined to the nanobeam, whereas the frequencies above the lightline are resonant in the surrounding airbox. The distance from the lightline $\Delta\nu_{\text{air}} = \nu_{\text{air}} - \nu_1$ describes the confinement of the TE_1 mode to the nanobeam.

The optomechanical coupling can be estimated by increasing the gap half by a small displacement $\delta x = 1\,\text{nm}$, and calculating the shift in the resonant frequency $\delta\nu_1$. We define a proxy for the optomechanical coupling as

$$G \coloneqq \frac{\delta\nu_1}{\delta x}.$$

We also estimate the expected zero-point fluctuations $\widetilde{x}_{\text{zpf}}$ with a nanobeam of fixed length $L = 20\,\mu\text{m}$ and breathing mode frequency $\Omega_{\text{m}} = 3\,\text{MHz}$ at the upper limit. The number of unit cells in the nanobeam can then be calculated as $N_{\text{tot}} = L/a$, which leads to an effective mass of $m_{\text{eff}} = 0.398 m_{\text{total}} = 0.398 N_{\text{total}} m_{\text{cell}}$ where m_{cell} is the unit cell mass. With $\widetilde{x}_{\text{zpf}} = \sqrt{\hbar / 2 m_{\text{eff}} \Omega_{\text{m}}}$ the optomechanical coupling can be estimated as

$$g_0 = x_{\text{zpf}} \frac{\partial \nu_1}{\partial x} \propto \widetilde{x}_{\text{zpf}} G.$$

For the optimization procedure itself, we utilized COMSOL's parametric sweep method to plot the figures of merit $\nu_1, \nu_2, \Delta\nu, \Delta\nu_{\text{air}}, G, \widetilde{x}_{\text{zpf}}$ to identify the optimal unit cell geometries connected by a tapering line for linearly increasing mirror strength.

3.2 Nanobeam cavity

After choosing optimized geometries for the cavity and mirror unit cells, we built the full nanobeam cavity by stacking a number of cavity N_{cav} and mirror N_{mir} unit cells with an additional tapering region of N_{tap} tapered cells for the Gaussian attenuation profile. We created the tapering profile using a scaling factor $b^p : b \in [0,1]$ between the cavity cell width w_{cav} and mirror cell width w_{mir}

$$\mathbf{w}_{\text{tap}} = w_{\text{cav}} + \mathbf{b}^p |w_{\text{mir}} - w_{\text{cav}}|, \tag{82}$$

where $\mathbf{w}_{\text{tap}}$ is the list of tapered widths corresponding to scaling factors $\mathbf{b}^p$. The scaling power p mandates the tapering profile e.g. linear with $p = 1$ and quadratic with $p = 2$. Generally, the scaling in equation (82) can implemented on any parameter, except for periodicity a. For periodicity tapering, the locations for the unit cells have to be separately calculated, since they spacing is nonlinear. Since the mirror strength $\gamma \propto \sqrt{\delta\nu_1} + \sqrt{\Delta\nu - \delta\nu_1}$, the highest Q-factor is expected with quadratic tapering, when $\delta\nu_1$ increases linearly.

However, creating a custom tapered array of unit cells was possible in COMSOL only via tedious scripting. Thus, instead we used Python utilizing Nazca Design [45] and Klayout [46] packages for photonic integrated circuit (PIC) masks. This allowed the creation of 2D fabrication design using the same Python script. Using Nazca, a 2D model of the nanobeam could be exported as a .gds file. We then used Klayout to convert the .gds file to a .dxf file to be compatable with COMSOL. Finally, we imported the 2D .dxf model and extruded it into 3D with the silicon layer thickness in COMSOL. To avoid having to manually import and simulate each nanobeam geometry, we used a Python MPh [47] package to access the COMSOL Java application programming interface (API). This allowed us to simulate multiple geometries in one sweep, similar to the parametric sweeps available in COMSOL.

For the full nanobeam cavity simulations we added a cylindrical airtube around the nanobeam with spherical ends and extending support layer of silicon, as shown in Figure 9. For the mesh we kept the size similar to the unit cell airbox. We added an additional perfectly matched layer (PML) with a sweeped rectangular mesh at the airtube edge to better absorb the unwanted eigenfrequencies in the tube. To further reduce the computation time and unwanted eigenfrequencies, we reduced simulations to 1/8th of the airtube, and added perfect magnetic conductors to the

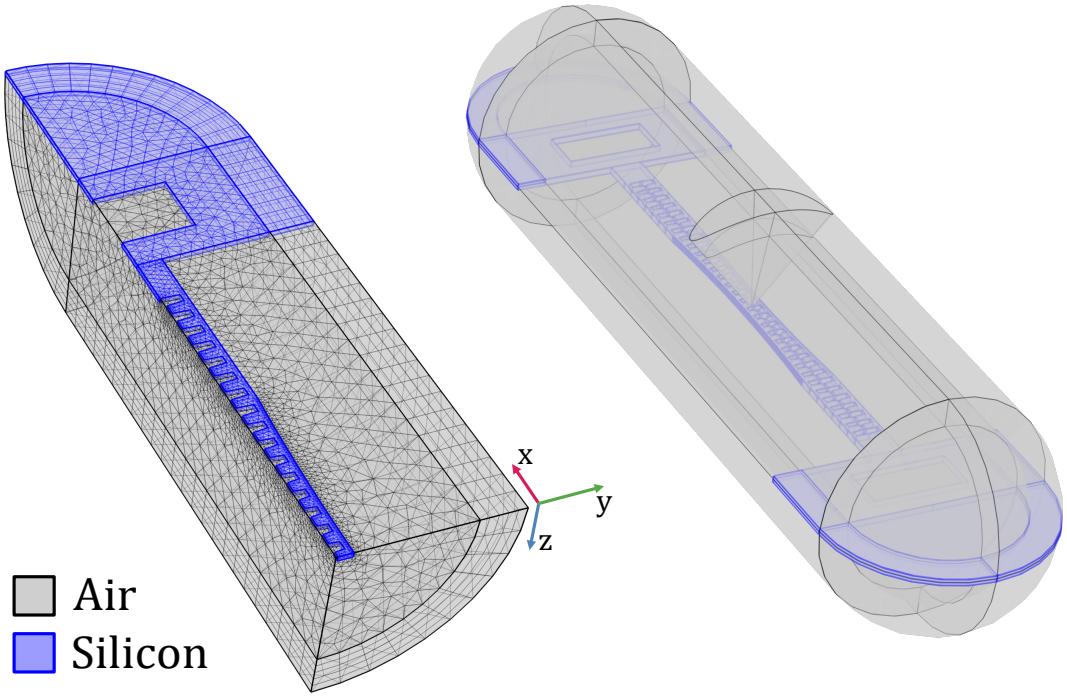

Figure 9. 3D models of the full nanobeam cavity. The full nanobeam cavity could be simulated in 1/8th of the airtube using symmetries. The reduction in computation time is twofold. First, the time solving a single eigenfrequency from the mesh is reduced. Second, the total number of unwanted resonances is smaller in 1/8th of the airtube. The air hole in the silicon layer next to the nanobeam is used to reduce fabrication induced stresses in the nanobeam [26]. The elliptical NA at the center of the nanobeam airtube is used to calculate the average ratio η_{avg}.

boundaries at $x = 0$ and $z = 0$ to find the proper resonant modes. For the estimation of optomechanical coupling, we simply extended the boundary at $y = 0$ by 1 nm and calculated the shift in the resonance frequencies.

For parametric sweeping, we solved the problem of mode selection i.e. finding and tracking correct optical modes in the nanobeam by constraining the eigenfrequency range and using the highest Q-factor of the fundamental TE_1 mode centered at the cavity. Fortunately, the resonant mode frequencies and their order did not change, although lengthening the cavity introduced more resonances of the TE_1 mode. Thus, we could identify them at by their frequency and Q-factors.

3.2.1 Far-field

Far-field calculations at a surrounding surface boundary estimate the direction and intensity of scattering EM-waves. COMSOL calculates electric far-fields using the 3D Stratton-Chu [48] formula

$$\mathbf{E}_{\text{far}} = \frac{ik}{4\pi}\mathbf{r_0} \times \int \left((\mathbf{n} \times \mathbf{E}) - \sqrt{\frac{\mu_0}{\epsilon_0}}\mathbf{r_0} \times (\mathbf{n} \times \mathbf{B}) \right) \exp\left(jk\mathbf{r} \cdot \mathbf{r}_0\right) dS, \tag{83}$$

over a surface S, where μ_0 and ϵ_0 are the vacuum permeability and permittivity, $\mathbf{n}$ is the normal vector and $\mathbf{r}$ ($\mathbf{r_0}$) is the radius (unit) vector pointing from the origin (center of the nanobeam) to a field point on the surface. In the case where the surface is a sphere at origin, $\mathbf{r}$ is the unit normal to the surface. We selected the surface below our airtube PML to estimate the far-fields at a distance of 2 μm from the nanobeam. Since COMSOL returns a Mercator projection of the 2D far-field surface in polar (spherical) coordinates, we addionally rotated the nanobeam 90° to face x-direction to avoid distortions.

We partitioned an ellipsoidal numerical aperture (NA) from the surface centered at x-direction with polar angle range of $\theta = 20°$ and azimuth angle range $\phi = 80°$ (see the elliptical cone inside the airtube in Figure 9). This was based on the high far-field region formed with higher double period modulations. We used the ratio between the total average far-field $\bar{E}_{\text{far}}$ and the average far-field inside the NA $\bar{E}_{\text{far}}^{\text{NA}}$ to estimate an average field ratio

$$\eta_{\text{avg}} = \frac{\bar{E}_{\text{far}}^{\text{NA}}}{\bar{E}_{\text{far}}} \tag{84}$$

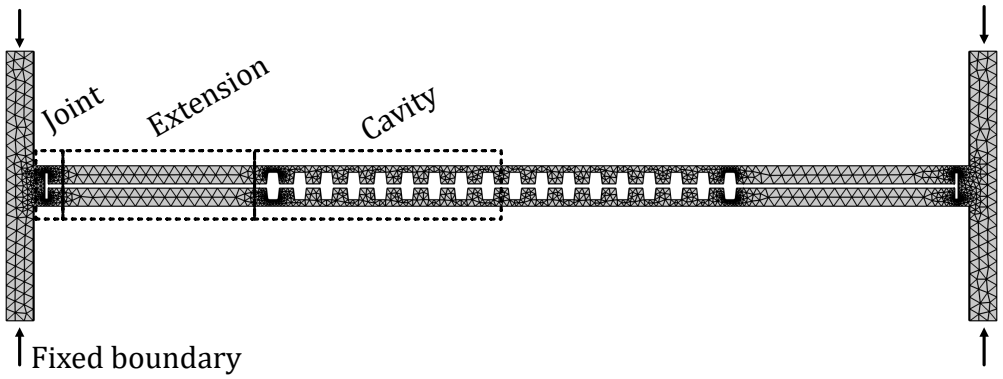

Figure 10. Meshed 3D model of the mechanically simulated nanobeam. The geometry of the cavity cell is used for the center cavity. The two supporting pillars are fixed from their ends. A higher resolution mesh is used at the areas of high strain. A strain confining design with uniform extension and a separate joint part is added to the nanobeam.

3.3 Mechanical nanobeam

The mechanical eigenfrequency simulations were done with a simplified version of the cavity, where the unit cell geometry was kept constant matching the cavity cell. This was enough for the relative comparison of the strains in the nanobeam, as the results with tapered nanobeam differed only slightly. With the simplified cavity, parametric sweeps for geometries could be done directly in COMSOL without the extra python scripting.

We constructed the 3D nanobeam from anisotropic silicon with additional supporting pillars fixed at the ends. We used the default orientation anisotropic silicon in COMSOL, where the x-direction along the nanobeam corresponds to the [110] direction of the crystal lattice in Miller's index notation [49]. A concave fillet of 40 nm radius was added to the sharp corners with high strain of the nanobeam joints to better resemble fabricated corners. We used a mesh size of ~ 10 nm for areas with high strain and ~ 100 nm for the rest of the nanobeam.

Similarly to the optical optimization, parametric sweeps were used to map out mechanical properties with the nanobeam dimensions. However, we searched for the more complex design of the nanobeam joint manually, as the COMSOL's optimization package was unavailable.

We observed that the nanobeam's geometry changed the order between the mechanical modes for the resonances in x,y, and z-directions, as well as between

their parallel and anti-parallel versions. We managed to select the fundamental y-directional breathing mode by setting a prescribed displacement of x,$z = 0$ on a point at the nanobeam's center. Furthermore, the problem of tracking parallel and anti-parallel mode could be evaded by simulating only one nanobeam half.

Importantly, the eigenfrequency solutions returned by COMSOL had an arbitrary unit of displacement and strain. Thus, we normalized the solutions using the ratio $E_{\mathrm{COMSOL}}/E_{\mathrm{zpf}}$ of the maximum potential energy in the displaced nanobeam E_{COMSOL} and the zero-point energy of a harmonic oscillator $E_{\mathrm{zpf}} = \frac{1}{2}\hbar\Omega_{\mathrm{m}}$. In order to keep the results consistent, we used the normalization E_{zpf} for results of a single nanobeam half and $2E_{\mathrm{zpf}}$ for results with both nanobeam halves, since the displacement potential energy doubled with the addition of the second nanobeam half. We used the normalization to deduce the zero-point properties relative to energy $\varepsilon_{xx}, x_{\mathrm{zpf}} \propto \sqrt{E}$.

4 Results

4.1 Mirror and cavity unit cells

For the mirror and cavity unit cells, priorities are to

- Cavity: Match $\nu_1 \approx 194\,\mathrm{THz}$ and maximize coupling G,
- Mirror: Match $\nu_{\mathrm{mid}} \approx 194\,\mathrm{THz}$ and maximize the first bandgap $\Delta\nu$,

while maximizing the displacement $\widetilde{x}_{\mathrm{zpf}}$ and the distance to lightline $\Delta\nu_{\mathrm{air}}$ for both. We can use parametric sweeps to explore the behaviour of the lowest photonic bands ν_1, ν_2 and the optical coupling G. We start by exploring these figures of merit using parametric sweeps in Figures 11 to 15.

Figure 11 starts with single parameter sweeps for each unit cell parameter, where we plotted changes in TE band structure and coupling. Notably, the behavior of support and gap widths verifies that they should be kept fixed at minimum size. Keeping the support width small is essential to the bandgap, and the coupling is highest at small gap widths. We can also see that the hole length f affects the bandgap more than d. Increasing periodicity a or beam width w drags down ν_1 but with the cost of lowering coupling.

Figure 12 depicts the general behavior of the figures of merit as a function of both a and w with holes and teeth of equal length. The coupling is highest at small a and w, whereas the bandgap maximizes with higher w. Most importantly, the bandgap $\Delta\nu$ and coupling G cannot be simultaneously optimized. Since maximizing the coupling G in the cavity is of high priority, the periodicity should be chosen around $a = (550 \pm 50)\mathrm{nm}$. This choice allows a to be kept constant as the tapering can be done directly upwards by increasing w from the cavity line to the mirror line in Figure 12.

In Figure 13, we can see the behavior of figures of merit as a function of hole lengths d and f. The hole size increases the first band frequency ν_1 slightly,but has much more impact on the the bandgap $\Delta\nu$. We can also see the much larger effect

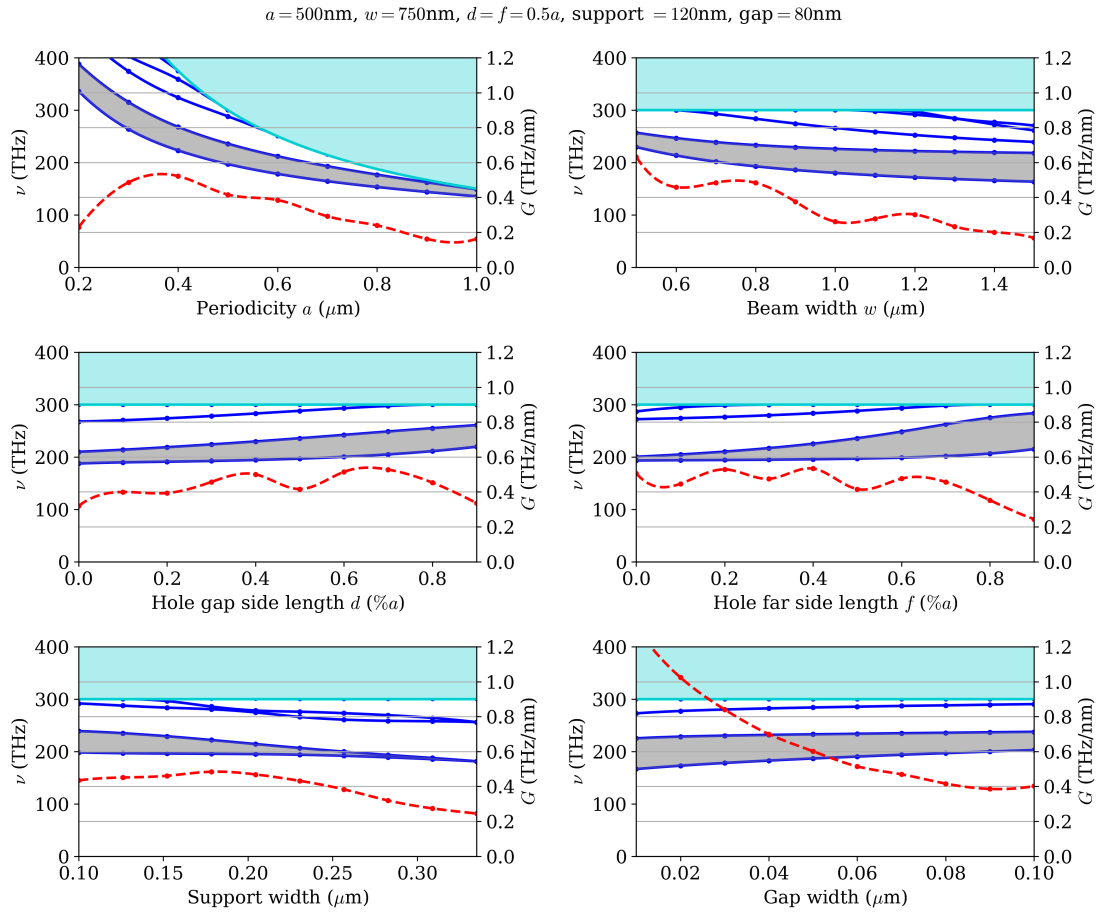

Figure 11. Optical eigenfrequency sweeps (blue dots with solid line) for each nanobeam parameter with lightline ν_{air} (turquoise), first bandgap $\Delta\nu$ (grey) and coupling G (red dots with dashed line). The lines correspond to cubic spline interpolation. The coupling G increases most with small gap widths and is thus kept at the minimum fabrication resolution. The support width is kept at a minumum as well, since it significantly affects the bandgap. The bandgap is further affected by the hole lengths, for which the coupling is highest in the center.

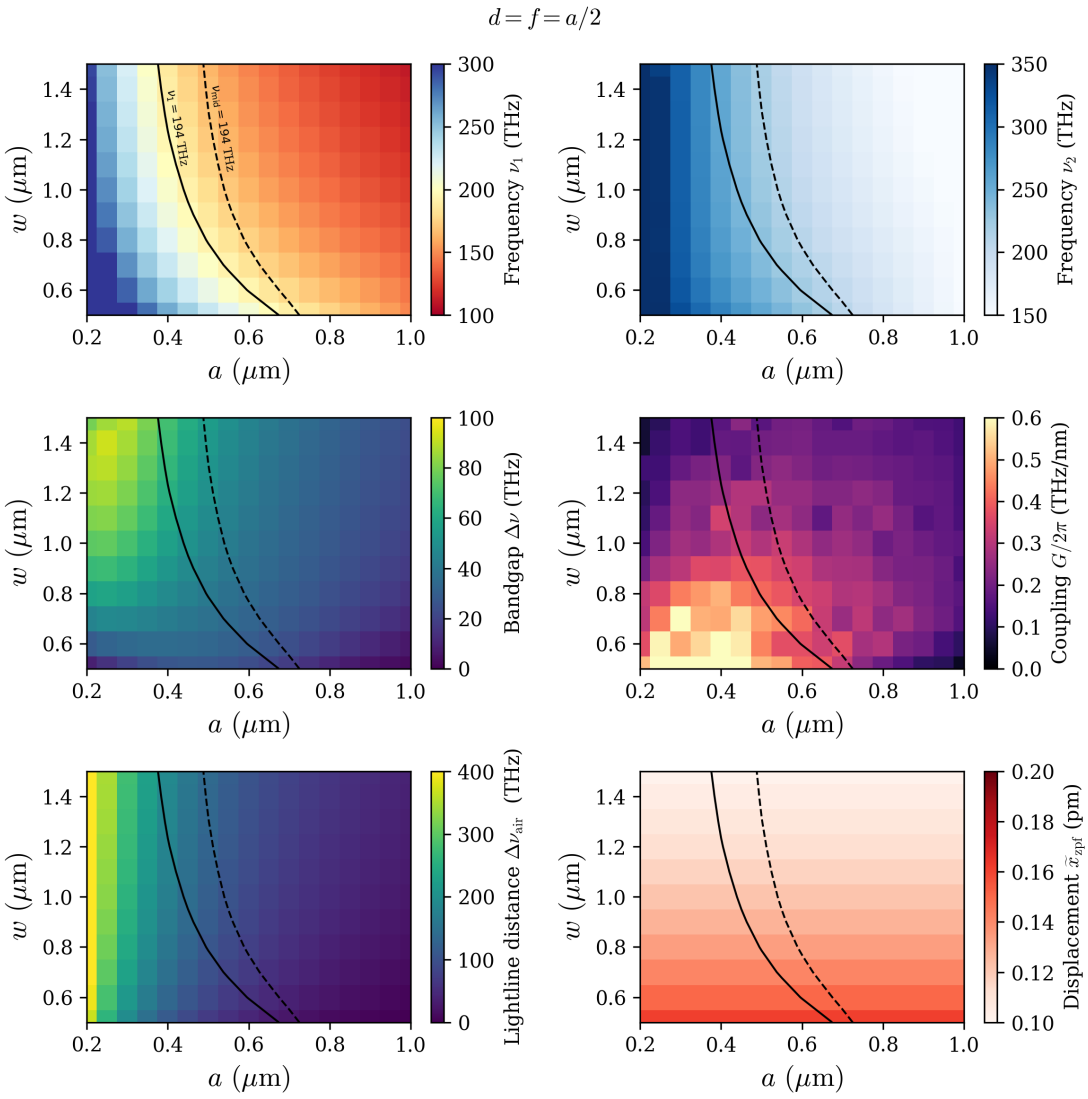

Figure 12. Parametric sweep for a,w with a rectangular hole $d = f = a/2$. The frequency lines for cavity $\nu_1 = 194\,\mathrm{THz}$ (solid) and mirror $\nu_{\mathrm{mid}} = 194\,\mathrm{THz}$ (dashed) are marked with contour lines. ν_1 and ν_2 are brought down by increasing amounts of silicon. We can see that the coupling G is maximized by minimizing both a and w, whereas the bandgap is maximized with larger w. The lightline frequency ν_{air} is inversely proportional to a. The estimated decrease in displacement $\tilde{x}_{\mathrm{zpf}}$ are comparatively small with increasing mass. The upper limit for the optomechanical coupling can be estimated as $g_0 \approx 50\,\mathrm{MHz}$ on the cavity line.

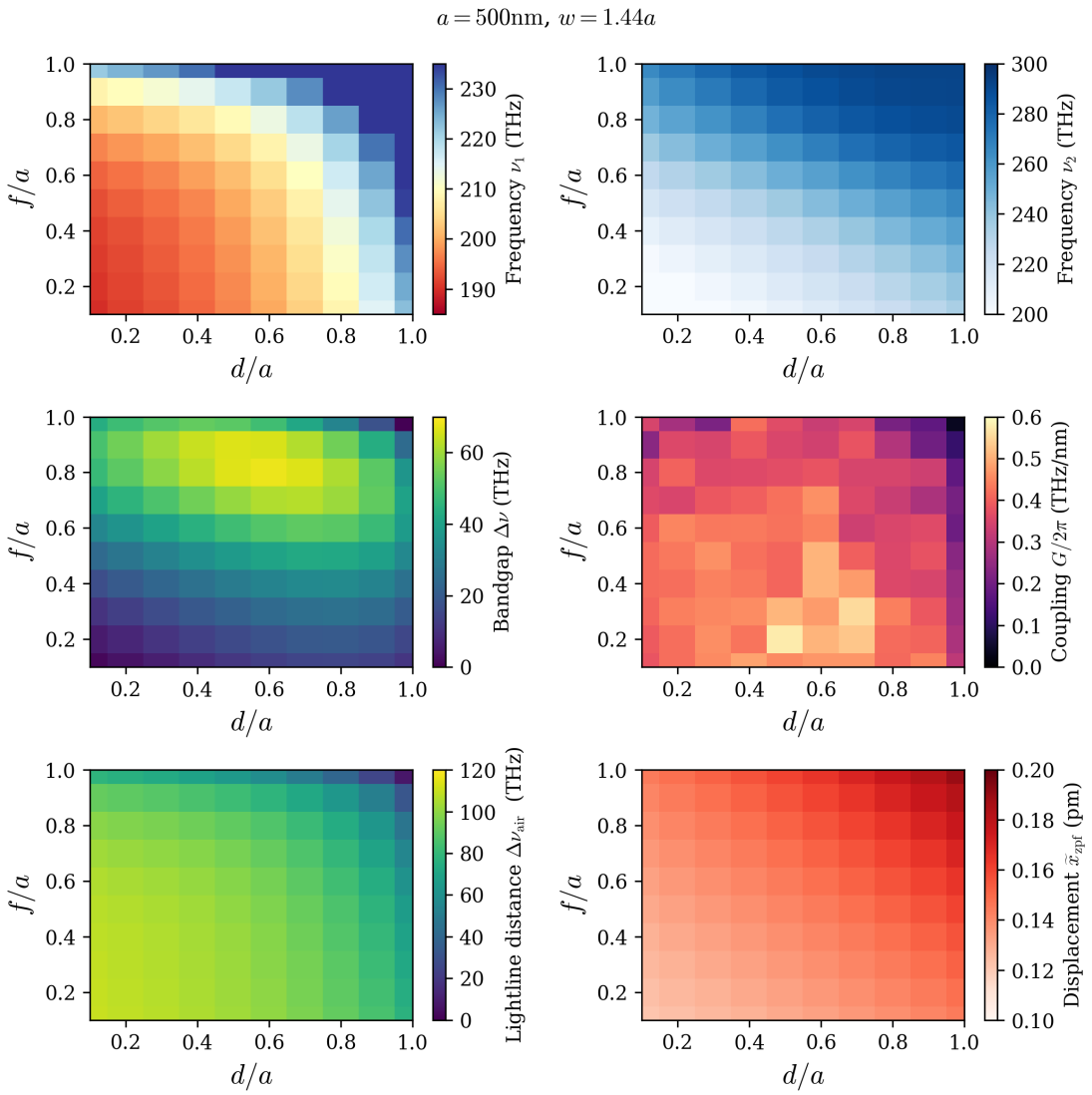

Figure 13. Parametric sweep for trapezoidal hole lengths d,f to find the optimal hole geometry. We can see that **both** the maximum coupling and bandgap can be achieved with $d = (0.6 \pm 0.1)a$. However, the coupling is highest at $f = 0.2a$ whereas the bandgap maximizes at $f = 0.8a$.

of f on $\Delta\nu$ maximizing around $f = 0.8a$. The coupling is instead maximized at $f = 0.2a$.

Most importantly in Figure 13, both the bandgap and coupling seem to maximize with the same values of $d = (0.6 \pm 0.1)a$. This is of great significance to the optimization procedure, as it allows to simplify our search space. We can fix $a = 500\,\text{nm}$ and $d = 0.6a$, and let the tapering of our cavity be entirely done with w and f.

The effect of hole lengths can also be seen in Figure 14, where we compared the bandgap and coupling between different trapezoidal hole shapes. We see that the increase in bandgap by f shifts the ν_1, ν_{mid} further apart. Thus, f has the most effect on the difference between cavity and mirror geometries, and can be used to tune them.

Figure 15 shows a parametric sweep for w,f to identify the most viable tapering path. We noticed that the easiest tapering path should be towards a linear gradient lowering the ν_1 frequency. This keeps the geometry transformations simple and smooth. Alternative paths require more customized and hand-picked points from the tapering line to create a linear increase in mirror strength. Furthermore, the behavior of the bands ν_1 and ν_2 can be dissimilar as in Figure 15, which makes mirror strength estimations more difficult as seen in Appendix A. Since we cannot increase $\Delta\nu$ and ν_2 linearly at the same time by changing f, we choose to fix $f = 0.4a$ as a compromise, and do the tapering only using the beam width w.

In Figure 16 we can see the resulting band structure of a linear width tapering along the line in Figure 15. In order to make the tapered bands more linear, we further adjusted the hole length to $d = 0.5a$. Comparison for Figure 16 can be found in Appendix A, where the tapering has been done by changing f.

4.2 Width tapered high-Q cavity

In previous works [24, 26], the mirror tapering for the nanobeam was done by a gradient search for the optimal mirror geometry, followed by a linear gradient-based decreasing of the ν_1 frequency to the desired cavity frequency. The gradient search was done on a fitness function defined as the multiplication of the figures of merit. Due to the weak gradient and negative effects of the nanobeam width w on coupling strength, the width tapering was discarded altogether. Instead, the tapering was mainly done with the periodicity a.

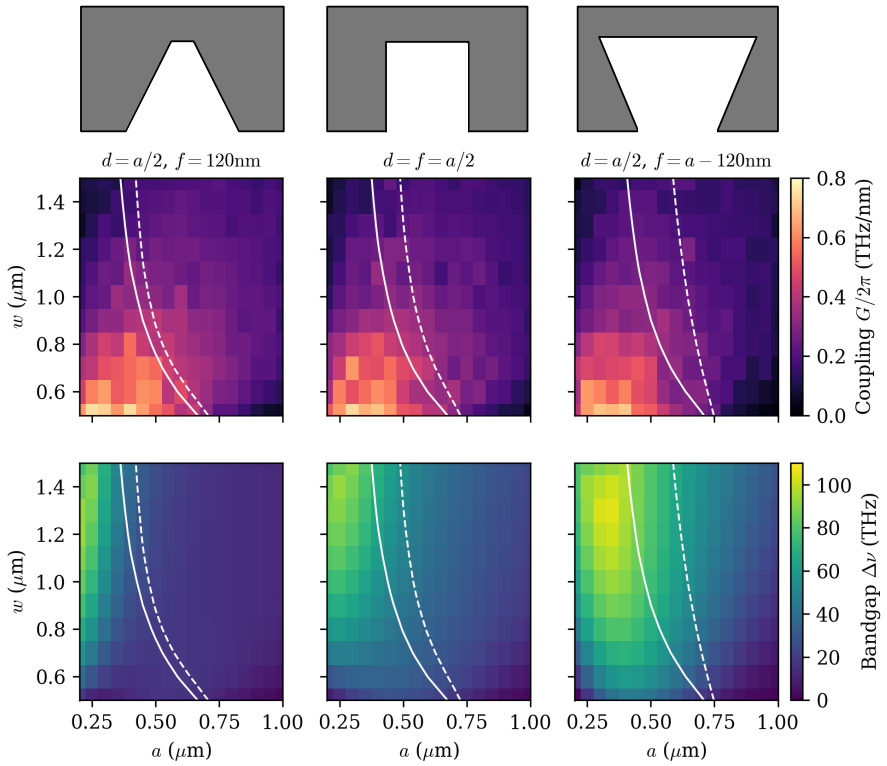

Figure 14. Comparison of coupling and bandgap with regards to different trapezoidal hole shapes. The frequency lines for cavity (solid white) and mirror (dashed white) are drawn for these geometries. Notice how the triangular teeth shape increases coupling, whereas its inversion increases bandgap. The inverted triangular teeth also shift the mirror line away from the cavity line.

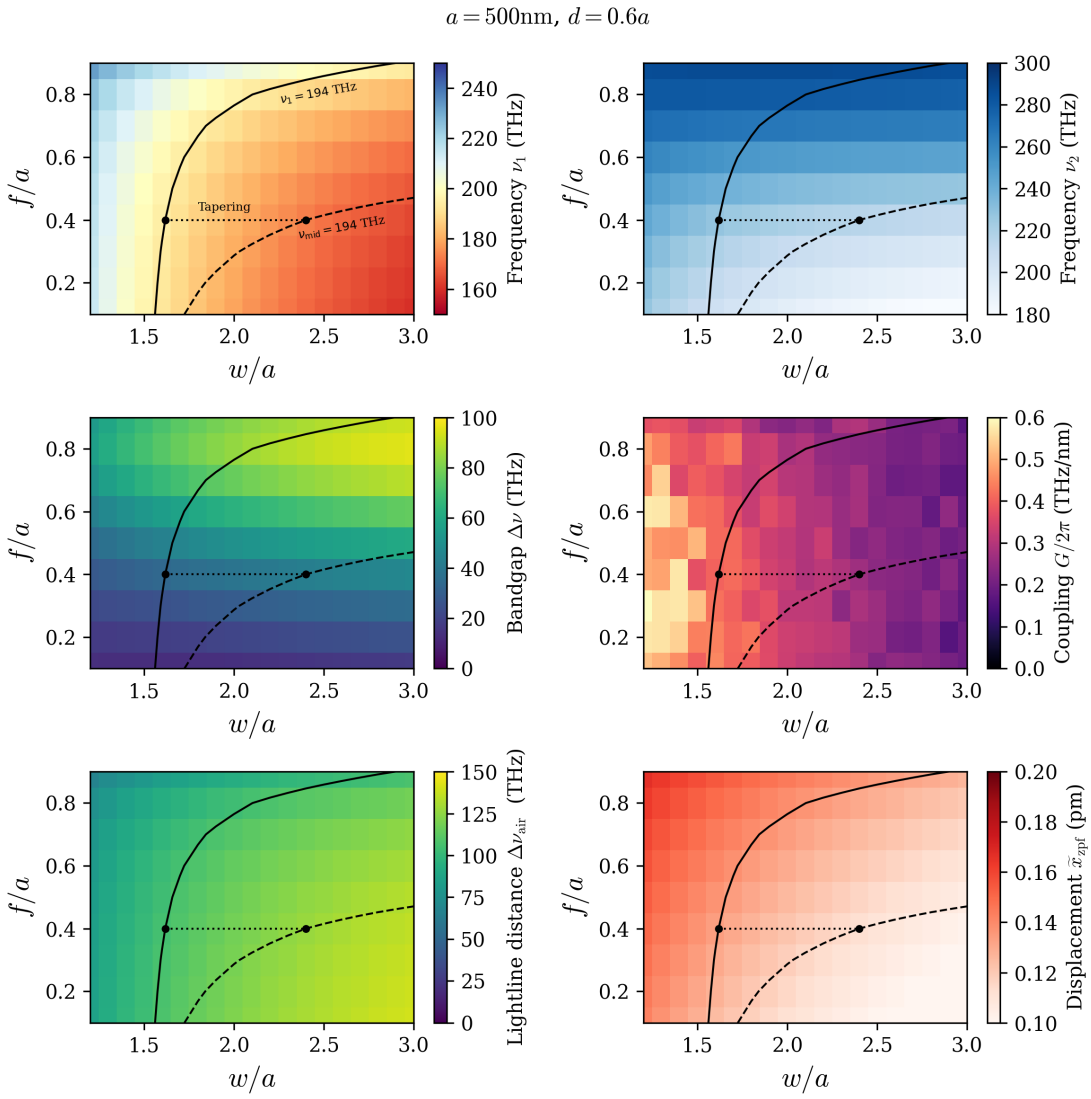

Figure 15. Parametric sweep for w, f with tapering line (dotted) between optimal cavity $\nu_1 = 194\,\text{THz}$ (solid) and mirror $\nu_{\text{mid}} = 194\,\text{THz}$ (dashed) frequency lines. The dots at the ends of the tapering line at $f = 0.4a$ correspond to the estimated cavity $w_{\text{cav}} \approx 800\,\text{nm}$ and mirror $w_{\text{cav}} \approx 1200\,\text{nm}$ widths. Tapering is done using only w in order to keep the change in ν_1, ν_2 smooth and linear as seen in Figure 16.

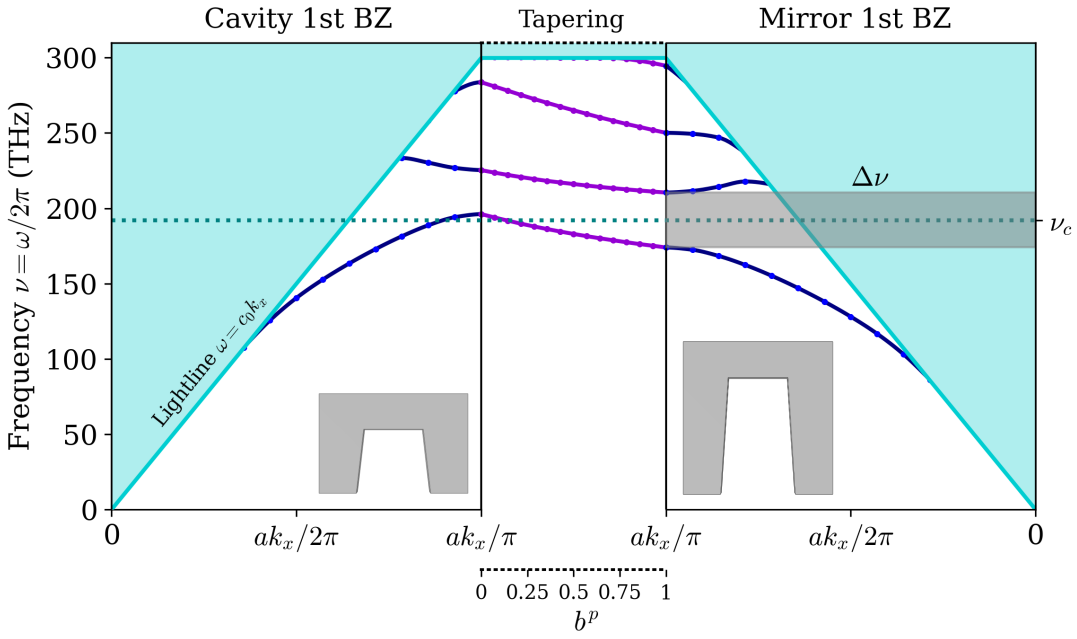

Figure 16. Band structures of cavity $w_\mathrm{c} = 750\,\mathrm{nm}$ and mirror $w_\mathrm{m} = 1100\,\mathrm{nm}$ periodic unit cells with $d = 0.5a$ and $f = 0.4a$. The effect of linear tapering on the BZ edge frequencies is shown in between them. The bandgap center in the mirrors is approximately matched with the cavity frequency ν_c. The cavity frequency ν_c in the cavity is estimated to be slightly lower than the cavity cell frequency ν_1, as seen in the frequency difference between tapered an untapered cavity in Figure 17.

Here, we took a different approach for two reasons. Firstly, matching the phase velocities of the unit cells by keeping a constant is one of the fundamental requirements for a high-Q cavity [42]. Secondly, the periodic constant was kept constant for mirror and cavity. Furthermore, we have prioritized coupling in the cavity cell and bandgap in the mirror cell to optimize both cells separately. This allows the coupling to be higher in regions of highest displacement.

We constructed the full cavity and identify the optimal number N_{cav},N_{tap},N_{mir} of each unit cell to maximize Q-factor of the optical cavity. We first wanted to identify the number of mirror cells needed to minimize scattering along the nanobeam. We picked a number of tapered cells $N_{\mathrm{tap}} = 9$ based on previous work [26, p.33] to reach a high-Q cavity and simulated the Q-factor with additional mirror cells, as shown in Figure 17. The scattering along the nanobeam waveguide is shown to be minimized with 6-7 mirror cells reaching $Q \sim 10^6$. The change in resonance frequency ν_1, mode volume V, as well as Q/V-ratio are shown.

Figure 17 shows also the Q-factor as function of constant cavity and tapered cavity is simulated in for increasing N_{cav} and N_{tap} separately. The maximum Q-factors reached are an order of magnitude lower. The mode volume for the constant cavity is also higher as the cavity holds more nodes of the resonant mode. The tapered cavity shifts the frequency down slightly as compared to the constant cavity.

In Figure 18 we verified the quadratic tapering as the optimal tapering profile by sweeping the scaling power $p = 1 \rightarrow 3$. The cavity Q-factors are highest at $p = 2.2$ keeping above $Q > 10^6$ between $p \in [1.9, 2.5]$. This result also estimates of the resilience of width tapering to fabrication errors.

Figure 19 shows the resonance in the nanobeam around 200 THz of the width tapered nanobeam with the corresponding frequencies ν and Q-factors. Notably, in a tapered cavity structure the fundamental cavity resonance $\nu = 191$ THz (with E-field peak at the center) is supplanted by a resonance $\nu = 179$ THz inside the tapered mirrors as the lowest frequency resonance. The tapered mirrors have a lower TE_1 mode resonance that can still be confined in the structure with sufficiently high Q. However, its optomechanical coupling is lower than the fundamental mode at least in width tapered beams. This is significant distinction to typical cavities, where the fundamental cavity mode is expected to have the lowest frequency. The two modes can be experimentally distinguished by the optomechanical coupling strength and frequency. Using the geometry of the high-Q cavity, a maximum optomechanical

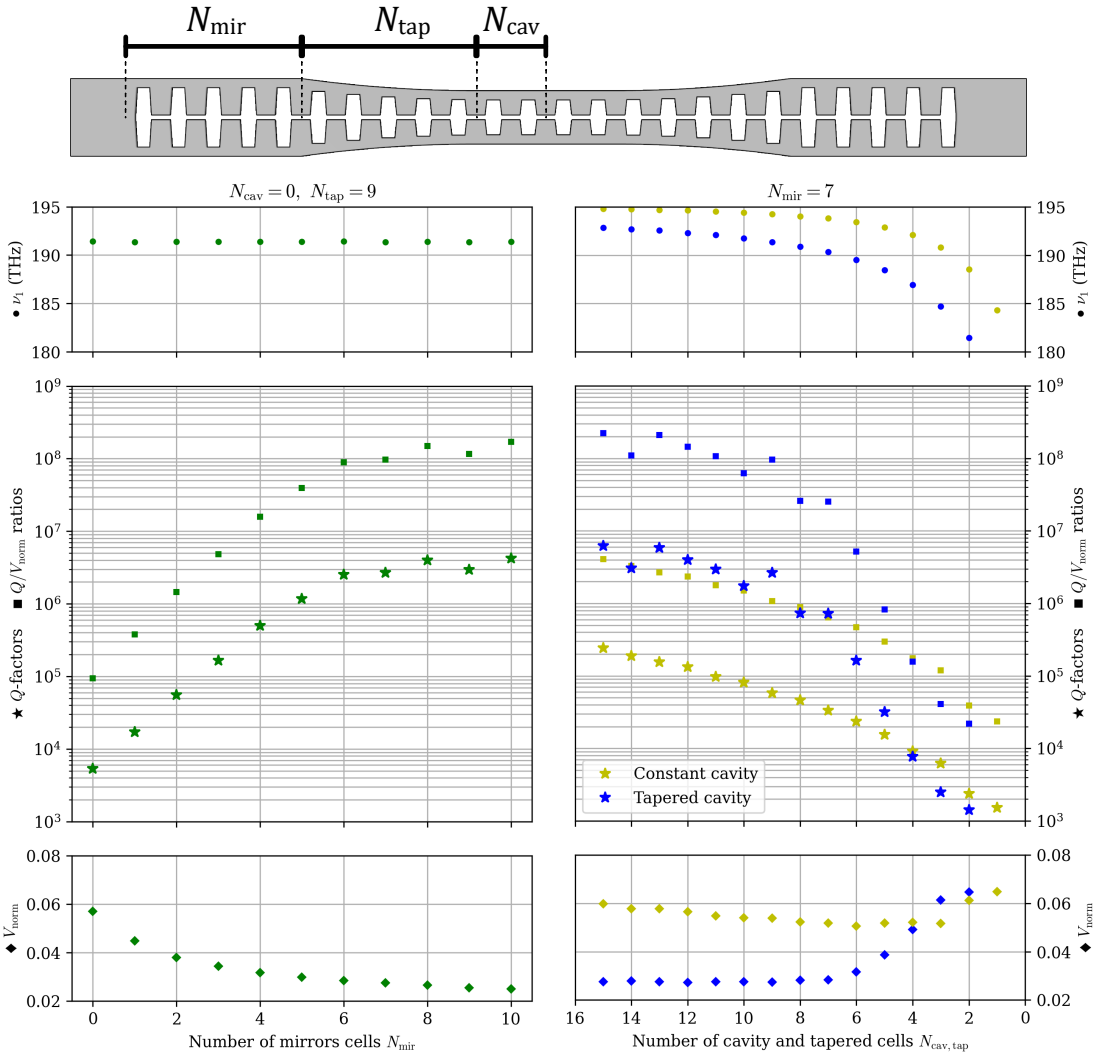

Figure 17. Behavior of ν_1, Q and V_{norm} as function of mirror and quadratically tapered cells in the nanobeam cavity using 1/8th airtube simulations. $Q \sim 10^6$ is reached with $N_{\mathrm{tap}} = 9$ and $N_{\mathrm{mir}} = 7$. The tapered cavity can reach an order of magnitude higher Q-factors than a non-tapered cavity. The tapering shifts the resonance frequency down slightly compared to the untapered constant cavity.

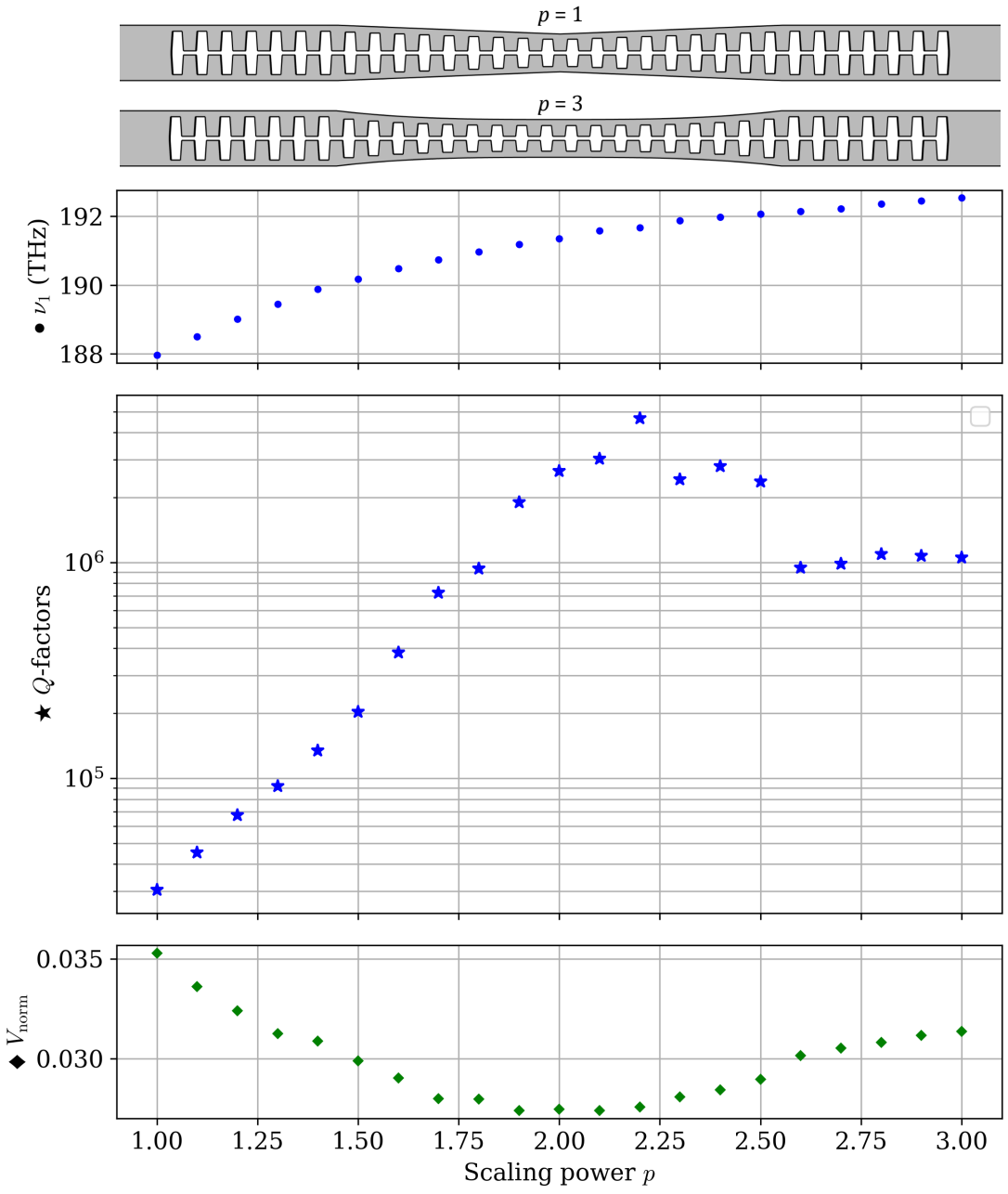

Figure 18. Behavior of ν_1, Q and V_{norm} as function of scaling power p in nanobeam with $N_{\text{tap}} = 9$ and $N_{\text{mir}} = 7$ using 1/8th airtube simulations. The cavity quality is verified to be highest with a quadratic tapering. The Q-factor might be slightly increased by a higher mode volume at higher scaling powers.

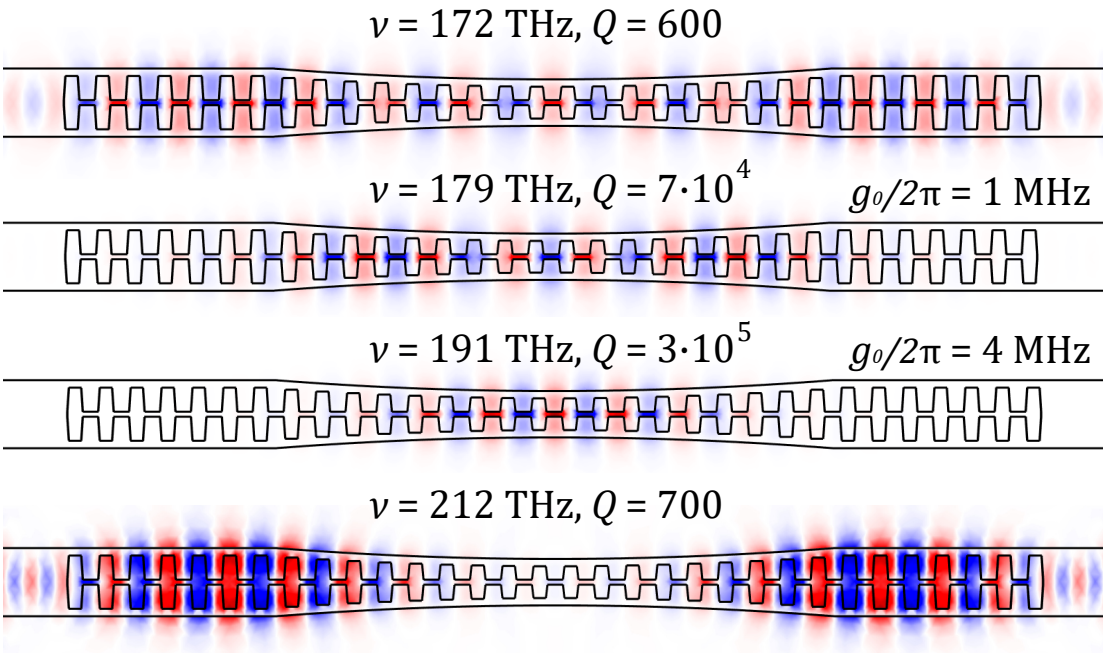

Figure 19. Resonances around 200 THz in a nanobeam cavity with $N_{\mathrm{mir}} = 7, N_{\mathrm{tap}} = 9$ using full airtube simulations. The fundamental mode $\nu = 191$ THz at the center of the cavity is not the lowest frequency mode. The lowest frequency resonance $\nu = 179$ THz is formed within the tapered mirrors (two E-field peaks), where TE_1 mode is still confined to the cavity. The maximum optomechanical couplings g_0 are calculated using $x_{\mathrm{zpf}} = 10^{-13}$. The simulation was done with full airtube.

coupling of 4 MHz is reached.

4.3 Effect of imperfections on Q-factor

As the the fabrication process is never perfect in realizing optimized designs, we also simulated the effect of possible noise in the design in Figure 20. We added a random noise of uniform distribution at different scales $\delta_{\mathrm{noise}} = 0.1$–$100$ nm to all of the (x,y) corner point coordinates of the trapezoidal holes. With this type of noise, the Q-factor of the fundamental cavity mode was observed to scale approximately

$$Q = \frac{Q_{\mathrm{max}}}{(\delta_{\mathrm{noise}}/\alpha_{\mathrm{noise}})^2 + 1},$$

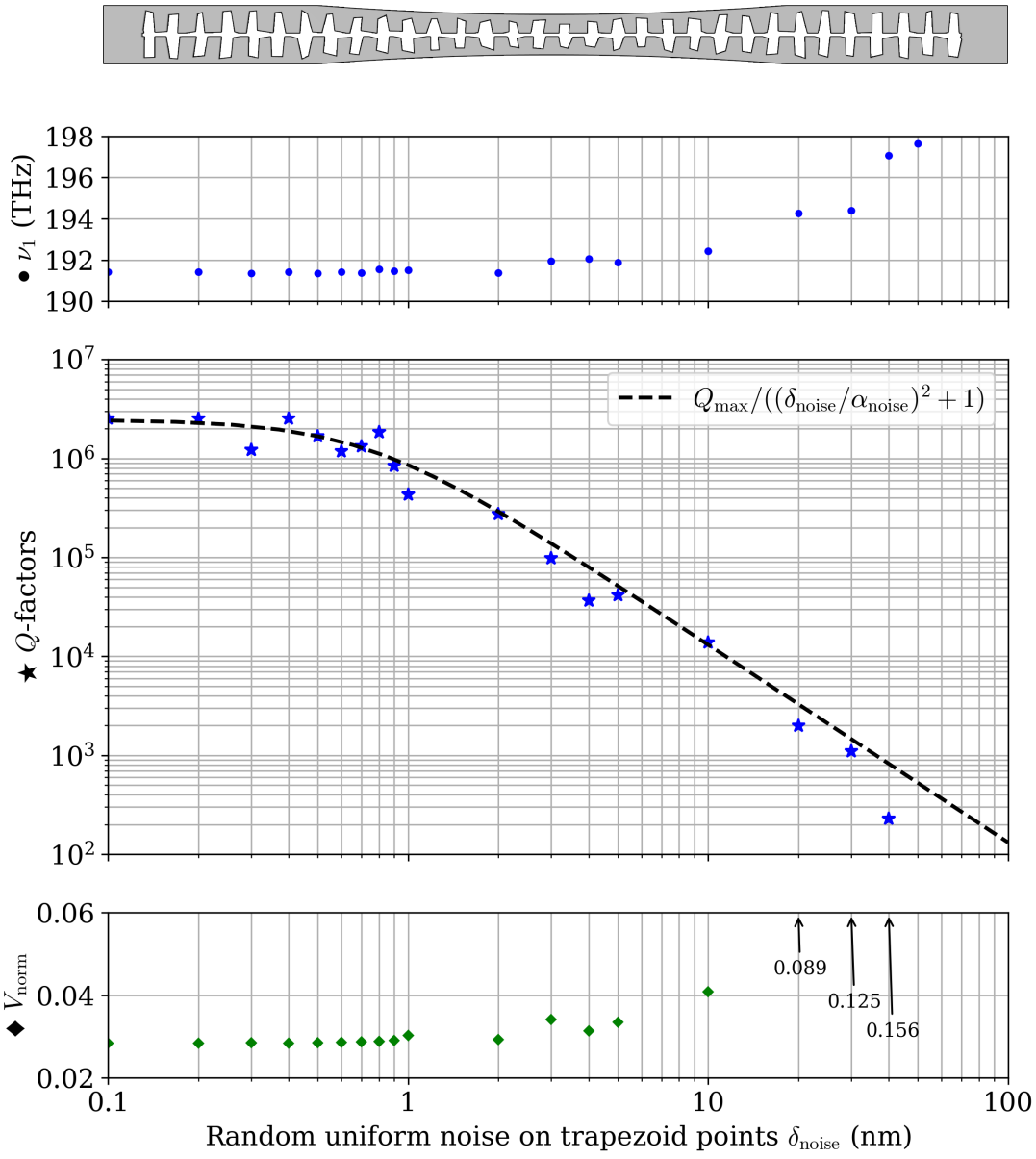

Figure 20. Effect of hole imperfections on the Q-factor using 1/8th airtube simulations. A uniformly random noise δ_{noise} is applied on the point defining the trapezoidal holes. The Q-factors decrease according to $\frac{Q_{\max}}{(\delta_{\text{noise}}/\alpha_{\text{noise}})^2+1}$ where $\alpha^2_{\text{noise}} \approx 0.5\,\text{nm}$ describes the limit for significant losses in the quality of the cavity with $Q_{\max} \sim 10^6$.

where $Q_{\max}$ is the Q-factor without noise, and $\alpha_{\text{noise}} \approx 0.7\,\text{nm}$ is a limit noise derived from a fit in Figure 20. This implies that a cavity with lower Q-factor can be more tolerant to small fabrication errors. Consequently, the Q-factor limit from imperfections can affect the choice of cavity size, as a lesser number of unit cells is required for lesser Q-factors. The amount of error in fabrication sets a limit to the achievable Q-factor of the cavity.

4.4 Double period modulation and far-fields

We estimated the effect of DPM on a cavity with $N_{\text{mir}} = 7, N_{\text{tap}} = 9$. Figure 21 shows the coupling G, Q-factor, and collection ratio η_{avg} as a function of the modulation percentage δ_{mod} for hole lengths $h \in \{d,f\}$. We used a DPM method following $h_{\text{odd}}^{\text{even}} = (1 \pm \delta_{\text{mod}})h$ for odd and even holes starting from the cavity center. We used 1/8th airtube for the simulations.

The modulation did not affect the mode frequency ν_1. However, the Q-factor drops similarly to the uniform noise added on trapezoid points. We derived a similar fit function for the reduction of

$$Q = \frac{Q_{\max}}{(\delta_{\text{mod}}/\alpha_{\text{mod}})^2 + 1},$$

with the limit for significant losses $\alpha_{\text{mod}} \approx 2.2\,\text{nm}$. We further estimated the optomechanical coupling by increasing the gap width by 2 nm. The coupling remained fairly constant fluctuating around 0.6 THz/nm. As for the far-fields and focus of scattering, the average far-field inside our elliptical NA was highest at $\delta_{\text{mod}} = 7\%$ reaching an order of magnitude higher than the average scattering field regardless of direction. This may be attributed to the increase in overall scattering at higher modulation percentages.

Figure 22 depicts the spherical far-field scattering profiles with Mercator projection, where the areas are exaggerated towards the poles $\theta = 0°, 180°$. Here, we used full airtube simulations. We can see that the DPM is effective at focusing the scattering to the center perpendicular to the nanobeam with angle range $\Delta\theta = 20°$ and $\Delta\phi = 80°$ of our NA.

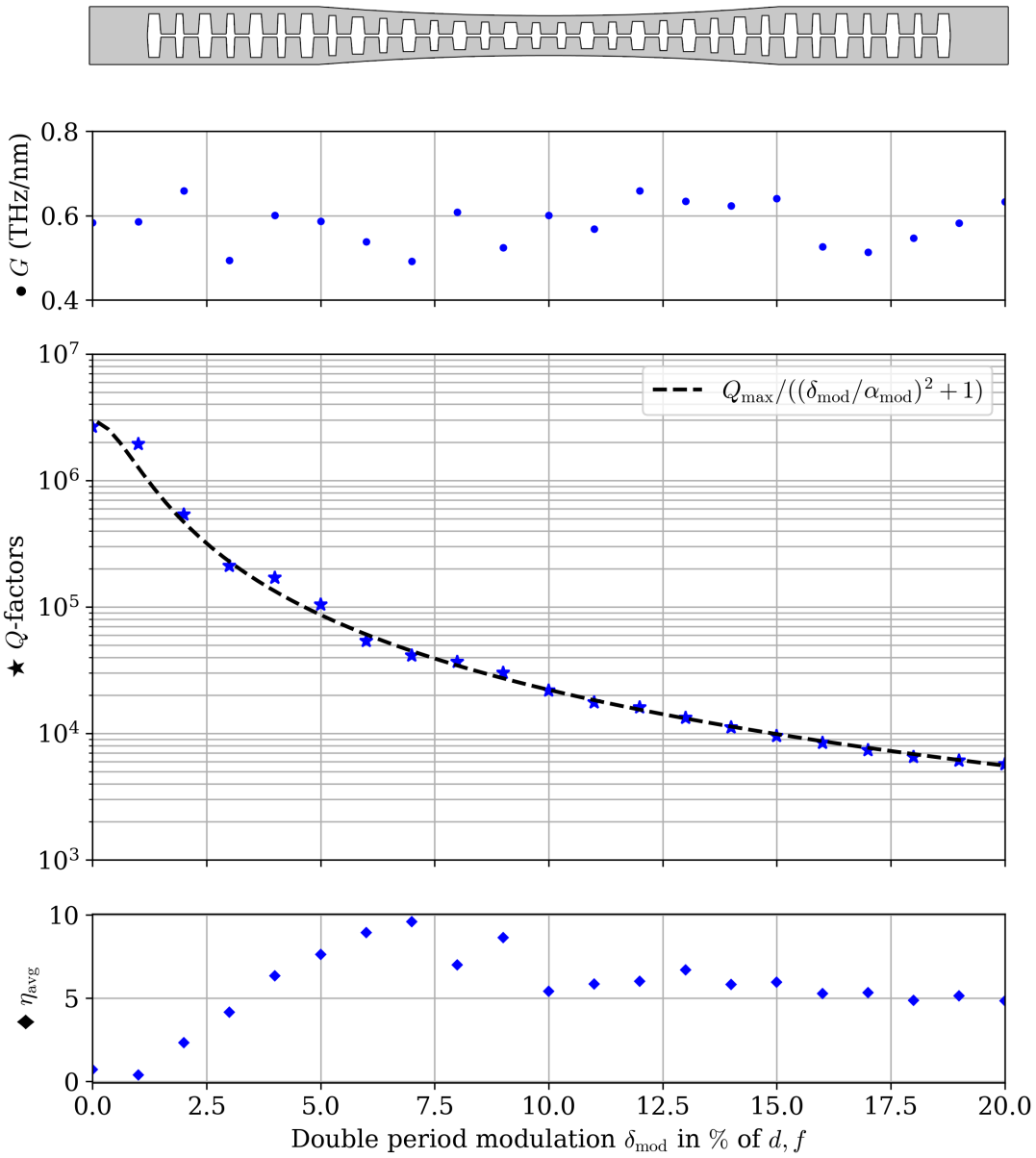

Figure 21. Optomechanical coupling G, Q-factor and collection ratio η_{avg} as a function of double period modulation percentage δ_{mod} on hole dimensions d,f. The limit for significant reduction in Q is determined as $\alpha_{\text{mod}} \approx 0.87\%$. The optomechanical coupling fluctuates around $G = 0.6\,\text{THz/nm}$. The averaged efficiency reaches its maximum at $\delta_{\text{mod}} = 7\%$, where the average far-field inside the NA is an order of magnitude higher than the total average field. The simulation was done with 1/8th airtube.

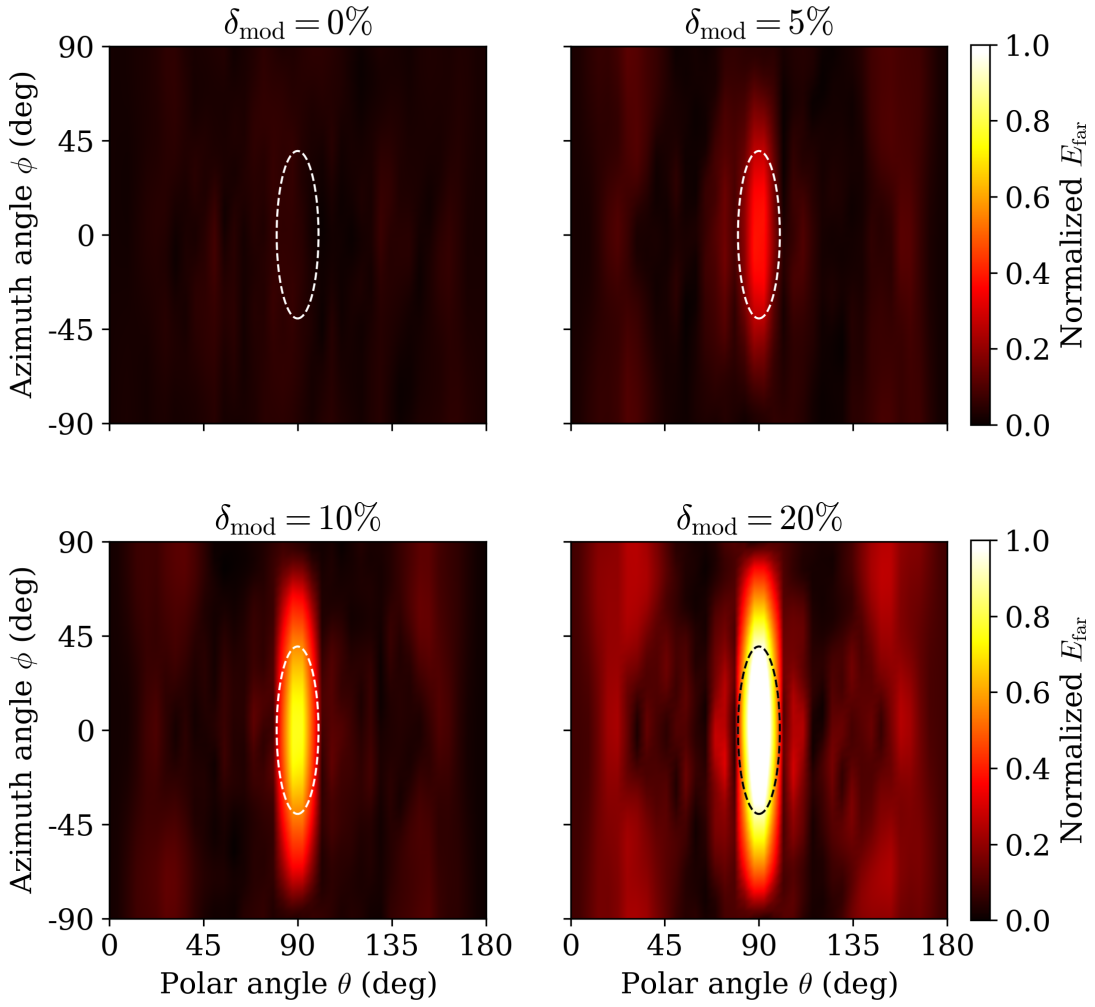

Figure 22. Mercator projected far-field profiles for modulated nanobeam cavity facing x-axis with nanobeam ends at z-axis poles $\theta = 0°, 180°$. At azimuth angles $\phi = \pm 90°$ the scattering is in-plane with the nanobeam. The dashed ellipse corresponds approximately to the NA used for η_{avg}. The far-fields are normalized so that the average field inside the NA is $\bar{E}_{\mathrm{far}}^{\mathrm{NA}} \approx 1$ at $\delta_{\mathrm{mod}} = 20\%$. At $\delta_{\mathrm{mod}} = 20\%$, we can verify that $\eta_{\mathrm{avg}} \approx 5$. The simulation was done with full airtube.

4.5 Strain and displacement behavior

Next, we move on to the mechanical eigenfrequency simulations. We want to design the rest of the nanobeam to maximize the spin coupling to a donor atom. The optimization goals for the nanobeam's breathing mode are

- Maximize the strain $\varepsilon_{xx}^{\mathrm{zpf}} \geq 10^{-8}$ at a sufficiently large volume for a robust ion implementation for strain coupling, or
- Maximize displacement x_{zpf} at the nanobeam center for the magnetic gradient coupling.

Figure 23 compares the $\Omega_{\mathrm{m}}, \max(\varepsilon_{xx})$, and x_{zpf} behavior of a single uniform and a zipper structured nanobeam consisting solely of cavity unit cells. The uniform nanobeams follow the equation (18) almost exactly. The frequency of the zipper structure with 120 nm support follows closely the behavior of a 120 nm wide uniform nanobeam, with slightly lesser displacement and higher strain. Importantly, a maximum strain of 10^{-8} is reached only at $L \leq 5\,\mu$m with eigenfrequencies 2 orders of magnitude higher than our limitation of 3 MHz.

The displacement of the uniform nanobeam is found to scale as $x_{\mathrm{zpf}}^2 \propto \frac{1}{m_{\mathrm{eff}}\Omega_{\mathrm{m}}}$, where the mass scales as $m_{\mathrm{eff}} \propto L$ and $\Omega_{\mathrm{m}} \propto \frac{w}{L^2}$. Clearly, x_{zpf} can be increased simply by maximizing the thin portion of the nanobeam and its length. Based on Figure 23 we can estimate the average zero-point fluctuations to be $x_{\mathrm{zpf}} \sim 0.1$ pm with a maximum of 1 pm for nanobeams with $L < 100\,\mu$m. For spin-magnetic field coupling of $\lambda_{\mathrm{mag}} \geq 1$ kHz, this results in a required field gradient of 36–360 nT/pm.

For the zipper structure, the width of the teeth has a lesser effect on the frequency, since the increase in stiffness is significantly reduced. The strain remains unaffected by the tooth width, whereas both frequency and displacements are slightly reduced.

In Figure 24, we added a uniform extension to the nanobeam cavity with a slit at the joint. We searched for an optimal proportional length of the extension an cavity to maximize bending and strain at the joint. However, the strain increased only together with the eigenfrequency Ω_{m} reaching a peak at $L_{\mathrm{zip}}/L = 0.5$. To minimize the increase in effective mass, we increased the width of the extension at a slightly lower proportion of the extension $L_{\mathrm{zip}}/L = 2/3$. The increase in strain was small and reached a plateau at $w \approx 1\,\mu$m when maximum stiffness was achieved. However, extending a nanobeam cavity of fixed length could be used to tune down the mechanical eigenfrequency.

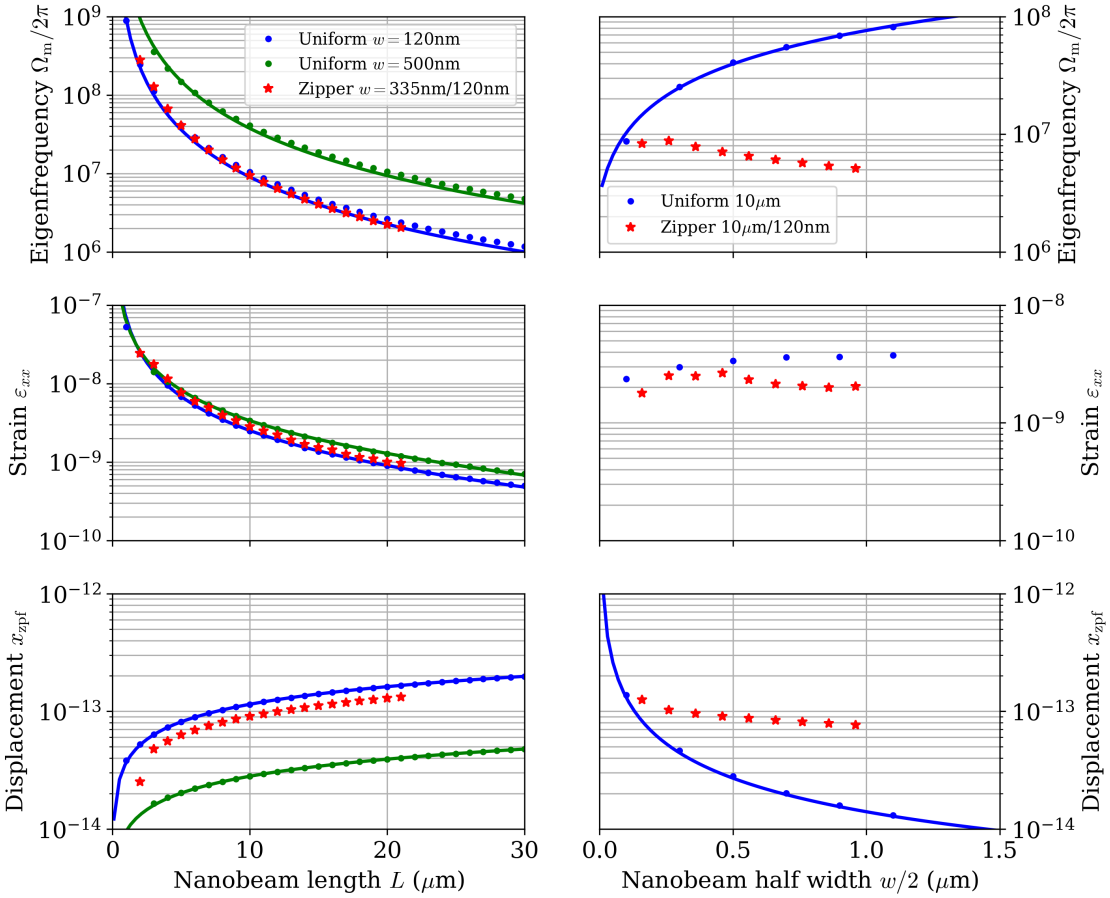

Figure 23. The behavior of Ω_m, ε_{xx}, and x_{zpf} as a function of nanobeam length and width. The properties of zipper structure with a 120 nm support are compared to uniform nanobeams. The lines for uniform nanobeams are drawn using the relations $\Omega_m \propto \varepsilon_{xx} \propto \frac{w}{L^2}$ and $x_{zpf}^2 \propto L$ or $x_{zpf} \propto w$. A strain of 10^{-8} is reached at $L \leq 5\,\mu$m with eigenfrequencies 2 orders of magnitude higher than our limitation of 3 MHz. The width of the zipper teeth affect the strain and displacement only slightly.

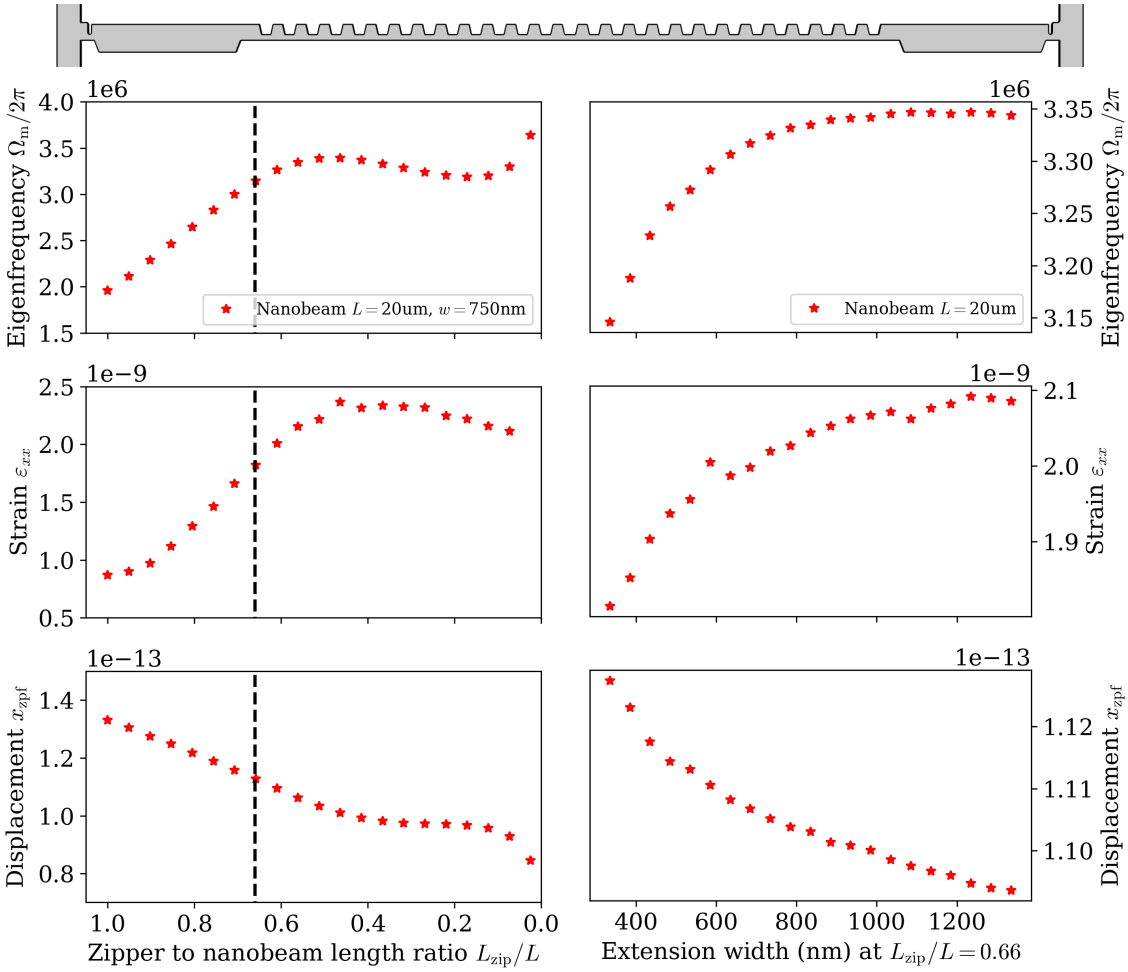

Figure 24. Maximum strain behavior of a nanobeam with uniform extension length and width. Extending the portion of the uniform part increases strain and frequency. The dashed line corresponds to $L_{\text{zip}}/L = 0.66$, where the effect of extension width is simulated. The width of the extensions increases strain and frequency until the maximum stiffness is reached at $1\,\mu$m.

4.6 Strain confinement at the joint

The design of the nanobeam joint itself was done by manual searching. To compare the strains between different design, we used a nanobeam cavity with $N_{\mathrm{cav}} = 10$ to keep the cavity dimensions constant for COMSOL sweeps and the number of unit cells at the limit for $Q \sim 10^5$. The uniform extension of the same width was then used to tune the mechanical frequency to the limit of $\Omega_{\mathrm{m}}/2\pi = 3\,\mathrm{MHz}$. All joints were restricted by the minimum hole resolution of 80 nm and minimum silicon support of 120 nm.

Both unified (Y) and separate joints for the nanobeam halves were explored. The most viable designs are depicted in Figure 25, as well as the strain of the original zipper structure. The tuning down of the frequencies is shown in Figure 26. Last but not least, the most interesting strain distributions are shown in Figures 27, 28, and 29.

In Figure 25 the largest maximum strain was found in an asymmetric design, where the gap was shifted to one side of the nanobeam and a narrow vertical slit was added at the joint. We reached a maximum strain of $\varepsilon_{xx} = 4.3 \cdot 10^{-9}$ at the narrow slit. Both volumetric ε and unidirectional ε_{xx} strains were above 10^{-9} in an ion implantable area of $100 \times 30\,\mathrm{nm}$ near the slit edge, as seen in Figure 27. The strain remained fairly constant throughout the silicon layer thickness of 220 nm. However, the mechanical frequencies of the wider and narrower nanobeam halves differed by about 2 MHz, which adds difficulty to the of measuring displacement in the thicker beam half. With these strains the maximum spin-strain coupling reaches a maximum of $\lambda_0 = 0.3\,\mathrm{kHz}$ with average coupling $\lambda = 0.1\,\mathrm{kHz}$.

The strains at the similar symmetric slit were slightly lesser with $\varepsilon_{xx} = 3.6 \cdot 10^{-9}$. In Figure 28 we see that the volumetric strain stays above 10^{-9} only at the inner edge of the slit. The area for $\varepsilon_{xx} > 10^{-9}$ was also a lesser $70 \times 20\,\mathrm{nm}$. The zero-point displacement x_{zpf} remained higher at 0.1 pm.

Interestingly, in Figure 26 all the higher maximum strains started to decline at higher frequencies. This can be attributed to the higher proportion of the nanobeam being uniform. The strain in the original zipper structure increased almost linearly with frequency. Surprisingly, the Y-notch design had the highest maximum volumetric strain. However, the strain was confined strictly to the center of the joint edge inside the gap in Figure 29.

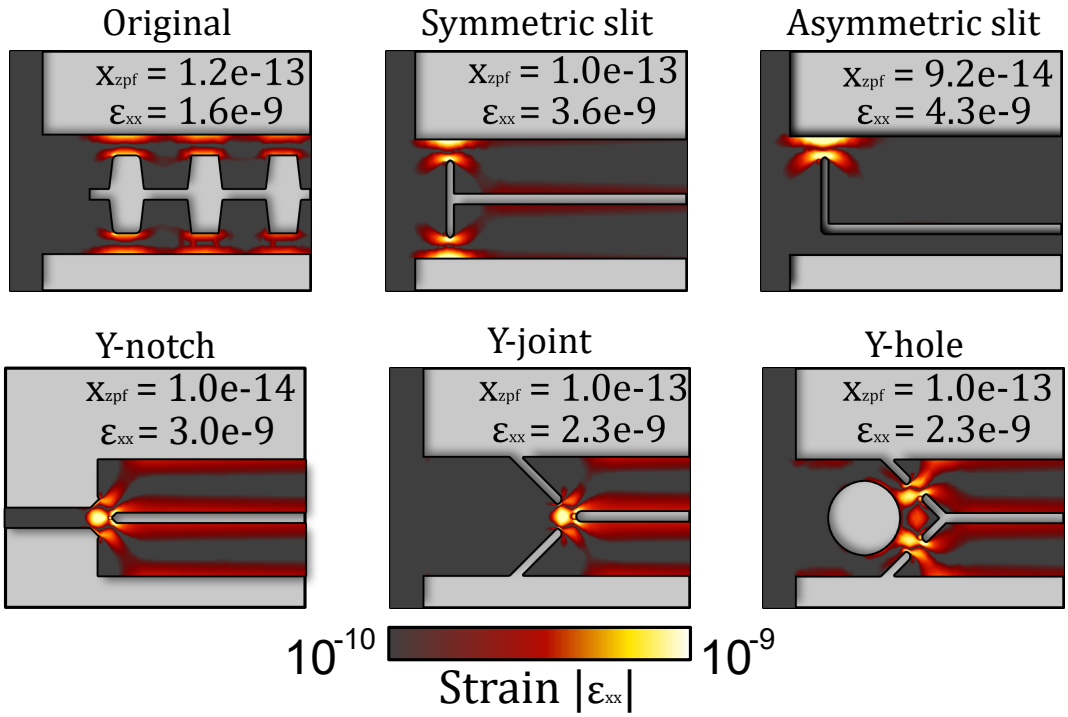

Figure 25. Strain distributions and maximum strains for different nanobeam joint designs at frequency limit $\Omega_{\mathrm{m}}/2\pi = 3\,\mathrm{MHz}$. We used a cavity with $N_{\mathrm{cav}} = 10$, which we set as a limit case for a good quality cavity length with $Q > 10^5$. The frequencies were tuned down with a uniform extension, except for the original upper left structure, where the cavity was extended. The upper right design offered the highest maximum strain with $\varepsilon_{xx} = 4.3 \cdot 10^{-9}$. However, the design for the nanobeam is asymmetric, which means that the two nanobeam halves will have different frequencies.

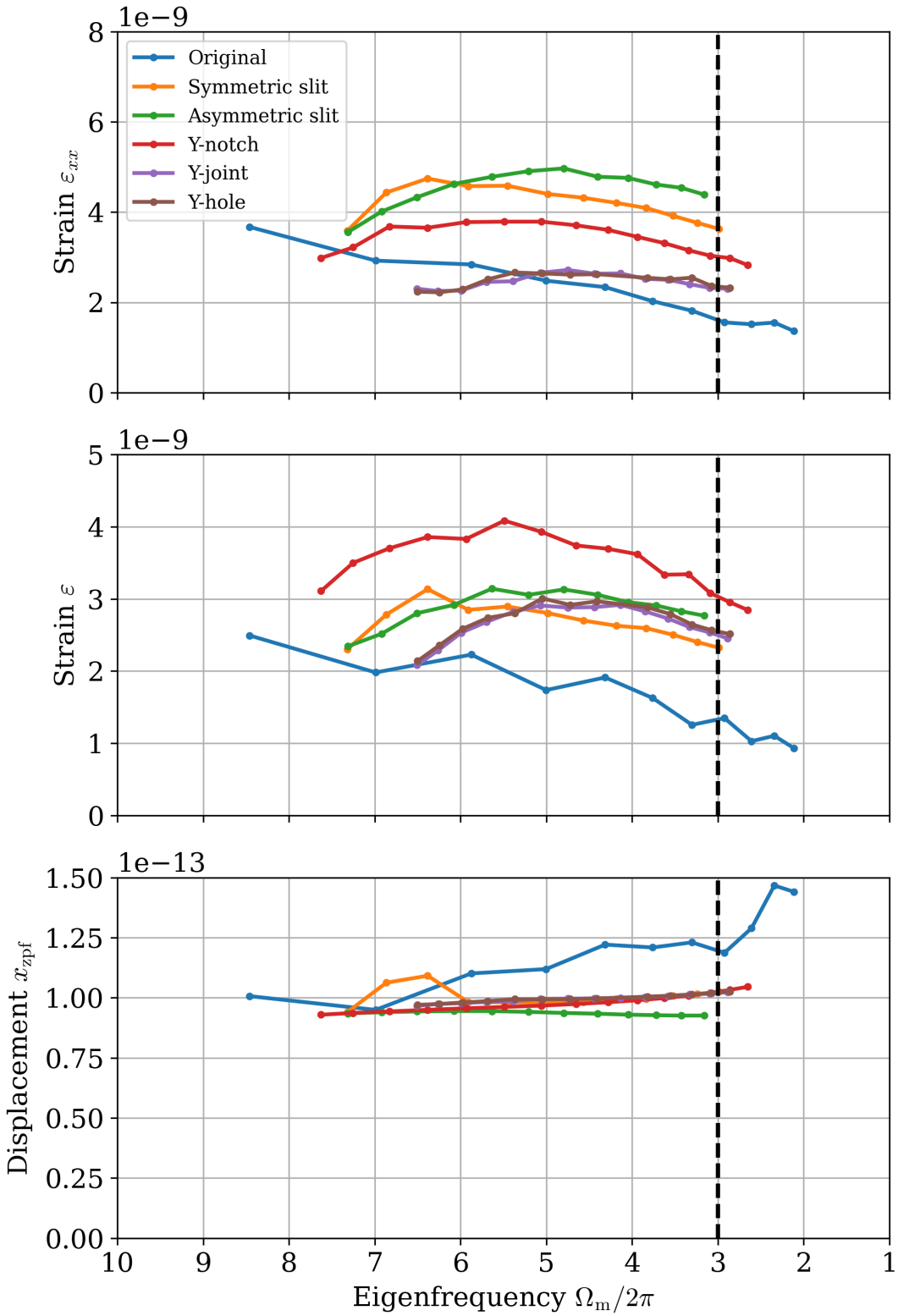

Figure 26. Tuning down the eigenfrequencies for a nanobeam cavity with $N_{\mathrm{cav}} = 10$ by lengthening the uniform extension. As the extension length is increased to approximately 6–7 μm, the eigenfrequency is tuned down to $\Omega_{\mathrm{m}}/2\pi = 3$ MHz. The asymmetric slit has the highest maximum ε_{xx}, whereas the original structure has the highest x_{zpf}. With increasing frequency, the strains drop toward the original zipper structure. Although the higher strain comes at a cost of lowering x_{zpf}, they remain relatively constant at 0.1 pm.

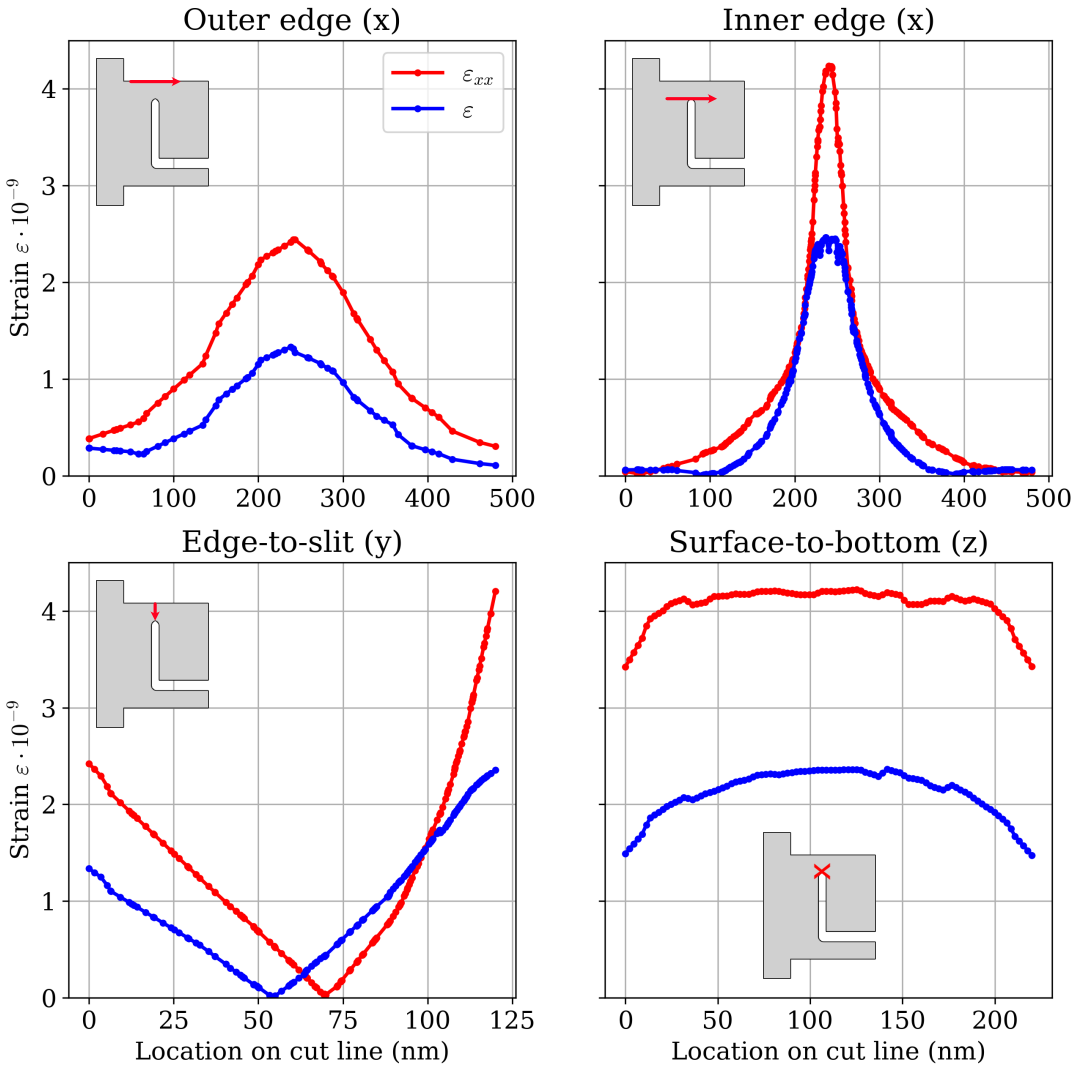

Figure 27. Strain distributions in x,y and z-directions for the asymmetric slit design. The unidirectional strain reaches $\varepsilon_{xx} > 10^{-9}$ in a volume of 200x40x200nm at the outer edge and $100 \times 30 \times 200\,\text{nm}$ around the slit. In the z-direction the stain is relatively constant. The maximum strain of $\varepsilon_{xx} = 4.3 \cdot 10^{-9}$ is located at the very end of the slit. Both the inner and outer edge at the slit provide a good location for donor spins.

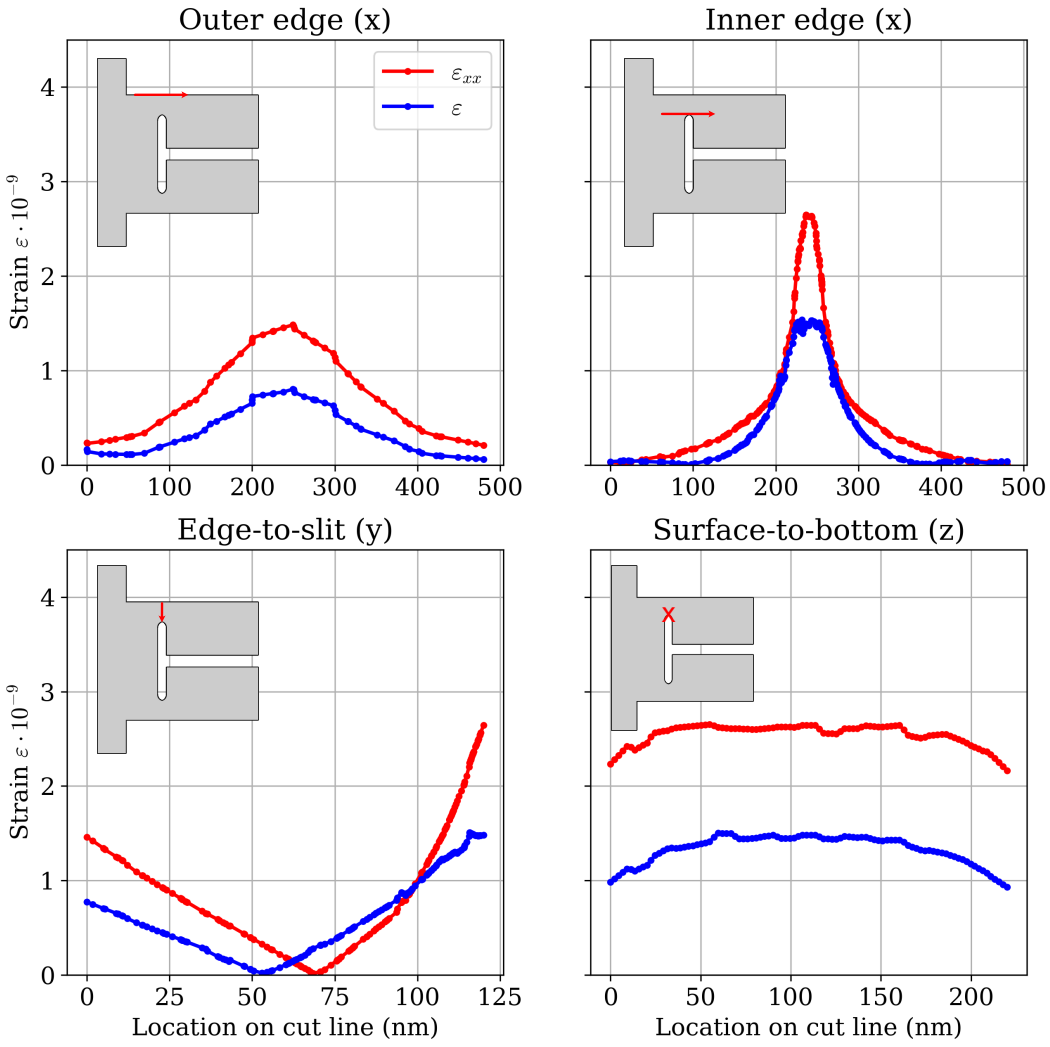

Figure 28. Strain distributions in x,y and z-directions for the symmetric slit design. The strains are slightly lesser than its asymmetric counterpart. The unidirectional strain still reaches $\varepsilon_{xx} > 10^{-9}$ in a volume of $100 \times 10 \times 200\,\text{nm}$ at the outer edge and $70 \times 20 \times 200\,\text{nm}$ around the slit.

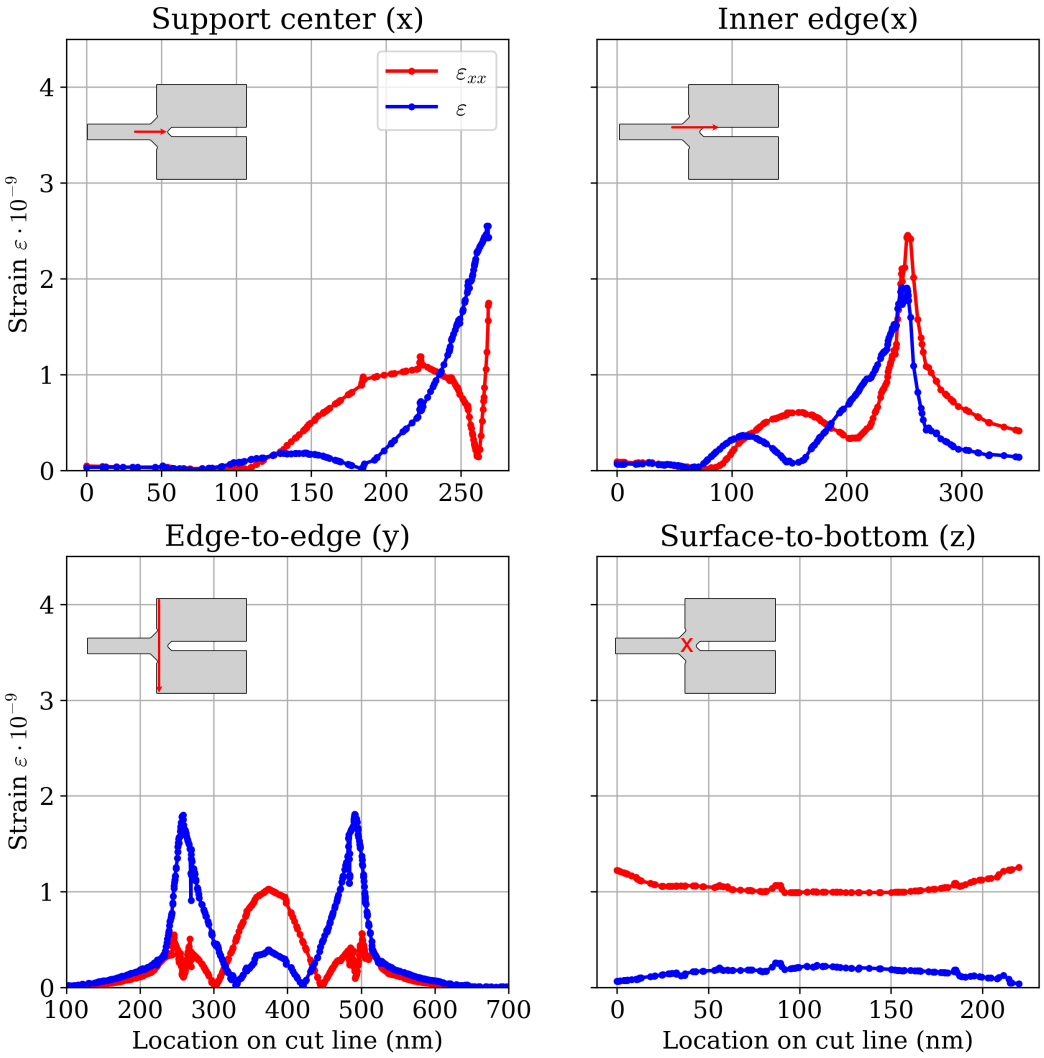

Figure 29. Strain distributions in x,y and z-directions for the Y-notch design. The maximum volumetric strain seen in Figure 26 is very tightly located at the end of the gap. At the center of the joint, the strain barely reaches $\varepsilon_{xx} = 10^{-9}$. Thus, the inner edge of the joint might be the most suitable location for donor spins.

5 Conclusions

This thesis considered the design of a width tapered photonic nanobeam cavity with simulated quality factors reaching $Q \sim 10^6$ with normalized mode volumes of $V_{\text{norm}} \approx 0.03$ and a maximum optomechanical coupling of $g_0/2\pi = 4\,\text{MHz}$. We estimated imperfections to start affecting the cavity Q-factor at the size of $\alpha_{\text{noise}} \approx 0.7\,\text{nm}$. We also applied a double period modulation on hole length to achieve an average field ratio of $\eta_{\text{avg}} \approx 10$ at $\delta_{\text{mod}} = 7\%$ modulation within an elliptical aperture of $\Delta\theta = 20°$ and $\Delta\phi = 80°$.

We simulated the zero-point fluctuation diplacements of the nanobeam to range $x_{\text{zpf}} = 0.1$–$1\,\text{pm}$. For a spin-magnetic field coupling to reach a required $\lambda_{\text{mag}} \geq 1\,\text{kHz}$ for single ^{31}P donor spin measurements, we detemined a corresponding requirement of $\nabla B_x = 36$–$360\,\text{nT/pm}$ for the field gradient of an external magnet.

Additionally, we added a strain confinement design to the nanobeam joints. We reached a maximum unidirectional strain of $\varepsilon_{xx} = 4.3 \cdot 10^{-9}$ and a volume of 200x40x200nm for strains $\varepsilon_{xx} > 10^{-9}$. This resulted in an average spin-mechanical coupling of $\lambda_0 = 0.1\,\text{kHz}$ with a maximum of $\lambda_0 = 0.3\,\text{kHz}$. For the coupling we used the experimental limitations for the application of qubit dressing with mechanical frequency of $\Omega_{\text{m}} \leq 3\,\text{MHz}$ and magnetic fields $B \leq 1\,\text{T}$. Unfortunately, we did not achieve the strain $\varepsilon_{xx} \geq 10^{-8}$ required for spin-phonon coupling of $\lambda_0 \geq 1\,\text{kHz}$ for single spin measurements, as the optimized strains were still an order of magnitude too low. Nevertheless, the simulated device is still feasible for bulk spin measurements with the scaling of spin coupling $\sqrt{N}\lambda_0$ with N spins.

The strain was mainly affected by the fluctuation energy determined by the mechanical eigenfrequency and confinement of bending to the narrow joint of the nanobeam. However, higher bending at joint was at odds with the zero-point displacement x_{zpf} since it was caused by increased the mass and stiffness of the nanobeam. Thus, the increase in spin-strain coupling was only possible at the cost of optomechanical coupling.

As noted in previous works, the optomechanical coupling is most affected and restricted by the gap width separating the two nanobeam halves [25, 26]. Thus,

increasing the fabrication resolution towards thinner slits is of utmost importance. The relative sizes of the nanobeam width, gap and x_{zpf} as the major influences for g_0 suggests that the width tapering might not be the optimal approach. Indeed, as the Q-factors did not increase past 10^6, a periodicity tapering might be more optimal for higher optomechanical coupling.

Notably, we learned that the phase matching did not yield any extra benefit compared to tapering with periodicity a in previous theses [25, 26]. However, unlike noted in the theses, a width tapered sliced nanobeam proved to be feasible. The cavity quality was still limited to $Q \sim 10^6$. This was largely due to the fact that a simple continuous geometry transformation was not possible between PhC geometries for maximal mirror strength $\gamma, \Delta\nu$ and maximal optomechanical coupling G. Especially the different direction of gradient for lowering ν_1 and lifting ν_2 prevented the tapering between a high coupling and large bandgap geometries in Figure 15, as γ would not be constantly increasing.

For further improvements on the design, utilizing external nanomagnets seemed to be way to go. Reaching an order of magnitude higher strain distribution would be tedious even for thinner silicon structures. The feasibility of nanobeams with nanomagnets are studied in [50]. An alternative route for spin-strain coupling would be to increase the mechanical frequency to GHz. However, since the qubit dressing protocol is limited by the magnetic fields, the inability to utilize it would lead to a significant loss in decoherence for the spin qubits.

References

[1] G. Tóth and I. Apellaniz. "Quantum metrology from a quantum information science perspective". In: *Journal of Physics A: Mathematical and Theoretical* 47 (42 Oct. 2014). ISSN: 17518121. DOI: 10.1088/1751-8113/47/42/424006.

[2] C. L. Degen, F. Reinhard, and P. Cappellaro. "Quantum sensing". In: *Reviews of Modern Physics* 89 (3 July 2017). ISSN: 15390756. DOI: 10.1103/RevModPhys.89.035002.

[3] D. D. Awschalom et al. "Quantum technologies with optically interfaced solid-state spins". In: *Nature Photonics 2018 12:9* 12 (9 Aug. 2018), pp. 516–527. ISSN: 1749-4893. DOI: 10.1038/s41566-018-0232-2. URL: https://www.nature.com/articles/s41566-018-0232-2.

[4] C. Noh and D. G. Angelakis. "Quantum simulations and many-body physics with light". In: *Reports on Progress in Physics* 80 (1 Jan. 2017). ISSN: 00344885. DOI: 10.1088/0034-4885/80/1/016401.

[5] J. Preskill. "Quantum Computing in the NISQ era and beyond". In: *Quantum* 2 (Jan. 2018). DOI: 10.22331/q-2018-08-06-79. URL: http://arxiv.org/abs/1801.00862.

[6] J. I. Cirac and P. Zoller. "Quantum Computations with Cold Trapped Ions". In: *Physical Review Letters* 74 (20 May 1995), pp. 4091–4094. DOI: 10.1103/PhysRevLett.74.4091. URL: https://link.aps.org/doi/10.1103/PhysRevLett.74.4091.

[7] N. A. Gershenfeld and I. L. Chuang. "Bulk Spin-Resonance Quantum Computation". In: *Science* 275.5298 (1997), pp. 350–356. DOI: 10.1126/science.275.5298.350. eprint: https://www.science.org/doi/pdf/10.1126/science.275.5298.350.

[8] B. E. Kane. "A silicon-based nuclear spin quantum computer". In: *Nature* 393 (6681 May 1998), pp. 133–137. ISSN: 1476-4687. DOI: 10.1038/30156. URL: https://www.nature.com/articles/30156.

[9] D. Loss and D. P. DiVincenzo. “Quantum computation with quantum dots”. In: *Physical Review A* 57 (1 Jan. 1998), pp. 120–126. DOI: 10.1103/PhysRevA.57.120. URL: https://link.aps.org/doi/10.1103/PhysRevA.57.120.

[10] E. Knill, R. Laflamme, and G. J. Milburn. “A scheme for efficient quantum computation with linear optics”. In: *Nature* 409 (6816 Jan. 2001), pp. 46–52. ISSN: 1476-4687. DOI: 10.1038/35051009. URL: https://www.nature.com/articles/35051009.

[11] A. Blais et al. “Cavity quantum electrodynamics for superconducting electrical circuits: an architecture for quantum computation”. In: *Physical Review A - Atomic, Molecular, and Optical Physics* 69 (6 Feb. 2004). DOI: 10.1103/PhysRevA.69.062320. URL: http://arxiv.org/abs/cond-mat/0402216.

[12] M. Kjaergaard et al. “Superconducting Qubits: Current State of Play”. In: *Annual Review of Condensed Matter Physics* 11 (May 2019), pp. 369–395. DOI: 10.1146/annurev-conmatphys-031119-050605. URL: http://arxiv.org/abs/1905.13641.

[13] G. Wolfowicz and D. Watson. “Quantum control of donor spins in silicon and their environment”. PhD thesis. University of Oxford, 2015.

[14] J. T. Muhonen et al. “Storing quantum information for 30 seconds in a nanoelectronic device”. In: *Nature Nanotechnology* 9 (2014). DOI: 10.1038/NNANO.2014.211.

[15] J. J. Burnett et al. “Decoherence benchmarking of superconducting qubits”. In: *npj Quantum Information* 5 (1 June 2019), pp. 1–8. ISSN: 2056-6387. DOI: 10.1038/s41534-019-0168-5. URL: https://www.nature.com/articles/s41534-019-0168-5.

[16] F. Flamini, N. Spagnolo, and F. Sciarrino. “Photonic quantum information processing: A review”. In: *Reports on Progress in Physics* 82 (1 Jan. 2019). ISSN: 00344885. DOI: 10.1088/1361-6633/aad5b2.

[17] T. E. Northup and R. Blatt. “Quantum information transfer using photons”. In: *Nature Photonics* 8 (5 2014), pp. 356–363. ISSN: 17494893. DOI: 10.1038/NPHOTON.2014.53.

[18] K. Heshami et al. “Quantum memories: emerging applications and recent advances”. In: *Journal of Modern Optics* 63 (20 2016), pp. 2005–2028. ISSN: 1362-3044. DOI: 10.1080/09500340.2016.1148212. URL: https://www.tandfonline.com/action/journalInformation?journalCode=tmop20.

[19] A. Wallucks et al. “A quantum memory at telecom wavelengths”. In: *Nature Physics* 16 (7 May 2020), pp. 772–777. ISSN: 1745-2481. DOI: 10.1038/s41567-020-0891-z. URL: https://www.nature.com/articles/s41567-020-0891-z.

[20] D. Lee et al. “Topical review: Spins and mechanics in diamond”. In: *Journal of Optics (United Kingdom)* 19 (3 Mar. 2017). ISSN: 20408986. DOI: 10.1088/2040-8986/AA52CD.

[21] M. C. Löbl et al. “Excitons in InGaAs quantum dots without electron wetting layer states”. In: *Communications Physics* 2 (1 Aug. 2019), pp. 1–7. ISSN: 2399-3650. DOI: 10.1038/s42005-019-0194-9. URL: https://www.nature.com/articles/s42005-019-0194-9.

[22] D. A. Vajner et al. “Quantum Communication Using Semiconductor Quantum Dots”. In: *Advanced Quantum Technologies* 5 (7 July 2022). ISSN: 25119044. DOI: 10.1002/QUTE.202100116.

[23] “Optical observation of single spins in silicon”. In: *Nature 2022 607:7918* 607 (7918 July 2022), pp. 266–270. ISSN: 1476-4687. DOI: 10.1038/s41586-022-04821-y. URL: https://www.nature.com/articles/s41586-022-04821-y.

[24] R. Leijssen and E. Verhagen. “Strong optomechanical interactions in a sliced photonic crystal nanobeam”. In: *Scientific Reports* 5 (May 2015). DOI: 10.1038/srep15974. URL: http://arxiv.org/abs/1505.00324.

[25] R. Leijssen. “Measuring mechanical motion using light confined at the nanoscale”. PhD thesis. AMOLF, 2017.

[26] L. Freisem. “Low-loss photonic nanocavities with strong optomechanical interactions”. Master’s thesis. AMOLF, 2015.

[27] A. van der Hel. “Sliced photonic crystal nanobeam as a spin-to-photon quantum transducer”. Master’s thesis. AMOLF, 2018.

[28] J. P. Dehollain et al. “Nanoscale broadband transmission lines for spin qubit control”. In: *Nanotechnology* 24 (1 Aug. 2012). DOI: 10.1088/0957-4484/24/1/015202. URL: http://arxiv.org/abs/1208.2421.

[29] A. Laucht et al. “A Dressed Spin Qubit in Silicon”. In: *Nature Nanotechnology* 12 (1 Mar. 2016), pp. 61–66. DOI: 10.1038/nnano.2016.178. URL: http://arxiv.org/abs/1603.04800.

[30] H. Wang and I. Lekavicius. “Coupling spins to nanomechanical resonators: Toward quantum spin-mechanics”. In: *Applied Physics Letters* 117 (23 Dec. 2020), p. 230501. ISSN: 00036951. DOI: 10.1063/5.0024001/14541883/230501_1_ACCEPTED_MANUSCRIPT.PDF.

[31] M. Imboden, P. Mohanty, and G. Bauer. “Dissipation in nanoelectromechanical systems editor”. In: *Physics Reports* 534 (2014), pp. 89–146. DOI: 10.1016/j.physrep.2013.09.003. URL: http://dx.doi.org/10.1016/j.physrep.2013.09.003.

[32] J. D. Joannopoulos et al. *Photonic Crystals: Molding the Flow of Light (Second Edition)*. Princeton University Press, 2011. ISBN: 9780691124568.

[33] E. Jaynes and F. Cummings. “Comparison of quantum and semiclassical radiation theories with application to the beam maser”. In: *Proceedings of the IEEE* 51.1 (1963), pp. 89–109. DOI: 10.1109/PROC.1963.1664.

[34] D. Manzano. “A short introduction to the Lindblad master equation”. In: *AIP Advances* 10.2 (Feb. 2020), p. 025106. ISSN: 2158-3226. DOI: 10.1063/1.5115323. eprint: https://pubs.aip.org/aip/adv/article-pdf/doi/10.1063/1.5115323/12881278/025106_1_online.pdf.

[35] J. Mansir et al. “Linear Hyperfine Tuning of Donor Spins in Silicon Using Hydrostatic Strain”. In: *Physical Review Letters* 120 (16 Apr. 2018), p. 167701. ISSN: 10797114. DOI: 10.1103/PHYSREVLETT.120.167701/FIGURES/4/MEDIUM. URL: https://journals.aps.org/prl/abstract/10.1103/PhysRevLett.120.167701.

[36] J. Larson and E. K. Irish. “Some remarks on ’superradiant’ phase transitions in light-matter systems”. In: *Journal of Physics A: Mathematical and Theoretical* 50 (17 Dec. 2016). DOI: 10.1088/1751-8121/aa65dc. URL: http://arxiv.org/abs/1612.00336.

[37] R. H. Dicke. "Coherence in Spontaneous Radiation Processes". In: *Physical Review* 93 (1 Jan. 1954), pp. 99–110. DOI: 10.1103/PhysRev.93.99. URL: https://link.aps.org/doi/10.1103/PhysRev.93.99.

[38] M. Tavis and F. W. Cummings. "Exact Solution for an N-Molecule—Radiation-Field Hamiltonian". In: *Physical Review* 170 (2 June 1968), pp. 379–384. DOI: 10.1103/PhysRev.170.379. URL: https://link.aps.org/doi/10.1103/PhysRev.170.379.

[39] B. M. Garraway. "The Dicke model in quantum optics: Dicke model revisited". In: *Philosophical Transactions of the Royal Society A: Mathematical, Physical and Engineering Sciences* 369 (1939 Mar. 2011), pp. 1137–1155. ISSN: 1364503X. DOI: 10.1098/RSTA.2010.0333. URL: https://royalsocietypublishing.org/.

[40] M. Aspelmeyer, T. J. Kippenberg, and F. Marquardt. "Cavity Optomechanics". In: *Reviews of Modern Physics* 86 (4 Mar. 2013), pp. 1391–1452. DOI: 10.1103/RevModPhys.86.1391. URL: http://arxiv.org/abs/1303.0733.

[41] M. Männikkö. "Position quadrature measurements of a nanomechanical resonator using pulsed optomechanics". Master's thesis. University of Jyväskylä, 2023. URL: https://jyx.jyu.fi/handle/123456789/91993.

[42] Q. Quan, P. B. Deotare, and M. Loncar. "Photonic Crystal Nanobeam Cavity Strongly Coupled to the Feeding Waveguide". In: *Applied Physics Letters* 96 (20 Feb. 2010). DOI: 10.1063/1.3429125. URL: http://arxiv.org/abs/1002.1319.

[43] Q. Quan and M. Loncar. "Deterministic design of wavelength scale, ultra-high Q photonic crystal nanobeam cavities". In: *Optics Express* 19 (19 Aug. 2011), p. 18529. DOI: 10.1364/OE.19.018529. URL: http://arxiv.org/abs/1108.2675.

[44] N. V. Q. Tran et al. "Vertical high emission in photonic crystal nanocavities by band-folding design". In: *Physical Review B - Condensed Matter and Materials Physics* 82 (7 Aug. 2010), p. 075120. ISSN: 10980121. DOI: 10.1103/PHYSREVB.82.075120/FIGURES/9/MEDIUM. URL: https://journals.aps.org/prb/abstract/10.1103/PhysRevB.82.075120.

[45] R. Broeke and X. Leijtens. *Nazca Design (v0.5.13)*. 2021. URL: nazca-design.org.

[46] M. Köfferlein. *Klayout (v0.28.12)*. 2023. URL: klayout.de.

[47] J. Hennig et al. *MPh (v1.2.3)*. Zenodo. 2023. DOI: doi.org/10.5281/zenodo.7749502. URL: github.com/MPh-py/MPh.

[48] J. A. Stratton and L. J. Chu. "Diffraction Theory of Electromagnetic Waves". In: *Physical Review* 56 (1 July 1939), pp. 99–107. DOI: 10.1103/PhysRev.56.99. URL: https://link.aps.org/doi/10.1103/PhysRev.56.99.

[49] M. A. Hopcroft, W. D. Nix, and T. W. Kenny. "What is the Young's Modulus of Silicon?" In: *Journal of Microelectromechanical Systems* 19 (2 2010), p. 229. DOI: 10.1109/JMEMS.2009.2039697.

[50] C. Shakespeare. "Seeing the Light: Towards Optical Readout of Donor Spins in Silicon". PhD thesis. University of Jyväskylä, (2024, Unpublished).

[51] D. P. DiVincenzo and IBM. "The Physical Implementation of Quantum Computation". In: *Fortschritte der Physik* 48 (9-11 Feb. 2000), pp. 771–783. DOI: 10.1002/1521-3978(200009)48:9/11<771::AID-PROP771>3.0.CO;2-E. URL: http://arxiv.org/abs/quant-ph/0002077.

[52] R. P. Feynman. "Simulating physics with computers". In: *International Journal of Theoretical Physics* 21 (6-7 June 1982), pp. 467–488. ISSN: 00207748. DOI: 10.1007/BF02650179/METRICS. URL: https://link.springer.com/article/10.1007/BF02650179.

[53] D. Deutsch, A. Barenco, and A. Ekert. "Universality in Quantum Computation". In: *Proceedings of the Royal Society of London. Series A: Mathematical and Physical Sciences* 449 (1937 May 1995), pp. 669–677. DOI: 10.1098/rspa.1995.0065. URL: http://arxiv.org/abs/quant-ph/9505018.

[54] G. Kurizki et al. "Quantum technologies with hybrid systems". In: *Proceedings of the National Academy of Sciences* 112.13 (2015), pp. 3866–3873. DOI: 10.1073/pnas.1419326112. URL: https://www.pnas.org/doi/abs/10.1073/pnas.1419326112.

[55] P. W. Shor. “Algorithms for quantum computation: Discrete logarithms and factoring”. In: *Proceedings - Annual IEEE Symposium on Foundations of Computer Science, FOCS* (1994), pp. 124–134. ISSN: 02725428. DOI: 10.1109/SFCS.1994.365700.

[56] L. K. Grover. “A fast quantum mechanical algorithm for database search”. In: *Proceedings of the Annual ACM Symposium on Theory of Computing* Part F129452 (May 1996), pp. 212–219. ISSN: 07378017. DOI: 10.1145/237814.237866. URL: https://arxiv.org/abs/quant-ph/9605043v3.

[57] N. Samkharadze et al. “Strong spin-photon coupling in silicon”. In: *Science* 359 (6380 Mar. 2018), pp. 1123–1127. ISSN: 10959203. DOI: 10.1126/science.aar4054. URL: https://www.science.org/doi/10.1126/science.aar4054.

[58] P. Haikka et al. “Proposal for detecting a single electron spin in a microwave resonator”. In: *Physical Review A* 95 (2017), p. 22306. DOI: 10.1103/PhysRevA.95.022306.

[59] A. Montanaro. “Quantum algorithms: an overview”. In: *npj Quantum Information* 2 (1 Jan. 2016), pp. 1–8. ISSN: 2056-6387. DOI: 10.1038/npjqi.2015.23. URL: https://www.nature.com/articles/npjqi201523.

[60] K. Bharti et al. “Noisy intermediate-scale quantum algorithms”. In: *Reviews of Modern Physics* 94 (2022). DOI: 10.1103/RevModPhys.94.015004.

[61] D. Englund, I. Fushman, and J. Vuckovic. “General recipe for designing photonic crystal cavities”. In: *Opt. Express* 13.16 (Aug. 2005), pp. 5961–5975. DOI: 10.1364/OPEX.13.005961. URL: https://opg.optica.org/oe/abstract.cfm?URI=oe-13-16-5961.

A Discarded unit cell geometries

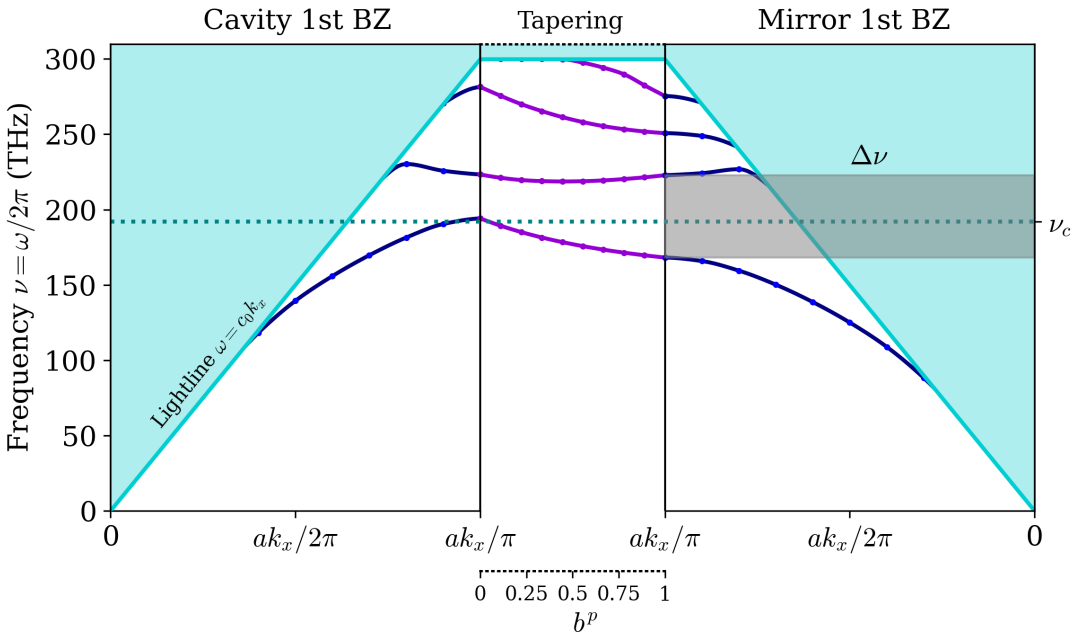

Figure 30. Discarded unit cell geometries with $a = 500\,\text{nm}, d = 0.6a$ and tapering between cavity with $f = 0.3a$,$w = 1.6a$ and mirror with $f = 0.45a, w = 2.7a$ parameters. The unit cell geometries resulted in higher coupling for cavity cells and higher bandgap for mirror cells. However, overall maximum quality factor was lower at $Q \sim 10^5$ regardless of the chosen scaling power p. We attributed this to the dissimilar behavior of the lowest photonic bands when tapering.